A Comparative Study of Gold Bonding via Electronic Spectroscopy

by

Ruohan Zhang

A Dissertation Presented in Partial Fulfillment
of the Requirements for the Degree
Doctor of Philosophy

Approved July 2017 by the
Graduate supervisory committee:

Timothy C. Steimle, Chair
Ranko Richert
Peter Williams

ARIZONA STATE UNIVERSITY

August 2017

ABSTRACT

The bonding and electrostatic properties of gold containing molecules are highly influenced by relativistic effects. To understand this facet on bonding, a series of simple diatomic AuX (X=F, Cl, O and S) molecules, where upon bond formation the Au atom donates or accepts electrons, was investigated and discussed in this thesis.

First, the optical field-free, Stark, and Zeeman spectroscopic studies have been performed on AuF and AuCl. The simple polar bonds between Au and typical halogens (i.e. F and Cl) can be well characterized by the electronic structure studies and the permanent electric dipole moments, μ_{el}. The spectroscopic parameters have been precisely determined for the [17.7]1, [17.8]0^+ and $X^1\Sigma^+$ states of AuF, and the [17.07]1, [17.20]0^+ and $X^1\Sigma^+$ states of AuCl. The μ_{el} have been determined for ground and excited states of AuF and AuCl. The results from the hyperfine analysis and Stark measurement support the assignments that the [17.7]1 and [17.8]0^+ states of AuF are the components of a $^3\Pi$ state. Similarly, the analysis demonstrated the [19.07]1 and [19.20]0^+ states are the components of the $^3\Pi$ state of AuCl.

Second, my study focused on AuO and AuS because the bonding between gold and sulfur/oxygen is a key component to numerous established and emerging technologies that have applications as far ranging as medical imaging, catalysis, electronics, and material science. The high-resolution spectra were record and analyzed to obtain the geometric and electronic structural data for the ground and excited states. The electric dipole moment, μ_{el}, and the magnetic dipole moment, μ_m, has been the precisely measured by applying external static electric and magnetic fields. μ_{el} and μ_m are used to give insight into the unusual

complex bonding in these molecules.

In addition to direct studies on the gold-containing molecules, other studies of related molecules are included here as well. These works contain the pure rotation measurement of PtC, the hyperfine and Stark spectroscopic studies of PtF, and the Stark and Zeeman spectroscopic studies of MgH and MgD.

Finally, a perspective discussion and conclusion will summarize the results of AuF, AuCl, AuO, and AuS from this work (bond lengths, dipole moment, etc.). The highly quantitative information derived from this work is the foundation of a chemical description of matter and essential for kinetic energy manipulation via Stark and Zeeman interactions. This data set also establishes a synergism with computation chemists who are developing new methodologies for treating relativistic effects and electron correlation.

ACKNOWLEDGMENTS

There have been many people who helped me greatly during my PhD study, and I would like to express my sincere gratitude to them. First, I would like to thank my advisor, Professor Timothy C. Steimle for his patience, support, motivation and immense knowledge. It was him who came to USTC to interview with me and gave me the opportunity to pursuing Ph.D. in his lab. It was also him who continuously mentoring and inspiring me to solve research problems and improve lab skills during the whole 6 year's journey. He is not only my advisor, a friend of mine, but more importantly, an example of a real scientist to me. I am grateful for him in my whole life.

I would also like to express my thanks to my dissertation committee members, Professor Peter Williams and Professor Ranko Richert, for their valuable time and insightful comments during these years.

I would like to thank Dr. Anh Le and Dr. Fang Wang for their grateful help when I first joined the lab. They taught me a lot of things, not only in the lab, but also in daily life, not only the knowledge, but also the skills. Also, I want to thank Trung for his patient on helping me improve and finish experiments. I would also like to express my gratefulness to all my friends and colleagues in Prof Steimle's lab and School of Molecular Science.

My thanks also go to my collaborators, Professor Michael C. Heaven (Emory), Professor John Stanton (U. Florida), and Prof. Lan Cheng (John Hopkins U.), for their important contributions to my thesis.

Last but not least, I would like to thank my family; my parents for their nurturing, love, and always being supportive on my education, my wife for her never-ending love, encouragement, and understanding, and my son for coming into my life and sharing this joyful journey with me.

TABLE OF CONTENTS

Page

CHAPTER Page

CHAPTER Page

LIST OF TABLES

Table Page

Table Page

Table Page

LIST OF FIGURES

Figure Page

Figure Page

Figure Page

Figure Page

1. INTRODUCTION

1.1 A brief history of spectroscopy

Although the spectral nature of the light is present in the rainbow, people didn't recognize and understand this phenomenon until 1666 that Newton showed that the light from the sun could be dispersed into a continuous series of colors like a rainbow. That is considered as the beginning of the history of spectroscopy with the word "spectrum" introduced to describe this phenomenon. Then people started to realize that the sun's radiation has the components of the colors of a rainbow. W. Herschel (1800) demonstrated that the sun's radiation extended into the infrared, and J.W. Ritter (1801) made similar observations in the ultraviolet. More important, dark lines in the solar spectrum were observed first by W. H. Wollaston in 1802 [1] by using narrow slits to disperse the wavelengths and then improved by Fraunhofer in 1814 [2]. Although discovered earlier, people didn't understand the cause of these observed dark lines until in 1859 Kirchoff and Bonsen found the spectral lines belonged to unique chemical element. Since then, by realizing each atom and molecular has its own characteristic spectrum, spectroscopy as a scientific tool to study the atomic and molecular structure was established.

The development of atomic molecular theories was motivated by trying to understand the spectral data. The spectral lines were noticed to be located at discrete wavelengths. In 1885, various visible spectral lines of atomic hydrogen were grouped by Balmer using a simple mathematical formula, known as the Balmer series. Later Rydberg and others extended this idea and recognized the spectral lines of atomic hydrogen at other wavelengths. But the insight of this phenomena was explained by the idea of "quantum mechanics" introduced primarily and started by Planck in the early 1900s. Planck assumed

that the energy of light consisted of small energy units, known as "quanta". In 1905 the photoelectron effect was described by Einstein and he proposed the idea that the light was composed of photons, with energy, $E=hv$ (h is the Planck's constant and v is the light's frequency). In 1913, Bohr modeled the hydrogen atomic lines using the concept of quantized energy and bought the idea that electrons exist in quantized energetic states and undergo transitions from one state to another. This work was awarded the Nobel Prize in 1925. In 1924, Louis de Broglie postulated the wave nature of electrons and suggested all matters have wave properties in his PhD thesis. Around 1925, Heisenberg, Born and Jordan invented the matrix mechanics to first represent the form of quantum mechanics. Later in 1926, Schrödinger formulated the wave function using differential equations form of quantum mechanics. In 1927, based upon the wave-particle duality, Heisenberg brought the idea of the uncertainty principle. Since then, the basic principles of quantum mechanics has been introduced and most of the understanding on modern physics and chemistry are driving from these early ideas.

The era of modern spectroscopy began with the invention of the laser in 1960 by Theodore Maiman. Laser, an acronym for "light amplification by stimulated emission of radiation", can provide intense, collimated and monochromatic radiation beam over wide spectral ranges. These advantages opened many fields of modern spectroscopy in both resolution domain and time domain. Here in my thesis, the technique applied is the high-resolution laser induced fluorescence (LIF) spectroscopy, the detail of which will be introduced in Chapter 3.2.

1.2 An introduction on gold chemistry

When the word “gold” comes into your mind, most people will have an image of a bright, yellow metal. This pretty signature color and the relative rarity of gold made it known as “King of the metals” for the first few thousand years of history. Gold has a noble personality, referring to its resistance to most corrosive forces and chemical reactions. While being chemically inactive, gold is also soft, malleable, and ductile, making it to be an ideal material used for coinage, jewelry and other arts. In recent decades, gold extends its application to industries. Gold metal is an excellent material used in the electronics industry due to its low electrical resistivity (0.022 μΩ·m) and high thermal conductivity (310 W/mK). More important, gold changes its role in industry no longer being as a bulk metal after the recent discovery of gold nanoparticles and nanowires [3]. This discovery is not only important in industry, it is also considered as a milestone from the view of science. When you look at the number of publication related to gold chemistry, it increased dramatically since the discovery of nanoparticles. (Figure 1.1)

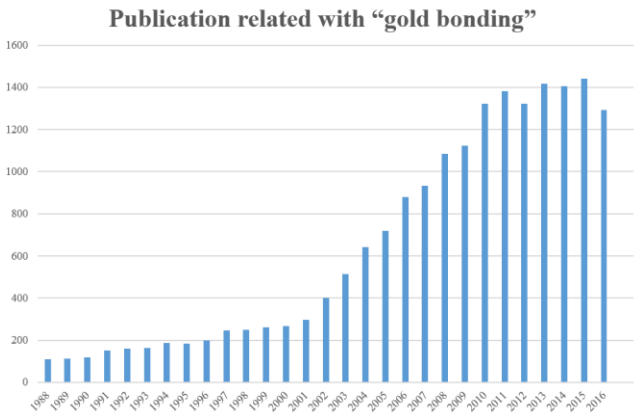

Figure 0.1 Number of publications related with "gold bonding" to illustrate the increasing interests on gold chemistry.

The history of gold chemistry, not the alchemy, can be tracked back to 19th and 20th century when it is realized that gold was not simply a homologue of the other two metals in the periodic table, copper and silver[4] . Compared to the other two, gold shows different oxidation states and oxidation potentials, coordination numbers and coordination geometries[5]. With the electronic ground state configuration of [Xe][4f^{14}][5d^{10}]6s^1, gold(I) compounds are favored to come up with a closed-shell configuration [5d^{10}], which is analogues to the situation in copper(I)[3d^{10}] and silver(I)[4d^{10}]. However, the first ionization potential of a gas phase gold atom (9.225 eV) is significantly higher than that of silver atom (7.576 eV). Therefore, gold is behaving more like a non-corrosive, noble metal while silver is and copper are easier to be tarnished. In addition, silver is oxidized to form Ag(I) compounds when dissolved in the HNO_3, while gold generates not Au(I) but Au(III) compounds reacting with aqua regia.

$$Ag + 2HNO_3 \rightarrow AgNO_3 + H_2O + NO_2 \quad (1.1)$$

$$Au + 3HNO_3/4HCl \rightarrow HAuCl_4 + 3H_2O + 3NO_2 \quad (1.2)$$

Thought to be the most "noble" metal, gold actually has a rich chemistry. As mentioned above, gold could form different compounds with various oxidation states, which varies from Au(I) to Au(V). A more interesting "personality" of gold is its ability to form stable compounds as an anionic component, Au^-, the auride anion [6, 7]. This is first observed in the compound of Cs+Au- by reacting elemental cesium with gold back to 1930s [8, 9]. This is not surprising when you consider the electron affinity of gold. Gold's atomic electron affinity (~2.311 eV) is the largest of all metals, which is not far from that of iodine (~ 3.057 eV). It has been proved that the auride anions (Au^-) can replace iodide anions in salt lattices without changing those alloys or causing any redox reactions [10, 11].

The observed unique "personalities" of gold gives rise to a question: why is its behavior so different from other metals. It is hard to find a straightforward answer by just looking at the periodic table and using the information presented in standard chemistry textbooks. Indeed, most of the unusual properties of gold are due to its large relativistic effect, which are not well documented in chemistry textbook. Relativistic effects are caused by the high speeds of electrons when moving near a heavy nucleus and leads to a 6*s* orbital energies stabilization and radial contraction [7, 12]. Among those heavy elements (Z>55), gold has a significantly large relativistic effect, larger than its neighbors and any other elements with Z<100. It can be quantitatively illustrated in Figure1.2 by comparing the contraction effect of the 6*s* orbital of gold with other elements [7]. Here the different predicated radial extent of the 6*s* orbital with and without relativistic contribution are given.

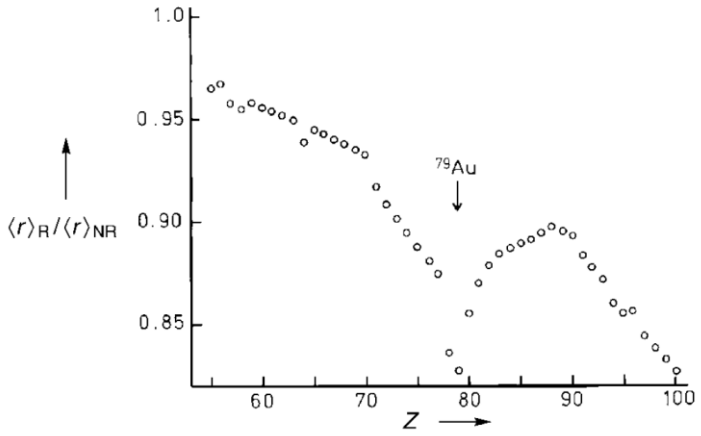

Figure 0.2 The ratio of relativistic and nonrelativistic 6s shell radii in the atomic ground states of the elements 55–100.[7]

The signature color of gold, back to the start of this subchapter, is another prominent example of this relativistic effect. Under the relativistic effect, 6*s* orbital on gold atom is having an energies stabilization and radial contraction, while 5*d* orbital is experiencing an effect of the opposite sign, with a destabilization and expansion [12, 13]. These effects lead to a small band gap between the Fermi level of 5*d* band and that of 6*s* band, which would be much larger in a set of non-relativistic orbitals, i.e. silver. Therefore, the color shown to human eyes is yellow for gold, and bright gray for silver. This effect exists as the same way in molecules as illustrated in Figure 1.3. The molecular orbitals in AuH are more affected by the relativistic effect than those in AgH, behaving as a smaller energy separation [14].

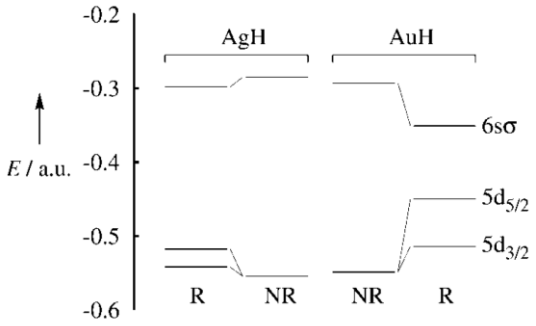

Figure 0.3 The relativistic (R) and nonrelativistic (NR) orbital energies of AgH and AuH molecules (a.u. is atomic units).[12]

There also exists a relativistic contraction on bond-lengths, which is correlated roughly with Z^2 as reported by Desclaux and Pyykko [15]. This contraction causes the single-bond lengths between Au and ligands (Au-L) are less than or similar to those of the corresponding Ag-L bonds, and simultaneously making that the bond strengths of Au-L are larger than those of Ag-L bonds [14, 16].

Due to the peculiar properties of this element, theoretical chemistry of gold is a challenging topic, particularly important in the theoretical predictions of the relativistic effect (RE). Preforming fully relativistic *ab initio* calculations for gold containing molecules is impractical and various approximation need to be implemented. As early as the 1970s, the RE in AuCl, $HgCl_2$, and PtH were studied via self-consistent field (SCF) Hartree-Fock (HF) method by Basch and Topiol [17]. Since then, methods and principles of quantum chemical calculations on RE of gold chemistry have been developed, especially after the development of parallel processing computer technology. Systematic reviews of theoretical chemistry of gold have been reported by P. Pyykko [12, 18, 19].

A common question that all theorists have to face is how to judge and verify their methods and predictions. Simple gas-phase gold containing diatomic molecules AuX (X=F, Cl, O, S) introduced here are ideal venues for testing the various computational methodologies. This is the simplest model for the Au adatom-X system. Compared with similar counterparts in condensed-phase, experimental studies of gold containing molecules in gas phase have advantages of isolating the bonding between gold and its ligand. The bonding properties of these molecules can be precisely derived from high-resolution spectroscopic measurements. A comparison of predicted and experimentally determined molecular bond lengths, r_e, electric dipole moments, μ_{el}, and magnetic dipole moments, μ_m, are particularly insightful for assessing predicted electronic wave functions. Although gas-phase studies of gold-containing molecules will not reveal all aspects of bonding between the ligands to the gold nanoparticles or extended surfaces, i.e. Au-S binding in nanoparticles. Still, the conceptual framework developed by the experiential/theoretical synergism established for the simple gas-phase systems will be applicable to modeling the chemistry of the more extended systems.

2. MOLECULAR THRORY

2.1 Terms symbols of Diatomic Molecules

Electronic states and structures of a diatomic molecule are designated by molecular term symbols to represent the information of both electronic orbital and electronic spin angular momenta. A term symbol is a compact notation for listing all the approximately good quantum numbers and has the general form of:

$$^{2S+1}\left|\Lambda\right|^{+/-}_{|\Omega|} \tag{2.1}$$

In this scheme the projection of total orbital angular momentum, L, usually leads to well defined component, Λ, along the internuclear axis:

$$\hat{L}^2\psi^{el} = L(L+1)\psi^{el} \tag{2.2}$$

$$\hat{L}_Z\psi^{el} = \Lambda\psi^{el} \tag{2.3}$$

The states associated with Λ=0, 1, 2, 3… are called Σ, Π, Δ, Φ… states. The total electronic spin angular momentum, S, resulting from the sum of individual electron spin angular momentum, s_i=1/2, and its projections, S_z, are also eigen operators:

$$\hat{S}^2\psi^{el} = S(S+1)\psi^{el} \tag{2.4}$$

$$\hat{S}_Z\psi^{el} = \Sigma\psi^{el} \tag{2.5}$$

For example, if there are 3 unpaired electrons in a molecule, it will lead to S=3/2 with Σ=–3/2, –1/2, +1/2 and +3/2. The electronic states are called singlet, doublet, triplet, etc.,

states due to the results of $2S+1$. Combination of the two terms are used to label the electronic states, such as ${}^{2S+1}\Sigma$, ${}^{2S+1}\Pi$, etc.

The component along the internuclear axis of the total electronic angular momentum is called Ω, and it is given by:

$$\Omega = \Lambda + \Sigma \tag{2.6}$$

To a first approximation, the energy only depends upon the magnitude of Ω, $|\Omega|$, and this is used as a a label: ${}^{2S+1}\Lambda_{|\Omega|}$. For example, in a ${}^2\Pi$ electronic states, we can have two fine-structure components, labelled as ${}^2\Pi_{3/2}$ and ${}^2\Pi_{1/2}$, due to the possible values of Ω.

In a Σ state, +/- superscripts are used to represent the reflection symmetry of electronic wave function:

$$\hat{\delta}_z \psi^{el} = \pm 1 \cdot \psi^{el} \tag{2.7}$$

If the sign of the eigenfunctions in diatomic molecules remain unchanged when reflected along the plane containing the internuclear axis, it is a Σ^+ state, otherwise it is a Σ^- state. For $|\Lambda| \neq 0$ the superscript is not warranted.

2.2 Coupling of electronic and rotational motion: Hund's coupling cases

In the above subchapter, I introduced the electronic orbital angular momentum (L) and the electronic spin angular momentum (S). Then the question comes up immediately concerning the coupling of L and S. The possible coupling cases are first outlined by Friedrich Hund, and the details of them are described in the Ref [20]. There are five

commonly used coupling cases: Hund's case (a), (b) … (e). Here I only focused on the two most common one of them, Hund's case (a) and case (b), and will be used to understand and analyze the spectra of the molecules discussed in this thesis.

The description of Hund's case (a) coupling case is best illustrated by the vector diagram shown in Figure 2.1. The electronic orbital angular momentum (L) and the electronic spin angular momentum (S) are strongly coupled together along the internuclear axis. The components of this spin-orbit coupling, Ω, is denoted by the sum of Λ and Σ. The angular momentum of the end-over-end rotating nuclei, R, is coupled to and forms the resulting total angular momentum, J. Therefore, the vector coupling could be written as:

$$J=R+\Omega \tag{2.8}$$

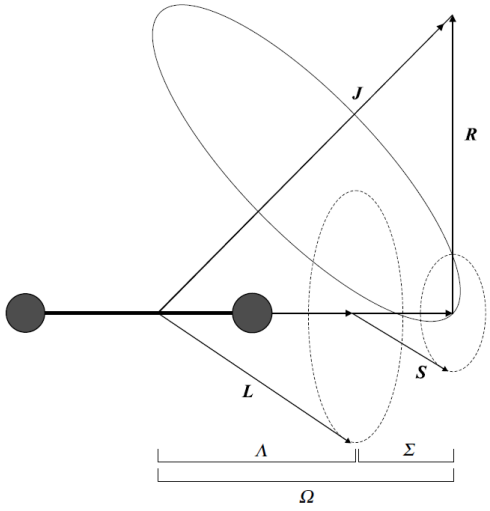

Figure 0.4 The description of Hund's case (a) coupling case illustrated by the vector diagram

The eigenfunctions for a hypothetical molecule having a Hund's case (a) coupling scheme is the simple product of:

$$\Psi_{case(a)} = \left|\eta\Lambda\right\rangle\left|S\,\Sigma\right\rangle\left|J\,\Omega M_J\right\rangle \tag{2.9}$$

where the symbol η denotes all other quantum numbers, and M_J is the component of J along the laboratory-z axis. M_J will be important when there is applied external electric or magnetic field. Hund's case (a) is a good representation whenever $A\Lambda$ is much greater than BJ. A is the spin-orbit coupling constant, and B is the rotational constant. Under Hund's case (a) limit, the good quantum numbers are: η, Λ, S, Σ, J, and Ω. The function given in Eq. (2.9) are commonly used as basis function for modelling the energy levels of real molecules.

On the other hand, Hund's case (b) becomes a good representation when the energy of $A\Lambda$ is much less than BJ. In this case, the spin-orbit coupling between L and S vanished or it is so weak that does not apply. As shown in Figure 2.2, Λ is coupled to R to form N; N is then coupled with S to form the total angular momentum J. N is the total angular momentum excluding electron spin, so that $N=J-S$. The basis sets in case (b) are expressed as $\left|\eta\Lambda\right\rangle(NS)J, M_J\rangle$, and the good quantum numbers are: η, Λ, N, S, and J.

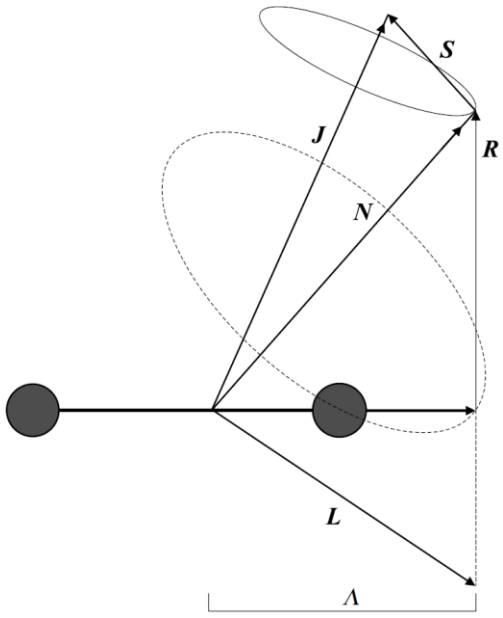

Figure 0.5 The description of Hund's case (a) coupling case illustrated by the vector diagram

2.3 Effective Hamiltonian Operator

In Born-Oppenheimer (BO) approximation the motion of the nuclei (i.e. vibrations and rotations) and electron motions are treated separately. The justification for the BO approximation is the large mass difference between the electron and nuclei. The electrons move freely while the nucleus are considered to be stationary. Therefore, the total energy of a molecule can be treated separately by the following parts: *a*) the nuclear kinetic energy; *b*) the electronic kinetic energy; *c*) the electron-nuclear attraction; *d*) the nuclear-nuclear repulsion; *e*) the electron-electron repulsion. The total Hamiltonian can be given by:

$$\hat{H}_T = -\frac{\hbar^2}{2}\sum_{I=1}^{N}\frac{1}{M_I}\nabla_I^2 - \frac{\hbar^2}{2m}\sum_{i=1}^{n}\nabla_i^2 - \sum_{I=1}^{N}\sum_{i=1}^{n}\frac{Ze^2}{r_{i,I}} + \sum_{I=1}^{N}\sum_{J=1}^{N}\frac{Z_I Z_J e^2}{r_{I,J}} + \sum_{i=1}^{n}\sum_{j=1}^{n}\frac{e^2}{r_{i,j}} \qquad (2.10)$$

“*a*” “*b*” “*c*” “*d*” “*e*”

In a molecule, the separations of energies between each different electronic state are usually much greater than those between each vibrational level, and so are the comparison of the separations between the vibrational levels and rotational levels. The total Hamiltonian operator also accounts for the interactions between the different electronic states and vibrational levels. It may be thought that having the Hamiltonian operator and basis functions (either case (a) or (b)) than the standard approach for determining the energies could be employed. Namely the complete set of basis functions for all electronic vibration and rotation motions be used to construct a massive representation which is then diagonalized to produce energies. This is illustrated in Figure 2.3 for the lowest states of OH radicals which has a $X^2\Pi$ ground state and an $A^2\Sigma^+$ excited state. The problem with this direct approach is that the matrix representation is of infinite order. All those factors result in the dimension of the matrix representation for the total Hamiltonian operator being incredibly large and hard to solve.

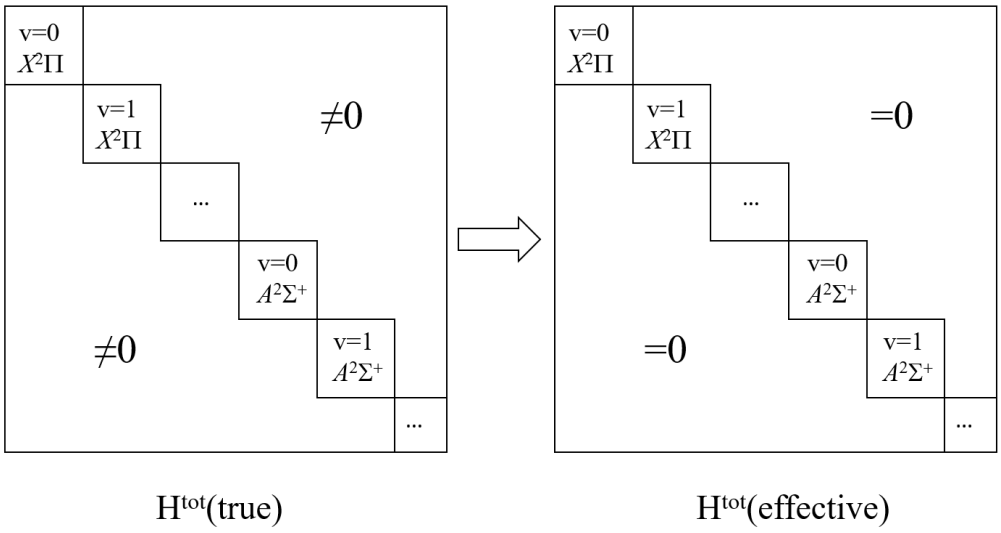

Figure 0.6 A schematic diagram of the transform of the total Hamiltonian matrix representation (left) to the effective Hamiltonian.

To simplify the analysis and to facilitate extraction of the insight, an effective Hamiltonian, H^{eff}, is formed by adding several terms to the true Hamiltonian, H^{t}, that accounts for the various interactions. Unlike H^{t}, the H^{eff} operates only within the energy levels of a single vibrational level of a single electronic state, such as for the rotational levels and hyperfine interactions. The effective Hamiltonian are different for each electronic state of a diatomic molecule. In this way the dimensions of the matrix representations for the Hamiltonian operator is reduced to a finite size, which greatly simplified the analysis and calculation. The most general form of the effective Hamiltonian for a field-free diatomic molecule can be written as the sum of the following terms [20]:

$$\hat{H}^{eff} = \hat{H}_{so} + \hat{H}_{ss} + \hat{H}_{sr} + \hat{H}_{rot} + \hat{H}_{cd} + \hat{H}_{LD} + \hat{H}_{mhfs} + \hat{H}_{Q} \qquad (2.11)$$

where $\hat{H}_{so}$ is the Hamiltonian operator for spin-orbit interaction; $\hat{H}_{ss}$ is the Hamiltonian operator for spin-spin interaction, $\hat{H}_{sr}$ is the Hamiltonian operator for spin-rotation interaction, $\hat{H}_{rot}$ is the Hamiltonian operator for rotation, $\hat{H}_{cd}$ is the Hamiltonian operator for centrifugal distortion, $\hat{H}_{LD}$ is the Hamiltonian operator for Λ-doubling, $\hat{H}_{mhfs}$ is the Hamiltonian operator for magnetic hyperfine interaction, $\hat{H}_{Q}$ is the Hamiltonian operator for electric quadrupole interaction. The $\hat{H}_{cd}$ and $\hat{H}_{LD}$ terms in the effective operator have been added such as to account for interactions between vibrionic and electronic states.

The Hamiltonian operator for spin-orbit interaction is:

$$\hat{H}_{so} = A\hat{L}_z\hat{S}_z \tag{2.12}$$

where A is the spin-orbital coupling constant; $\hat{L}_Z$ and $\hat{S}_Z$ are the orbital and spin angular momentum operators, respectively.

The Hamiltonian operator for spin-spin interaction is:

$$\hat{H}_{ss} = \frac{2}{3}\lambda(3\hat{S}_z^2 - \hat{S}^2) \tag{2.13}$$

where λ is the spin-spin parameter.

The Hamiltonian operator for spin-rotation interaction is:

$$\hat{H}_{sr} = \gamma\hat{N}\cdot\hat{S} \tag{2.14}$$

where γ is the spin-rotation parameter.

The Hamiltonian operator for rotation is:

$$\hat{H}_{rot} = B\hat{R}^2 \tag{2.15}$$

where B is the rotational constant that related with the reduced mass (μ) and bond length (r) of the molecules ($B = \frac{h}{8\pi^2 \mu r^2}$). $\hat{R}$ is the operator of the rotation.

The Hamiltonian operator for centrifugal distortion is:

$$\hat{H}_{cd} = -D\hat{R}^2\hat{R}^2 \tag{2.16}$$

where D is the centrifugal distrotion constant.

The Hamiltonian operator for Λ-doubling is:

$$\hat{H}_{LD} = \frac{1}{2}o(\hat{S}_+^2 + \hat{S}_-^2) - \frac{1}{2}p(\hat{N}_+\hat{S}_+ + \hat{N}_-\hat{S}_-) + \frac{1}{2}q(\hat{N}_+^2 + \hat{N}_-^2) \tag{2.17.1},$$

$$\text{or } \hat{H}_{LD} = \frac{1}{2}(o+p+q)(\hat{S}_+^2 + \hat{S}_-^2) - \frac{1}{2}(p+2q)(\hat{J}_+\hat{S}_+ + \hat{J}_-\hat{S}_-) + \frac{1}{2}q(\hat{J}_+^2 + \hat{J}_-^2) \tag{2.17.2}$$

where the *o, p, q* are the Λ -doubling constant. Equation (2.17.1) usunally refers to a molecule under Hund's case (b) basis set, and equation (2.17.2) usunally is under Hund's case (a) basis set.

Most relevant to my study of this thesis are the modelling and analysis of the hyperfine interactions. These interactions are of four types:

1) nuclear quadrupole moment with the electric field gradient at the nucleus;
2) Fermi contact interaction;

3) electronic orbital angular momentum magnetic moment with the magnetic moment of the nucleus;
4) electronic spin angular moment magnetic moment with magnetic moment of the nucleus.

The first type of the effect is called the electric quadrupole interaction. The combined effects of 2-4 are called the magnetic hyperfine effect. The Hamiltonian operator for electric quadrupole interaction is:

$$\hat{H}_Q = \frac{eq_0Q}{4I(2I-1)}(3\hat{I}_z^2 - \hat{I}^2) - \frac{eq_2Q}{8I(2I-1)}(\hat{I}_+^2 + \hat{I}_-^2) \tag{2.18}$$

where the eq_0Q and eq_2Q are the electric quadrupole interaction parameters. Here and are related to the electric field qradients parallel and perperdicular to the bond axis.

The Hamiltonian operator for magnetic hyperfine interaction is:

$$\hat{H}_{mhfs} = a\hat{I}_z\hat{L}_z + b_F\hat{I}\cdot\hat{S} + \frac{1}{3}c(3\hat{I}_z\hat{S}_z - \hat{I}\cdot\hat{S}) - \frac{1}{2}d(\hat{S}_+\hat{I}_+ + \hat{S}_-\hat{I}_-) \tag{2.19}$$

where *a, b, c,* and *d* are the magnetic hyperfine constant. Each term in equation (2.13) refers to the nuclear spin electron orbit interaction (*a*), Fermi contact interaction (b_F) , the diagonal dipolar interaction (*c*), the non-diagonal nuclear spin-electron spin dipolar interaction(*d*). The defination of the magenetic hyperfine parameters are [20-22]:

$$a/\mathrm{Hz} = \left(\frac{\mu_0}{4\pi h}\right) g_e g_N \mu_B \mu_N \frac{1}{\Lambda} <\Lambda| \sum_i \frac{\hat{l}_{zi}}{r_i^3} |\Lambda> \tag{2.20},$$

$$b_F/\mathrm{Hz} = \left(\frac{\mu_0}{4\pi h}\right)\left(\frac{8\pi}{3}\right) g_e g_N \mu_B \mu_N \frac{1}{\Sigma} <\Lambda\Sigma| \sum_i \hat{s}_{zi}\delta_i(r) |\Lambda\Sigma> \tag{2.21},$$

$$c/\mathrm{Hz} = \left(\frac{\mu_0}{4\pi h}\right)\frac{3}{2} g_e g_N \mu_B \mu_N \frac{1}{\Sigma} < \Lambda\Sigma| \sum_i \hat{s}_{zi} \frac{(3\cos^2\theta_i - 1)}{r_i^3} |\Lambda\Sigma> \quad (2.22),$$

$$d/\mathrm{Hz} = \left(\frac{\mu_0}{4\pi h}\right)\frac{3}{2} g_e g_N \mu_B \mu_N < \Lambda'\Sigma' | \sum_i s_{-i} \frac{sin^2\theta_i}{r_i^3} e^{2i\phi_i} |\Lambda''\Sigma'' > \quad (2.23),$$

where $\hat{l}_{zi}$ and $\hat{s}_{zi}$ are orbital and spin angular momentum operators for the i^{th} electron. $\vec{r}_i$ and θ_i are the spherical polar coordinates of the electrons relative to the nuclei with I≠0.

2.4 Interaction with external field: Stark effect & Zeeman effect

In the presence of an external electric field the spectral lines of atoms are found to shift and/or split into several components. This effect was first discovered by Johannes Stark, and is called Stark effect. It is due to the interaction of the molecule's electric dipole moment with the external electric field and the interaction Hamiltonian can be written as [20, 23]:

$$\hat{H}^{Stark} = -\hat{\mu}_{el} \cdot \hat{E}\,, \quad (2.24)$$

where $\hat{E}$ is the external electric field and $\hat{\mu}_{el}$ is the molecular frame electric dipole moment operator. This operator typically suffices to model the observed shift/splitting when the field strength is less than 10 kV/cm.

In the presence of a magnetic field the spectral lines of atoms or molecules is also found to shift or split into several components and it is called the Zeeman effect. Zeeman studies of molecules provide valuable information about the orbital and spin angular momenta, and the nature of any perturbing electronic state. The interaction of the molecule within the external magnetic field can be modelled using the Zeeman Hamiltonian:

$$\hat{H}^{Zee} = -\hat{\mu}_m \cdot \hat{B}, \tag{2.25}$$

where $\hat{B}$ is the external magnetic field, $\hat{\mu}_m$ is the magnetic dipole moment operator of the molecules. The major contribution to $\hat{\mu}_m$ are the electronic orbital ($-\mu_B g_L \hat{L}$), electronic spin ($-\mu_B g_S \hat{S}$), and a rotational ($-\mu_B g_R \hat{R}$) terms. The rotational magnetic dipole moment is negligibly small for low rotational levels, which are the focus of my studies. Thus, the effective Zeeman Hamiltonian can be taken as [20, 24]:

$$\hat{H}^{Zee} = \mu_B g_L \hat{L} \cdot \hat{B} + \mu_B g_S \hat{S} \cdot \hat{B} + g_l \mu_B \left[\hat{S}_x \hat{B}_x + \hat{S}_y \hat{B}_y \right] + g_l' \mu_B \left[e^{-i2\varphi} \hat{S}_+ \hat{B}_+ + e^{+i2\varphi} \hat{S}_- \hat{B}_- \right] \tag{2.26}$$

The "±" designates the ladder operators, φ is the azimuthal angle of the electronic coordinates. The g_l and g_l terms describe the anisotropic contribution to the electron spin which need to be added to $\hat{H}^{eff}$ to account for mixing of electronic states.. g_S, g_L, g_l and $g_{l'}$ are all treated as adjustable parameters to account for electronic state mixing (i.e. $g_L \neq 1.0$, $g_S, \neq 2.002$).

2.5 Predictions of relative intensities

The line strength of an electric dipole allowed transitions between different vibrartion rotation levels in the upper and lower states, *v'J'←v"J"*, is proportional to the product of the population, $N_{v'J'}$, of the excited state level and the Einstein coefficient of spontaneous emission, $A_{v"J"}^{v'J'}$ [25],

$$I_{v"J"}^{v'J'} = KhvN_{v'J'}A_{v"J"}^{v'J'} \tag{2.27}$$

where *K* is a constant expressing the quantum efficiency. The Einstein coefficient, $A_{v"J"}^{v'J'}$,

can be written as:

$$A_{v''J''}^{v'J'} = [\frac{64\pi v^3}{3h(2J'+1)}]S_{v'v''}S_{J'J''} \tag{2.28}$$

where

$$S_{v'v''} = \left|\left\langle v'\left|\mathrm{R}_e^{n'n''}\right|v''\right\rangle\right|^2 \tag{2.29}$$

is called the vibrational band strength factor(which is simply proportional to the Frank-Condon factor, $\langle v'|v''\rangle^2$), and

$$S_{J'J''} = 3\sum_{M',M''}\left|\left\langle J'M'\left|z\right|J''M''\right\rangle\right|^2 \tag{2.30}$$

is called the rotational line strength factor. "z" is the component of the electric dipole transition moment.

Description of dipole moment in a transition is the key for the prediction of relative intensities. Let us take a good case Hund's (a) molecule as an example. The basis set for a Hund's case (a) has been described in the above subchapters. Therefore, for a typical rotational transition between two different rotational levels that are approximated as case (a), the matrix elements for the transition operator, $\hat{\mu}$, is given:

$$\begin{aligned}&\left\langle \eta\Lambda'S'\Sigma'J'\Omega'IF'M_F'\left|T_p^1(\hat{\mu})\right|\eta\Lambda S\Sigma J\Omega IFM_F\right\rangle \\ &= (-1)^{F'-M_F'}\begin{pmatrix} F' & 1 & F \\ -M_F' & p & M_F\end{pmatrix}\times\delta_{\Sigma'\Sigma}(-1)^{J'+I+F+1}\sqrt{(2F'+1)(2F+1)}\times term \\ &term = \begin{Bmatrix} I & J' & F' \\ 1 & F & J\end{Bmatrix}\sum_q(-1)^{J'-\Omega'}\sqrt{(2J'+1)(2J+1)}\begin{pmatrix} J' & 1 & J \\ -\Omega' & q & \Omega\end{pmatrix}\left\langle\eta\Lambda'\left|T_q^1(\mu)\right|\eta\Lambda\right\rangle\end{aligned} \tag{2.28}$$

The 3-j symbol, $\begin{pmatrix} J' & 1 & J \\ -\Omega' & q & \Omega\end{pmatrix}$, in this expression gives the selection rules on the J with that ΔJ=-1, 0, 1. Usually, transitions that satisfied ΔJ=-1are grouped to be called P branch,

and similarly, those with $\Delta J = 0$ are called Q branch and $\Delta J = 1$ are called R branch.

3. EXPERIMENTAL METHOD

3.1 Sample generation

The generation of the molecular samples consists of two steps: a) generate plasma by using the laser ablation technique; b) form the molecular beam via supersonic expansion. The details of the setups will be described in the following sub-chapters.

3.1.1 Laser ablation technique

The production of the target molecules in our lab is usually achieved using the laser ablation/reaction technique. For example, AuS is generated by ablating the gold sample in the presence of an SF_6/Ar gas expansion. A matching stainless steel end-cap is designed to fit the rod of the metal sample as shown in Figure 3.1, with a Teflon holder on the bottom pushing the rod position. Light from Nd: YAG laser (5 mJ/pulse, 532 nm) goes through the top hole on the end cap and ablates the metal rod surface. The ablated metal atoms react with the reagent seeded in the carrier gas (mostly argon or helium) passing through the pulsed valve to produce the target molecules. To have a fresh surface, the metal rod is rotating and translating continuously under the control of a commercial stepper motor via a homemade LabVIEW program. The plasma generated via laser ablation includes electrons, ions, atoms, molecules, clusters, as well as the desired radicals. The plasma also supplied the required energy to drive the chemistry. The ratio of different productions can be affected by the concentration of the reagent in carrier gas, backing pressure, background pressure of the source chamber, type of the carrier gas and ablation laser power. The selection of the end-cap is also important because the hole-size for the ablation laser and the gas-channel affects the production process and the resulting sample temperature.

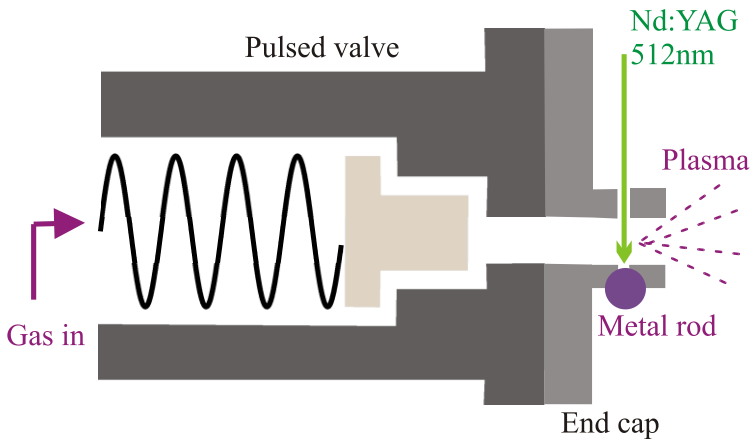

Figure 0.7 A schematic diagram of laser ablation source and supersonic expansion in molecular beam apparatus.

3.1.2 Super free jet expansion and molecule beam

Supersonic free jet expansion has become a common laboratory tool for spectroscopic measurements and provides the ideal environment to study the physical properties of transient metal containing molecules. The theories and properties of the free jet expansion were first discovered by Kantrowitz et al [26] nearly half a century ago and are reviewed by Scoles [27]. A typical schematic diagram of a supersonic free jet expansion is shown in Figure 3.2. The key feature of the free jet expansion is a small nozzle aperture that separates a high-pressure gas source and a downstream vacuum region. In our setup the diameter of the nozzle aperture is around 1 millimeter. The backing pressure of the gas (Ar or He) ranges from 50 psi to more than 700 psi, while the pressure of the downstream is usually less than 10^{-6} torr which is maintained by a pumping system. One important part of this supersonic expansion is that the random orientation of the molecules velocity is converted

to a forward narrow velocity. In addition, the temperature of the post-expansion beam (T) can be heavily cooled down, given by:

$$T = T_0 \cdot (\frac{P}{P_0})^{\frac{\gamma-1}{\gamma}}, \tag{3.1}$$

where T_0 is the pre-expansion temperature, γ is the ratio of the specific heats, P_0 and P are the pressure of the pre- and post-expansion environments. Under the above conditions in most of my experiments, the post-expansion temperature is around 10 to 20 K.

In our high-resolution experimental setup, a "skimmer" is inserted in the travel path of the free jet expansion products to form a will collimated molecular beam. The skimmer is an adjustable iris (D: ~2.5cm) placed approximately 5 cm downstream between the source and detection chambers. This "skimmed" molecule beam can greatly reduce the spectral Doppler broadening effect.

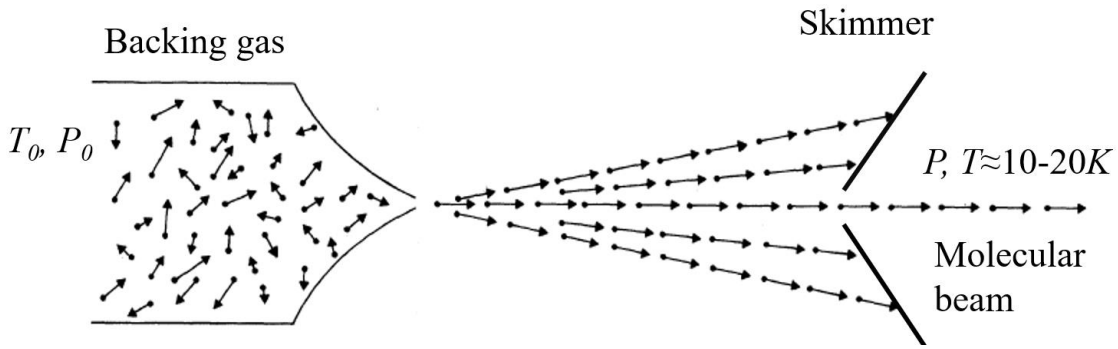

Figure 0.8 A schematic diagram of a supersonic free jet expansion.

3.2 Spectroscopic techniques

3.2.1 Laser induced fluorescence

Laser induced fluorescence (LIF) technique is the key to all my laboratory detections and measurements. The target molecules are excited to a higher energy level by the absorption of laser light, followed by the release of fluorescence light to reveal the structural information of the molecules. There are two types of LIF spectra: excitation spectra and disperse LIF spectra.

Excitation LIF detection is the technique used in most of my work in this thesis. As the wavelength of the laser is scanned, the molecules of interest will be excited and emit fluorescence whenever the laser frequency is tuning to match the energy difference of the molecular levels. This process for a diatomic molecule is usually very sensitive and results in a strong fluorescence signal. The scheme of the light collection system for the fluorescence is shown in Figure 3.3. A spherical lens at the top of the cross-section is used to focus the anistropically emitted light onto a cooled photomultiplier tube (PMT). In addition, a reflection mirror at the bottom is used to help increase collection of the fluorescence signal. Usually, a narrow band-pass filter centered either on or off the laser excitation wavelength is used to reduce background noise and enhance the ratio of signal to noise. The photon induced electrical signals are processed by a gated photon counter (Stanford Research System-SR400) which is interfaced to the data acquisition computer via a LabVIEW program.

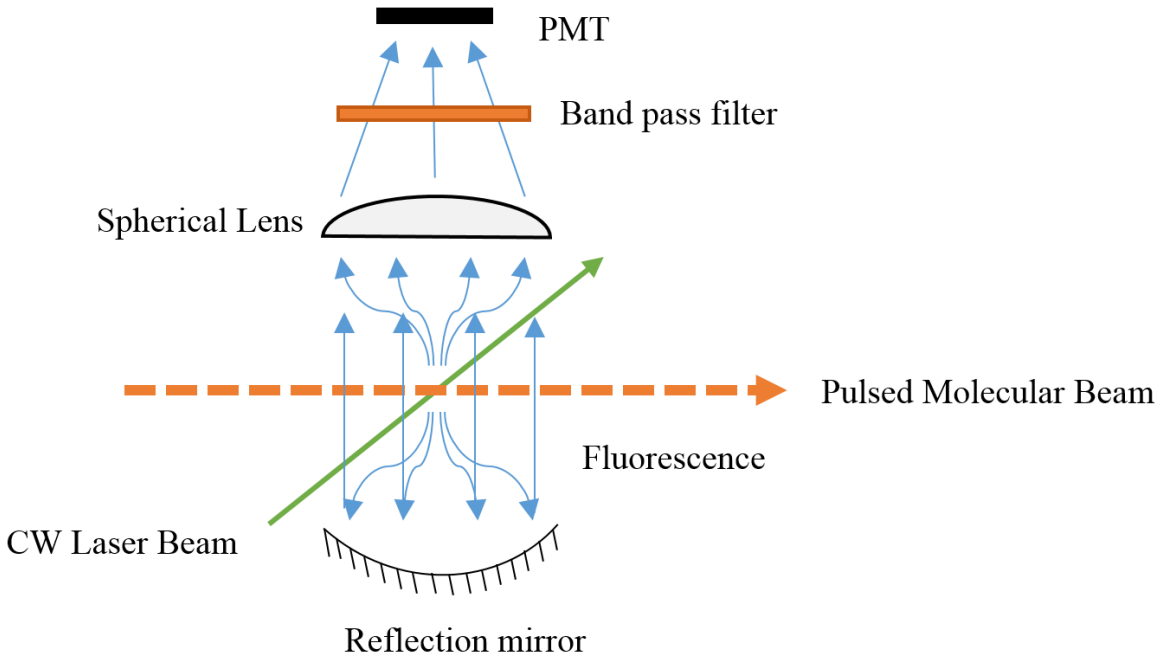

Figure 0.9 A schematic diagram of fluorescence light collection setup.

The dispersed laser induced fluorescence (DLIF) technique provides information about the ground state vibrational structure. In this case the excitation laser is tuning to a certain resonant wavelength, and the resulting LIF signal is viewed through a McPherson 2/3 m scanning monochromator and detected by a similar gated photon counter through the PMT. The resolution of a DLIF spectrum is controlled by the resolving power of the monochromator.

3.2.2 Optical spectrometer

Overall, three types of optical spectroscopy techniques were employed in my thesis:

a. High resolution field-free spectroscopy,

b. Optical Stark spectroscopy,

c. Optical Zeeman spectroscopy.

The experimental setup for *b* and *c* are based upon the first apparatus of *a*.

The high-resolution optical field-free spectrometer consists of the following parts: vacuum chamber, laser, source generation, signal detection and control program. The schematic diagram of my setup is illustrated in Figure 3.4. There are two separate chambers: molecule source chamber and LIF detection chamber. The two chambers are separated by an aluminum plate with an adjustable iris hole in middle to allow the passage of the molecular beam. Each chamber is connected to a mechanical vacuum pump and a 6" diffusion pump. A roots pump is installed on the source side to accelerate the pumping process. Normally the background pressure during the experiment is below 1×10^{-6} torr on both two sides. Details of the source generation and signal detection have been discussed above. The laser beam is from a Coherent model 699 continuous-wave (cw) ring dye laser pumped by the 488nm solid state laser. The output power of the laser beam is around 100 mW with a diameter size of approximately 1.0 mm. This cw dye laser can cover most of the visible range (from 500 nm to 750 nm) by using different species of laser dyes. The calibration of the laser wavelength will be introduced in the following subchapter. A control program written in LabVIEW is used to communicate with each equipment and finish the process of parameter initializing, command sending, data acquiring, and spectra plotting.

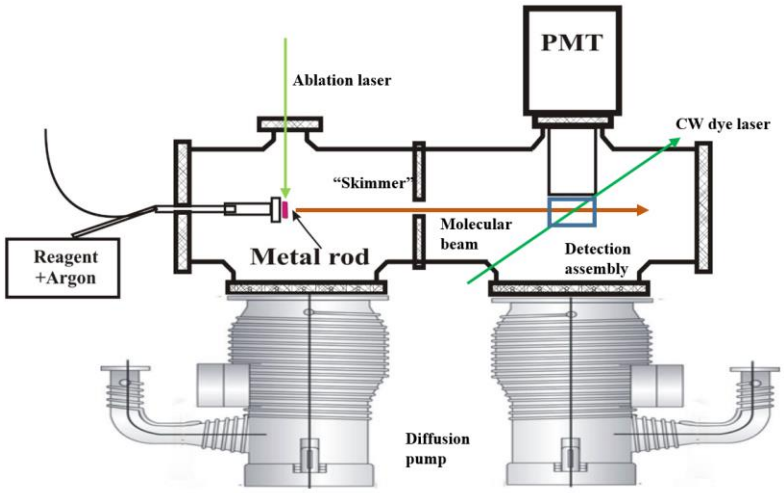

Figure 0.10 A schematic diagram of optical high-resolution spectrometer

To provide an external electric or magnetic field in the type *b* and *c* experiments, additional small devices are placed at the detection area of the field-free setup with all the other parts remaining the same. A schematic diagram of a homemade Stark device are shown in Figure 3.5. The static electric field is generated by applying a voltage across two conducting plates straddling the LIF region. Both plates are 5×5 cm square neutral density filter with 90% transmission of light. A spherical lens and reflection mirror are used to increase the signal. The strength of the electric field can go up to 6000 V/cm. A polarization rotator and polarizing filter are commonly used to orient the electromagnetic field vector of the linearly polarized laser radiation either parallel, "∥", or perpendicular, "⊥", to that of the applied field.

In the Zeeman measurement, static homogenous magnetic fields are generated via a device illustrate in Figure 3.6. This apparatus use a homemade magnet/yoke assembly with rare earth magnets attached to each side of an iron yoke. 5 mm holes are drilled through these poles to allow for the passage of the molecular beam. The magnetic field can

be adjusted by adding or removing additional ferromagnetic poles and varied from 100 to 3000 gauss. The strength is measured using a commercial Hall-type gauss meter. The relative orientation is achieved as described above. The systematic errors arising from the field calibration and the spectral measurement uncertainties in the Zeeman and Stark shifts are estimated to be less than 2%.

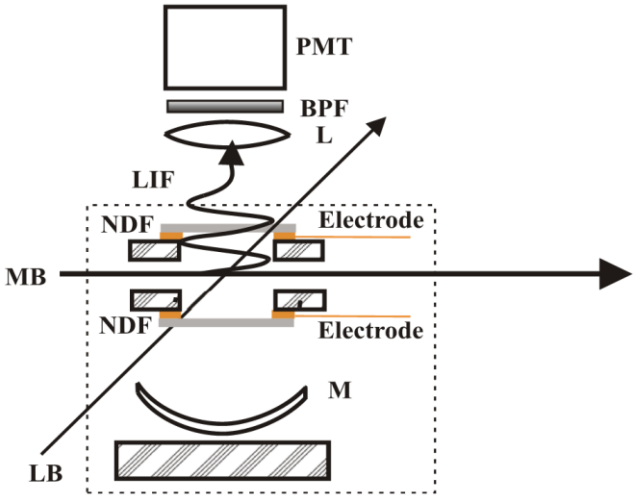

Figure 0.11 A schematic diagram of the electric field and laser excitation region of the Stark spectrometer. Molecular beam (MB); Tunable laser radiation beam (LB); Neutral density filter (NDF); Stainless steel (SS); Cooled photomultiplier tube (PMT); Band pass filter (BPF); Lens(L); Mirror (M); Laser induced fluorescence (LIF).

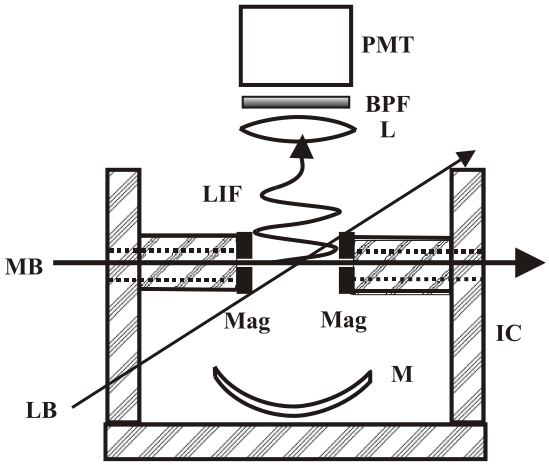

Figure 0.12 A schematic diagram of the magnetic field and laser excitation region of the Zeeman spectrometer. Molecular beam (MB); Tunable laser radiation beam (LB); Rare-earth permanent magnets (Mag); iron core (IC); Cooled photomultiplier tube (PMT); Band pass filter (BPF); Lens(L); Mirror (M); Laser induced fluorescence (LIF).

3.3 Wavelength calibration

The wavelength of the laser beam from the cw ring dye laser is initially determined with a commercial wavemeter (WA 1500, Burleigh) with a precision of ±0.01 cm^{-1}. This precision is further improved to ±0.0001 cm^{-1} (30 MHz) by using a combination of sub-Doppler iodine spectra and etalons. (Figure 3.7) I_2 absorption spectrum is chosen because the precise absolute frequencies of ±0.00001 cm^{-1} (3 MHz) are provided. Sub-Doppler I_2 spectra are recorded using a saturation polarization technique. The cw dye laser is split into two beams. The polarization of one laser beam (labeled A) is rotated via a half wave plate by 90^o, which means the polarization is perpendicular to that of the other laser beam

(labeled B). The laser beam B is mechanically chopped at ~2 kHz. These two beams are counter propagating and are simultaneously absorbed only by these molecules with no transverse velocity (i.e. no Doppler effect). The intensity of laser beam A is detected by a photodiode after absorption. The output signal from the photodiode is monitored by a lock-in amplifier. In this case, the modulation of laser beam B is transferred to a modulation of laser beam A for those molecules that are simultaneously excited (i.e. molecules with zero velocity). Since Doppler broadening is from the thermal motions of molecules, sub-Doppler resolution ($\pm 0.001 cm^{-1}$) can be achieved by molecules with zero velocity. The I_2 cell can be heated to produce more I_2 molecules in the gas-phase and populate additional levels. This will increase the absorption signal.

The relative wavelengths are precisely measured by simultaneously recording the transmissions of two confocal étalons (Fabry-Pérot interferometers) with the sub-Dopper absorption spectrum of I_2 (Figure 3.7). One étalon (labeled Et1) is unstabilized with free spectra range of 75.04 MHz and the other étalon (labeled Et2) is actively stabilized with free spectra range of 750.956 MHz. There is an insulated housing outside the Et2. The Et2 is evacuated and temperature controlled. The cavity spacing of Et2 is locked to the transmission peak of a frequency stabilized Melles Griot Model 05 STP He-Ne laser. The transmission is detected by a photodiode and the signal is under computer control through a lock-in amplifier. When the monitored transmission intensity changes slightly, the spacing of the cavity is changed by sending a correction voltage to the piezoelectric crystal on the mirror or changing the temperature. The relative resolution could be determined to be approximately $\pm 0.0001 cm^{-1}$.

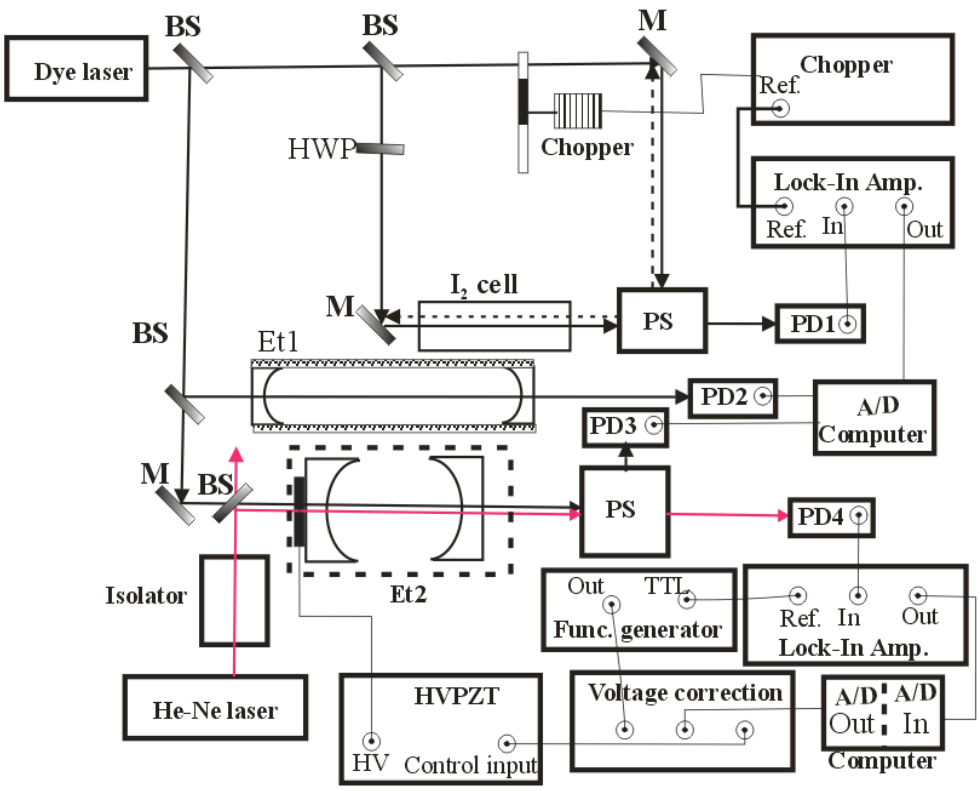

Figure 0.13 A schematic diagram for wavelength calibration. Beam splitter (BS); Mirror (M); Half wave plate (HWP); Photodiode (PD); Etalon (Et); Polarize beam splitter (PS).

4. OPITICAL SPECTROSCOPIC STUDY OF GOLD FLURIDE, AuF, AND GOLD CHOLORIDE, AuCl

4.1 Introduction

Halogen elements are well known for their strong electronegativity, such as fluorine (3.98) and chlorine (3.16)[1]. They all have five electrons in the *p*-orbitals and want to accept an electron to from a state noble gas configuration. Gold, on the other hand, with an electronic configuration of [Xe][$4f^{14}$][$5d^{10}$]$6s^1$, is considered to be a good electron donor and form a strong polar bond between Au and X(=F, Cl, …). This simple strong polar bonding between two atoms makes AuX an ideal starting target to step into the world gold-containing molecules. As describing in Chapter 1, the large relativistic effect of gold caused the *6s* orbital to be strongly contracted and energies to be stabilized. In an ideal Au^+X^- molecule, a small relativistic effect is expected because the *6s* electron is transferred to X^- and 6*s* orbital of Au is not occupied. On the opposite side, in an ideal Au^-X^+ molecule, which has 6*s* orbital occupation, strong bond relativistic effects are predicted. Hence, there should be a correlation among the different AuX molecules between the bond polarity and the bond lengths. The reduced dipole moment ($=\mu_{el}/r_e$, where r_e=bond length) is a good standard to probe the relativistic contributions to the bond polarity [28]. In the study of a AuX molecule by itself, its ground state properties (r_e and μ_{el}) are insensitive to the relativistic stabilization of 6*s*-orbital because of the metal-center configuration of Au^+ ($5d^{10}$). However, the relativistic effect in the excited states will be much greater since the

[1] In Pauling scale

metal center Au^+ configuration becomes to be $5d^96s^1$. It is a critical test to predict the electronic structure parameters for both ground and excited states of AuX molecules simultaneously and correctly. Therefore, in this chapter I will introduce my optical spectroscopic study on AuF and AuCl, which are the two most typical AuX molecules, including rotational properties, electronic hyperfine interactions, electric dipole moments (μ_{el}), and magnetic dipole moment (μ_m) of AuF and AuCl.

Experimental studies of AuF and AuCl are both very limited. The first identification of AuF in gas-phase was reported by Saenger and Sun through visible emission spectrum in 1992 [29], whereas the AuCl were measured seventy years earlier by Ferguson using the same method in 1928 when progressions in two bands (labelled as *A* and *B*) were assigned [30]. The first assignment of AuF was accomplished in 2000 with the spectra of $A^1\Pi$–$X^1\Sigma^+$ and $B^1\Sigma^+$–$X^1\Sigma^+$ bands being recorded [31]. In this study the first vibrational parameters for the $X^1\Sigma^+$, $A^1\Pi$, and $B^1\Sigma^+$ states were determined together with the predicted results from a relativistic density functional theory (DFT) calculation. More importantly later the pure rotational study was performed using millimeter and submillimeter-wave spectroscopy to precisely determined the rotational and hyperfine parameters for the ground $X^1\Sigma^+(v=0)$ state of AuF [32]. The most recent works of AuF were performed by Varberg's group using high-resolution laser spectroscopic technique in the visible range [33, 34]. The $A^1\Pi$–$X^1\Sigma^+$ and $B^1\Sigma^+$–$X^1\Sigma^+$ bands were reassigned as [17.7]1–$X^1\Sigma^+$ and [17.8]0^+–$X^1\Sigma^+$ bands. Similarly to the studies on AuF, the $A\Omega=1$–$X^1\Sigma^+$ and $B\Omega=0^+$–$X^1\Sigma^+$ of AuCl were recorded at near Doppler limited resolution using Fourier transform emission by O'Brien *et al* [35] and a pure rotational study were performed later by the Tanimoto's group to determine the

rotational and hyperfine parameters of the $X^1\Sigma^+$ state [36]. No high-resolution studies of AuCl in the visible range have been performed and precise measurement on the fine and hyperfine parameters of both excited states is in progress.

In contrast to the limited number of experimental studies on AuF and AuCl, there have been numerous theoretical predictions on these two molecules. Most of those studies are focused on the prediction of the ground state properties, like bond lengths (r_e), vibrational frequencies(ω_e), and dissociation energies (D_e), for both AuF [31, 37-43] and AuCl [44-49]. However, the prediction of the dipole moment (μ_{el}) were performed using a variety of methods and the results vary dramatically depending upon the approaches [31, 39]. A comparison of several selected predicted values for μ_{el} with my experimental results will be present and discussed in the following subchapters [28].

Theoretical predictions on the excited states of AuF and AuCl are described in the same two papers by Stoll group [39, 50]. Potential energies curves and various spectroscopic parameters (D_e, r_e, μ_{el}, T_e, and ω_e) for the $X^1\Sigma^+$ ground states and nine low-lying excited states were predicted. The energies of the low-lying excited states of AuF and AuCl are presented in Figure 4.1 along with the observed values. It is noteworthy from Figure 4.1 that the large spin-orbit interaction makes the description of the states as $^3\Pi$, $^3\Sigma$ and $^1\Pi$ etc of limited value. Specifically the spin-orbit induced splitting and shifts is larger than the calculated state energy separation in the absence of spin-orbit. The observed values are from the studies of Varberg group [33, 34] and my work [28, 51]. Surprisingly, the observed [17.7]1 and [17.8]0^+ bands of AuF are close to the predicted energies[39] for the $1^3\Pi_{0+}$ and $1^3\Pi_1$ sub-states with different Ω components, but far from the previous

assigned components of $1^1\Pi_1$ and $2^1\Sigma^+$ states. In contrast to AuF, the observed two bands of AuCl are close to the predicted $1^3\Pi_0{}^+$ and $1^3\Pi_1$ sub-states. In addition, the predicted μ_{el} values [39] for the states $X^1\Sigma^+$ of AuF and AuCl are 4.91D and 4.90 D, and those for the $^3\Pi$ states are 2.68D and 1.39 D, respectively. Therefore, it is interesting and necessary to have a comprehensive high-resolution study on the AuF and AuCl to determine the electronic properties and bring experimental insights of the energy states distribution.

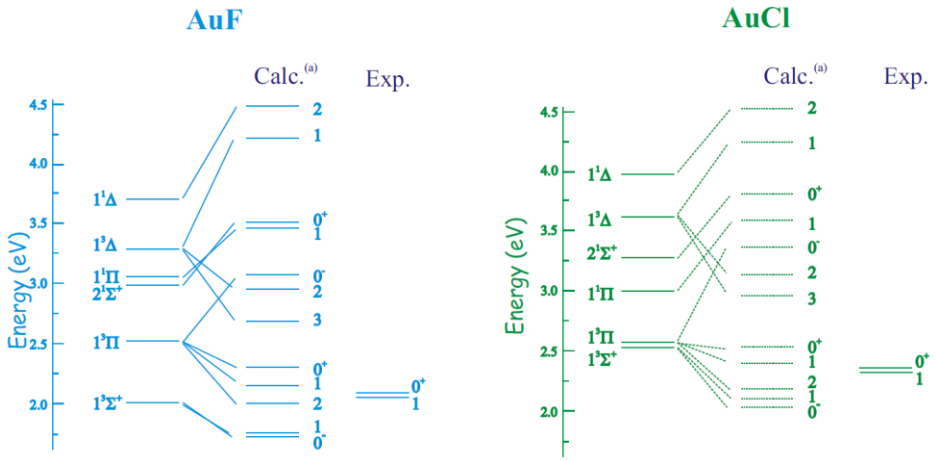

Figure 0.14 The calculated and observed energies for AuF (left) and AuCl (right). Calc. a is from ref. [39].

4.2 Optical Stark and Zeeman study of AuF

Studies of the optical Stark and Zeeman effect were performed on the $[17.8]0^+–X^1\Sigma^+$ band and the permanent electric dipole moment and magnetic hyperfine parameters of the $X^1\Sigma^+$ and $[17.8]0^+$ states were determined [28]. Most parts of the experimental setup have been introduced in Chapter 3. The reacting gas was prepared with 5% sulfur hexafluoride

(SF_6) and 95% argon carrier gas from a backing pressure of approximately 600 Psi. External static electric and magnetic fields were applied.

4.2.1 Observation

Three different lines of the $[17.8]0^+–X^1\Sigma^+$ band, $R(0)$(=17756.156 cm^{-1}), $R(1)$(=17756.642 cm^{-1}) and $P(1)$(=17755.125 cm^{-1}), were selected for optical Stark measurements. In Figure 4.2 the spectra of the $P(1)$ line recorded field-free and in the presence of a 2366 V/cm electric field with parallel ($\Delta M_J = 0$) and perpendicular ($\Delta M_J = \pm 1$) orientation are given on the left. Stark induced shifts were precisely measured by scanning over the field-free and Stark-shifted component consciously with the field turning on or off as illustrate in Figure 4.2. The Stark tuning of the associated energy levels and assigned transitions are presented in right side portion of Figure 4.2. A total of 29 Stark shifts were precisely measured and are presented in Table 4.1 along with the assignments and the difference between the observed and calculated shifts. The calculated shifts were obtained using optimized μ_{el} values of 2.03D and 4.13D for the $[17.8]0^+$ and $X^1\Sigma^+$ states, respectively.

The $R(0)$(=17756.156 cm^{-1}), $R(1)$(=17756.642 cm^{-1}), $R(2)$(=17757.106 cm^{-1}), $P(1)$(=17755.125 cm^{-1}), $P(2)$(=17754.577 cm^{-1}), and $P(3)$(=177554.009 cm^{-1}) lines were selected for optical Zeeman measurements. Zeeman spectra were rescored in a magnetic field of 4650 Gauss with both parallel ($\Delta M_J = 0$) or perpendicular ($\Delta M_J = \pm 1$) orientation. The $R(1)$ and $P(3)$ lines, both of which goes to the same $J = 2$ rotational level of the $[17.8]0^+(v=0)$ excited state, are presented in Figure 4.3. The Zeeman tuning of the associated energy levels and assigned transitions is also presented in Figure 4.3. As expected, no magnetic tuning effect were observed in the rotational levels of the $X^1\Sigma^+$ ($v=0$)

state. The measured shifts and energy level assignment and difference between the observed and calculated shifts are presented in Table 4.2. The calculated results were obtained using in two sets of values: a) ideal values for a non-perturbed $^3\Pi_{0+}$ state (g_S=2.0023 and g_L=1.0); b) optimized values for the [17.8]0^+ states (g_S=2.84 and g_L=1.0).

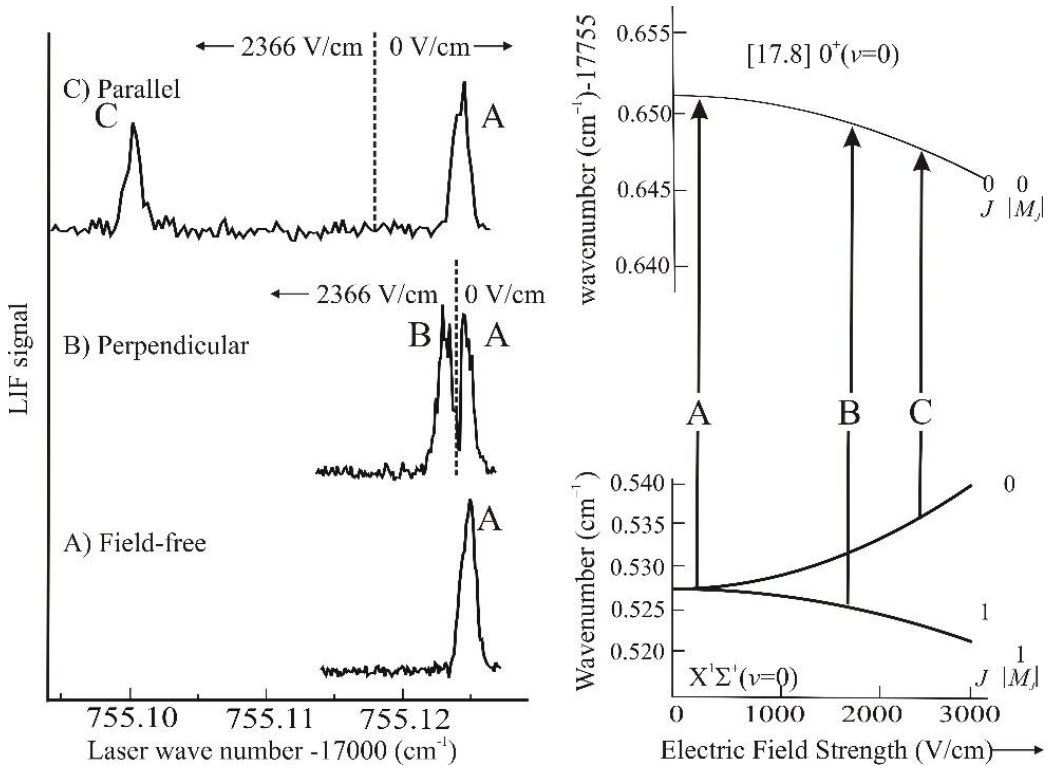

Figure 0.15 The observed and predicted spectra of the *P*(1) line recorded field-free and in the presence of a 2366 V/cm electric field with parallel (ΔM_J =0) and perpendicular (ΔM_J =±1) orientation. The Stark tuning of the associated energy levels and assigned transitions are presented on the right.

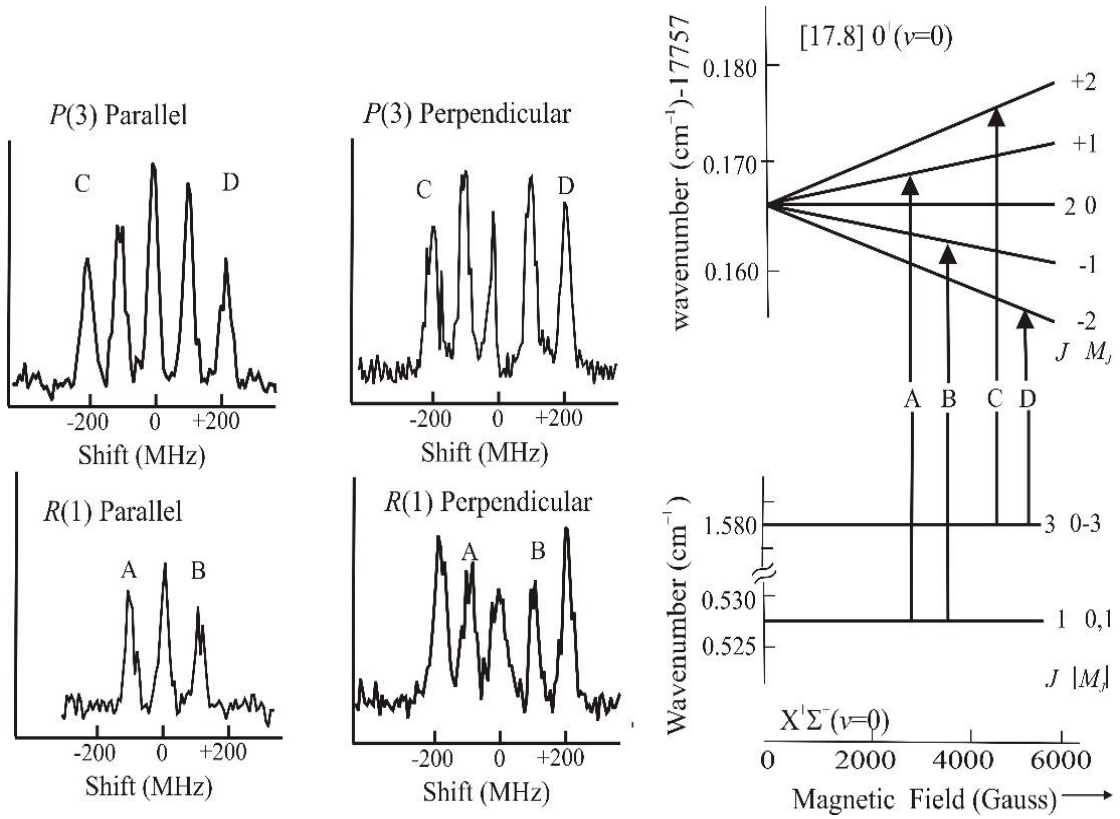

Figure 0.16 The observed and predicted spectra of the *P*(3) and *R*(1) line recorded field-free and in a magnetic field of 4650 Gauss with parallel ($\Delta M_J = 0$) and perpendicular ($\Delta M_J = \pm 1$) orientation. The Zeeman tuning of the associated energy levels and assigned transitions are presented on the right.

Table 0.1 The observed Stark shifts for the $[17.8]0^+–X^1\Sigma^+$ (0, 0) band.

Branch, Pol	Field (V/cm)	Assign.[a]	Shift (MHz)	Obs-Calc[b]
R (0), ‖	2751	A	779	6
	2751	A	775	2
	2745	A	769	0
	2745	A	771	2
	2472	A	619	-8
	2931	A	870	-4
R (0), ⊥	2565	B	522	-17
	2565	B	550	11
	2360	B	460	2
R (1), ‖	1991	A	-220	-22
	1991	A	-224	-26
	2777	A	-366	9
	2366	A	-272	4
	1991	C	135	20
	1991	C	126	11
	1991	C	127	12
	2366	C	160	-2
	2777	C	216	-7
R (1), ⊥	2739	B	-352	25
	2485	B	-310	4
	2490	B	-291	24
	2739	D	184	4
	2485	D	159	11
	2490	D	163	14
P (1), ‖	2366	A	-432	-10
	2745	A	-569	-6
P (1), ⊥	2360	E	30	5
	2360	E	30	5
	2497	E	34	6
	Std. dev. = 12 MHz			

a) A: M_J”=0→ M_J’=0; B: M_J”=0→ M_J’=1; C: M_J”=1→ M_J’=1; D: M_J”=1→ M_J’=2; E: M_J”=1→M_J’=0;

b) Calculated shifts obtained using optimized μ_{el} values of 2.03D and 4.13D for the [17.8]0^+ and $X^1\Sigma^+$ states, respectively.

Table 0.2 The observed Zeeman shifts for the [17.8] 0^+ (v=0) levels.

J, M_J	Obs. Shift (MHz)	Obs-Calc[a] (MHz)	Obs-Calc[b] (MHz)
0, 0	10	-9	-28
1, -1	-89	-45	-40
1, +1	137	46	-4
2, -2	-173	-63	-32
2, -1	-86	-35	-23
2, 0	7	-7	-20
2, +1	119	35	-9
2, +2	233	74	-6
3, -3	-298	-122	-64
3, -2	-195	-80	-43
3, -1	-108	-56	-44
3, 0	0	-14	-28
3, +1	102	19	-24
3, +2	214	60	-14
3, +2	324	97	-12
		Std=63	Std=31
In a magnetic field of 4650 Gauss			

a) Calculated using g_S =2.0023 and g_L=1.0.

b) Calculated using optimized g_S = 2.84 and g_L=1.0.

4.2.2 Analysis

The analysis of the Stark and Zeeman measurement was straightforward since the rotational and hyperfine parameters for the [17.8]0^+ and $X^1\Sigma^+$ states have been determines by previous studies [32-34]. A $^3\Pi$ state description was chosen to model the behavior of the energy levels of the [17.8]0^+ state. Guichemerre et. al [39] predicts an 0^+ state in the energy region near that of the observed [17.8]0^+ state that is primarily the $1^3\Pi_{0+}$ state (as shown in Figure 4.1), which is spin-orbit mixed with the $2^1\Sigma^+$ state, whereas the state is primary the $1^3\Pi_1$ sub-state, which is mixed with the $1^1\Pi_1$ and $1^3\Sigma_1^+$ states. As expected, the spectra did not any hyperfine splitting due to the [17.8]0^+ state. In the absence on hyperfined splitting, the effective Hamiltonian for a $^3\Pi$ state is give as:

$$\hat{\mathrm{H}}^{\mathrm{eff}}(^3\Pi) = T_{v'v''} + A\hat{L}_Z\hat{S}_Z + B\hat{\mathrm{R}}^2 + \frac{2}{3}\lambda\left(3\hat{S}_Z^2 - \hat{\mathbf{S}}^2\right) + \frac{1}{2}(o+p+q)\left(\hat{S}_+^2 + \hat{S}_-^2\right) \qquad (4.1)$$

where the values of A=-2780 cm^{-1}, (o+p+q) = 3520.0 cm^{-1} and λ= 419.3 cm^{-1} are from the fitting of the separations between $1^3\Pi_2$, $1^3\Pi_1$, $1^3\Pi_{0+}$, and $1^3\Pi_{0-}$ sub-states. The rotational constant, B, and Ω-doubling constant, q, are from the experimental values of 0.254cm^{-1} and 0.00324cm^{-1} [34], respectively. The field-free energies were modeled by numerically diagonalizing 6×6 matrices constructed in a Hund's case (a) basis set. Based upon the well characterized field-free energy states, the Zeeman effect was modeled afterwards by numerically diagonalizing 42×42 matrix representation for the J=0-6 rotational levels augmented by the matrix element for $\hat{\mathrm{H}}^{\mathrm{Zee}}$. The initial parameters for predicting the Zeeman shifts were set to g_{L}=1.000, g_{S}=2.002 (i.e. those of a free electron) and $g_\ell = g'_\ell$ = 0.0 assuming that a pure $^3\Pi$ state was observed. However, this resulted in a large standard

deviation of 62 MHz which was significantly larger than the estimated uncertainty (20 MHz) and a large systematic trend in the residuals was observed (as show in the third column of Table 4.2). Various fits using g_L, g_S and g_ℓ as adjustable parameters were attempted. In the end, the set of optimized value with g_L=1.000, g_S= 2.002 g'_ℓ =0 and g_ℓ=0.82 resulted in the residuals given in the fourth column of Table 4.2. The standard deviation of 32 MHz is still slightly larger than the estimated uncertainty (20 MHz) and a slight systematic trend in the residuals remains.

The Stark induced shifts of the energy levels were modeled by including the operator:

$$\hat{H}^{Stark} = -\hat{\mu}_{el} \cdot \vec{E} \qquad (4.2)$$

where $\hat{\mu}_{el}$ is the dipole moment operator and $\vec{E}$ is the applied static electric field vector. 8×8 matrices were generated to represent the J=0-7 rotational levels for both the [17.8]0^+ (v=0) and $X^1\Sigma^+$ (v=0) state and then were numerical diagonalized to produce eigenvalues and eigenvectors. A non-linear least squares fitting was preformed using the observed Stark shifts in Table 4.1 to determine μ_{el} values of 2.03 ± 0.05 D and 4.13± 0.02 D for the [17.8]0^+(v=0) and $X^1\Sigma^+$ (v=0) tates, respectively. The standard deviation of the fitting procedure is around 12 MHz, which is much less than the estimated uncertainty (20 MHz).

4.2.3 Discussion

The determined μ_{el} values for the $[17.8]0^+$ (v=0) and $X^1\Sigma^+$ (v=0) states are listed in Table 4.3 comparing with the selected predicted values from various reference [39, 40, 42, 52]. The prediction results from the high level calculation for the $X^1\Sigma^+$ (v=0) state (i.e., DFT-CCSD, CAM-B3LYP, and CBS-CCSD(T) in Ref. [40] and the DK-AE and SCPP in Ref. [42]) are within ±0.4D (~ 10%) of the experimental values. This relatively good agreement may reflect the expected small relativistic effect for this highly polar molecule as discussed earlier. The μ_{el} value for the $X^1\Sigma^+$ (v=0) state is 4.13(2) D, which is reasonable large due the nature of the bonding's polarity. However, the μ_{el} value for the $[17.8]0^+$ (v=0) state (=2.03±0.05 D) is significantly less than that for the ground state even though the bond distance for the $[17.8]0^+$ state (=1.955 Å) is longer than that of the $X^1\Sigma^+$ state. Different from the configuration of $Au^+(5d^{10})$ center in $X^1\Sigma^+$ state, $Au^+(5d^96s^1)$ of the $[17.8]0^+$ state has an occupation of the 6*s*-orbital. The 6*s*-orbital is more readily back-polarized in comparison to the 5*d* orbital and thus there is a large reduction in the μ_{el} upon excitation [12]. The limited theoretical predictions of the excited state μ_{el} and the disagreement between the results (i.e. 2.68 D in Ref.[39]) and experimental value is a reflection of the inability, and difficulty, of the employed methods to account for the relativistic and polarization effects.

The magnetic tuning observed in the $[17.8]0^+$ (v=0) state is a result of strongly mixing with the [17.7]1(v=0) state, which is only 100 cm^{-1} away from them. The tuning of the energy levels is larger than that expected of an isolated $^3\Pi_1$ state having g_L=1.000 and

g_S = 2.002. This is consistent with the prediction from Guichemerre et al. [39] that the [17.7]1(v=0) state is primarily the $1^3\Pi_1$ sub-state but with mixed contributions from the $^1\Pi$ and $^3\Sigma_1^+$ states. Therefore, the results of g_L =1.000, g_S = 2.002 g_ℓ' =0 and g_ℓ =0.82 were obtained for the magnetic dipole moment for the [17.8]0^+ (v=0) state of AuF.

Table 0.3 The observed and predicted AuF μ_{el} values [39, 40, 42, 52].

Method	μ_{el} (Debye)	Ref.	Method	μ_{el} (Debye)	Ref.
		$X\,^1\Sigma^+$			
Exp.	4.13±0.02				
CBS/CCSD(T)	4.37	[39] a)	DK-AE/LDA	3.585	[42] a)
DFT/LDA	3.58	[39]	DK-AE/PW91	3.578	[40]
DFT/PBE	3.62	[39]	DK-AE/PBE	3.576	[40]
DFT-CCSD(T)/LDA	4.44	[39]	DK-AE/M06	4.317	[40]
DFT-CCSD(T)/PBE	4.43	[39]	DK-AE/B3LYP	4.029	[40]
CAM-B3LYP	4.24	[39]	SC-SRRP-S b)	4.046	[40]
			SC-SRRP-LANL b)	3.939	[40]
			SC-SRRP-CEP b)	4.071	[40]
			LC-SRRP-LANL b)	4.872	[40]
CC-SRPP	4.89 c)	[52]c)			
		[17.8]0^+			
Exp.	2.03±0.05				
CC-SRPP	2.68	[52]c)			

a) Predicted at the experimental R_e value (=1.9184 Å).

b) DFT calculation using the B3LYP functional.

c) Predicted at the theoretical R_e value (=1.95 Å).

4.3 Optical field-free measurement of AuCl

The high-solution spectra of the $[19.07]1 - X^1\Sigma^+$ and $[19.20]0^+ - X^1\Sigma^+$ band systems of gold chloride, AuCl, have been record and analyzed. Precise measurement have been processed to determine the fine- and hyperfine molecular constants.

4.3.1 Observation

Both the spectral features of the $[19.07]1 - X^1\Sigma^+$ and $[19.20]0^+ - X^1\Sigma^+$ sub-bands of AuCl were observed. Portions of the field-free excitation spectrum in the region of the $[19.07]1 - X^1\Sigma^+$ and $[19.20]0^+ - X^1\Sigma^+$ band systems are presented in Figures 4.4, respectively. Gold has only one naturally occurring isotope, ^{197}Au, and chlorine has two, ^{35}Cl (75.7%) and ^{37}Cl (24.3%). The transitions of both isotopologues were observed, but only the spectral features of the main isotopologue, ^{197}Au^{35}Cl, were assigned and analyzed. The energy levels patterns of the $X\,^1\Sigma^+$ state is that of a molecule near the sequentially coupled Hund's case (*b*) limit with a very small splitting due to the ^{35}Cl(I=3/2) nuclear electric quadrupole interaction, eq_0Q(Cl)=-62 MHz, and an even smaller splitting due to ^{197}Au(I=3/2), eq_0Q(Au)=-9 MHz [36].The optical transitions studied here show only slight contributions due to ground state hyperfine splitting and the appropriate quantum numbers for describing the $X\,^1\Sigma^+$ state levels are the rotational angular momentum, N, and it's laboratory projection, M_N. The energy levels pattern of the two excited states of AuCl are treated as a $^3\Pi$ system [39], which is near the energy level pattern expected for a sequentially coupled Hund's case (a_{bJ}) limit. The vector coupling can be written as:

$$J + I_1\,(^{197}\text{Au}) = F_1; \qquad F_1 + I_2\,(^{35}\text{Cl}) = F, \tag{4.3}$$

and the corresponding basis function $|n\Lambda\rangle|S\Sigma\rangle|J\Omega(JI_1)F_1(F_1I_2)F\rangle$ is appropriate for the approximate description of the $^3\Pi$ state. The appropriate quantum numbers for describing the levels are total angular momentum, F, and the projection, M_F, and the intermediate quantum number F_1 and M_{F1} in the case where the small ^{35}Cl(I=3/2) hyperfine interaction is not resolved.

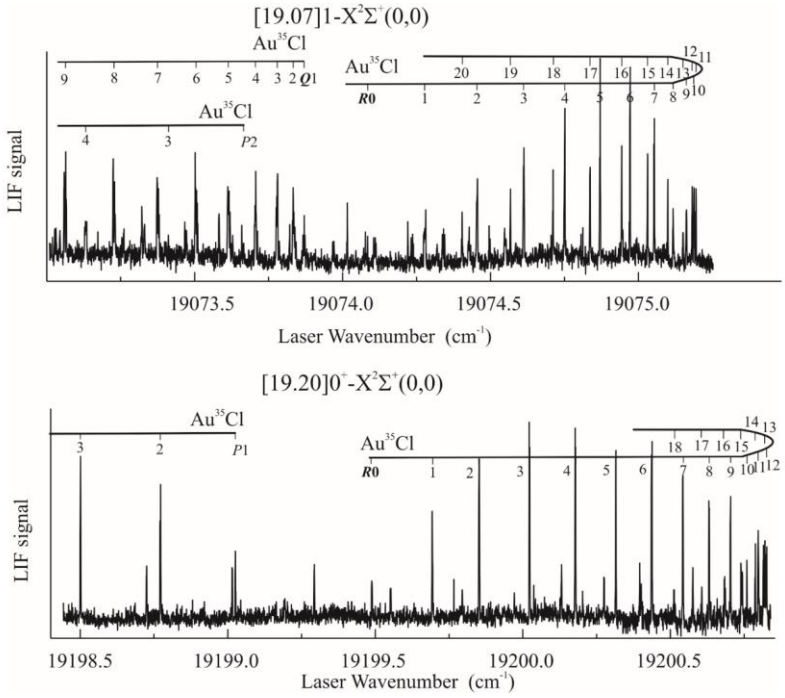

Figure 0.17 Portions of the field-free excitation spectrum in the region of the [19.07]1 – $X^1\Sigma^+$ and [19.20]0^+ – $X^1\Sigma^+$ band systems of AuCl.

The hyperfine splitting in Q-branch of the [19.07]1–$X^1\Sigma^+$ (0,0) band is significantly larger than either the P- or R-branch of the [19.07]1–$X^1\Sigma^+$ (0,0) band or the P- or R-branch of the [19.20]0^+–$X^1\Sigma^+$(0,0) band, indicating a strong parity dependence. This is illustrated in Figure 4.5 where the observed and predicted high-resolution LIF spectra for the $Q_1(6)$(ν= 19073.475 cm^{-1}) and $P_1(7)$(ν= 19071.823 cm^{-1}) branch features of the [19.07]1–$X^1\Sigma^+$ (0, 0)

band are presented. The associated energy levels, obtained using the optimized spectroscopic parameters (see below), and assignments are given in the right-hand portion of Figure 4.5. The upper energy termini of the $Q_1(6)$ and $P_1(7)$ branch features are the *f*-parity and *e*-parity components, respectively, of the $J = 6$ rotational level of the [19.07]1(v=0) spin-orbit state. The complex structure of the $Q_1(6)$ and $P_1(7)$ lines is due primarily to ^{197}Au(I=3/2) hyperfine splitting in the $J = 6$ rotational level of the [19.07]1(v =0) state. The hyperfine structures in the *f*-parity components of the J=6 level of the [19.07]1(v =0) state are well resolved, but those in the *e*-parity components are not. The spread of the hyperfine energy in *e*-parity, ΔE_1, is about 80 MHz, whereas for the *f*-parity level the spread, ΔE_2, is about 225 MHz, which is three time larger. Also shown in Figure 4.5 are the predicted spectra obtained using the optimized spectroscopic parameters in this work.

The energy level pattern in the *f*-parity level (*Q*-branches) varies with the increasing *J*-values as illustrated in Figure 4.6 by the example spectra of the *Q*(3), *Q*(6) and *Q*(15). At low-*J* there are four resolved spectral features, with *F*-values in the sequence of *J*-1.5, *J*+1.5, *J*-0.5, and *J*+0.5 going from high to low energy. However, with increasing rotation the upper two levels (i.e. *F*=*J*-1.5 and *J*+1.5) and the lower two patterns (i.e. *F*=*J*-0.5 and *J*+0.5) become grouped together, and the associate *Q*-branch spectral feature is a doublet, i.e. the spectra features of the *Q*(15) line. The hyperfine pattern also changes quickly upon going to lower-*J* branch features as illustrated in Figure 4.7 where the observed and calculated spectra for the spectra $Q_1(3)$(ν= 19073.750 cm^{-1}) and $P_1(4)$(ν= 19072.810 cm^{-1}) branch features of the [19.07]1–$X^1\Sigma^+$ (0, 0) band are presented. The broadening of the lines is assumed to be due to unresolved ^{35}Cl(I=3/2) hyperfine interaction.

The observed and predicted spectra for $R_0(10)$(ν=19200.758 cm^{-1}), $P_0(10)$(ν=19196.178 cm^{-1}), and $P_0(12)$(ν=19195.368 cm^{-1}) branch features of the $[19.20]0^+–X^1\Sigma^+$ (0,0) band are presented in Figure 4.8. Small hyperfine interactions in the $[19.20]0^+$ (v=0) band were observed. The line positions of 53 transitions in the $[19.20]0^+–X^1\Sigma^+$ (0,0) band and 24 line positions $[19.07]1–X^1\Sigma^+$ (0,0) bands were accurately measured and are present in the Table 4.4 along with the assignments.

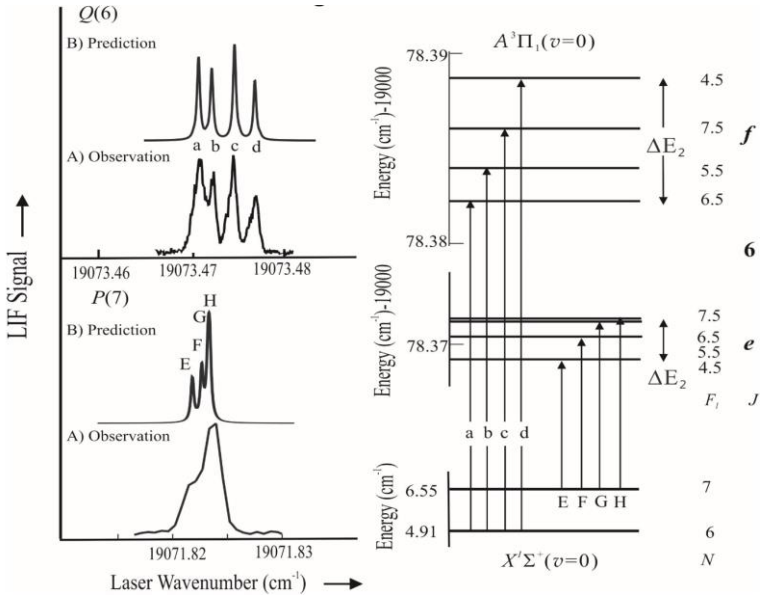

Figure 0.18 The observed and predicted spectra for the $Q_1(6)$(ν= 19073.475 cm^{-1}) and $P_1(7)$(ν= 19071.823 cm^{-1}) branch features of the $[19.07]1–X^1\Sigma^+$ (0, 0) band

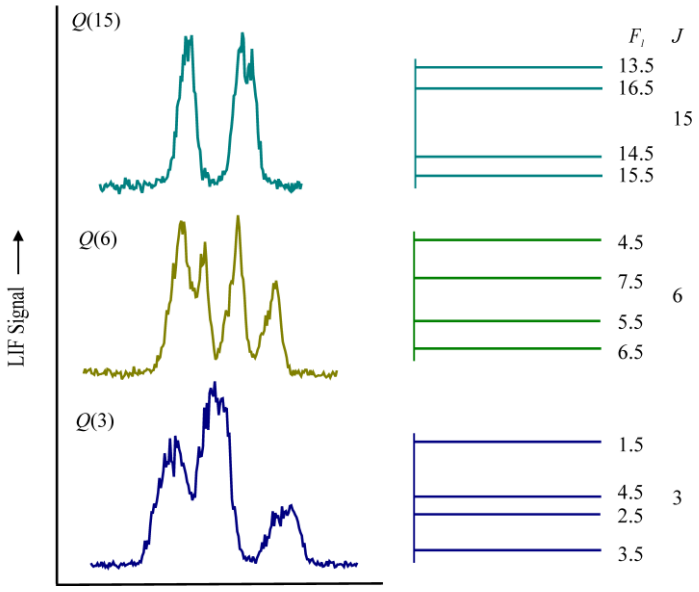

Figure 0.19 The energy level pattern of the $Q(3)$, $Q(6)$, and $Q(15)$ branch features of the [19.07]1–$X^1\Sigma^+$ (0, 0) band

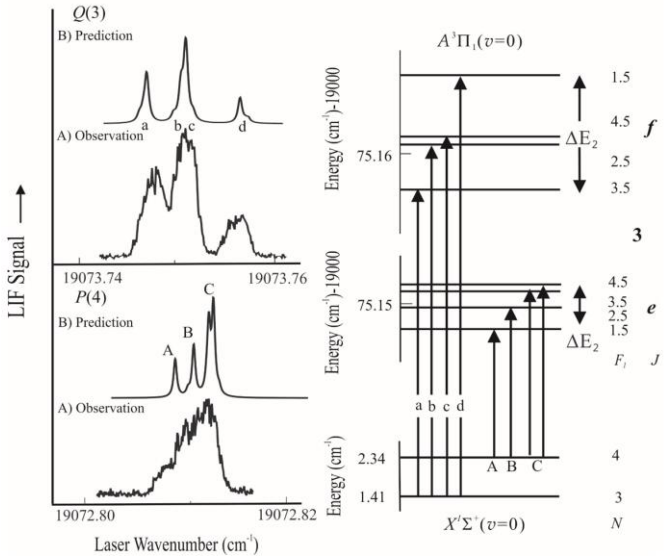

Figure 0.20 The observed and predicted spectra for the $Q_1(3)$ (ν=19073.750 cm^{-1}) and $P_1(4)$ (ν=19072.810 cm^{-1}) branch features of the [19.07]1–$X^1\Sigma^+$ (0, 0) band.

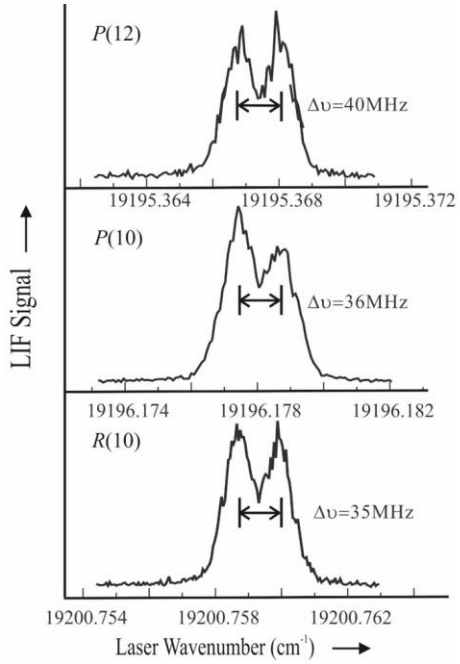

Figure 0.21 High-resolution LIF spectra for the $R_0(10)$(ν=19200.758 cm^{-1}), $P_0(10)$(ν=19196.178 cm^{-1}), and $P_0(12)$(ν=19195.368 cm^{-1}) branch features of the $[19.20]0^+$–$X^1\Sigma^+$ (0, 0) band.

4.3.2 Analysis

As what was done for the AuF study, the $[19.20]0^+$ and [19.07]1 states were treated as components of the $^3\Pi_i$ state, and $X^1\Sigma^+$ (v=0) states of AuCl requires an accurate determination of the relative field-free energies of low-rotational levels. The energies for the $X^1\Sigma^+$ (v=0) state can be accurately predicted using the spectroscopic parameters from previous microwave work [36]. For the $^3\Pi$ (v=0) state, a two stage analysis process is performed similar to that used in the analysis of CuF [23]. The reason of preforming a "two-step" process is because the small relative splitting of a given branch feature, which

arise from the ^{197}Au(I=3/2) and ^{35}Cl(I=3/2) hyperfine interactions in the $^3\Pi$ (v=0) state, can be measured more accurately than the absolute transition wavenumber. Therefore, in the first stage, the hyperfine splitting in the [19.20]0^+(v=0) and [19.07]1(v=0) sub-states were measured by combination/differences and used as input for a least squares optimization of the hyperfine parameters of the $^3\Pi$ state. The fine structure parameters for the $^3\Pi$(v=0) state were held fixed during this stage. In the second stage the measured transition wavenumbers were used as input into a least squares optimization of the fine structure parameters of the $^3\Pi$(v=0) state and the hyperfine structure parameters were held fixed during this stage. The process was repeated for several iterations to get the final set of parameters.

Modelling the energy levels of the $X\,^1\Sigma^+$ states of AuCl was straightforward by including the rotation and its centrifugal distortion, and the quadrupole interaction[20]:

$$\hat{\mathrm{H}}^{\mathrm{eff}}(^1\Sigma) = B_0\hat{J}^2 - D_0\hat{J}^4 + eq_0Q(\mathrm{Cl})\frac{\left(3\hat{I}_z - \hat{\mathbf{I}}^2\right)}{4I(2I-1)} \qquad (4.4)$$

In equation (4.4), J is the angular momentum operator. The rotational, B_0 (=3511.088 MHz), centrifugal distortion correction to rotation, D (=1.3128×10^{-3} MHz), and the quadrupole parameter of chlorine, eQq_0(Cl) (=61.0 MHz) were held fixed at values determined from the analysis of the microwave spectrum [36]. The ^{197}Au(I=3/2) quadrupole coupling parameter, $eq_0Q(\mathrm{Au})$, for the $X\,^1\Sigma^+$ state of AuCl is small (=10 MHz [36])and the effects not detectable in the optical spectra. The eigenvalues and eigenvectors for the $X^1\Sigma^+$ (v=0) state of AuCl were obtained by constructing and diagonalizing a $8 \times 8 = (2S+1)\times(2I_1+1)$)

matrix representation constructed in a one nuclear spin (^{35}Cl(I=3/2)) Hund's case ($a_{\beta J}$) basis set.

For the analysis of the [19.20]0^+ and [19.07]1 states, which are assumed to be components of a $^3\Pi(v=0)$ state, the effective Hamiltonian for fine structure was taken as[20]:

$$\begin{aligned}\hat{\mathrm{H}}^{\mathrm{eff}}(^3\Pi) = T_{v'v''} + A\hat{L}_Z\hat{S}_Z + B\hat{\mathrm{R}}^2 + \frac{2}{3}\lambda\left(3\hat{S}_Z^2 - \hat{\mathbf{S}}^2\right) + \frac{1}{2}(o+p+q)\left(\hat{S}_+^2 + \hat{S}_-^2\right) \\ + \frac{1}{2}(p+q)\left(\hat{S}_-\hat{J}_- + \hat{S}_+\hat{J}_+\right) + \frac{1}{2}q\left(\hat{J}_-^2 + \hat{J}_+^2\right)\end{aligned} \tag{4.5}$$

which included the spin-orbit(A), Λ-doubling(o, p, and q), and spin-spin (λ) fine structure terms. The spin-orbit parameter, A, will be constrained to the predicted values of -2250 cm^{-1} [39] and the (o+p+q) combination of parameters was constrained to 3548 cm^{-1}, which is half the predicted splitting between the predicted $1^3\Pi_{0^+}$ and $1^3\Pi_{0^-}$ sub-states [39]. The observed splitting between the [19.20]0^+ (v=0) and [19.07]1 (v=0) levels of AuCl is approximately 125 cm^{-1}, which is much less than the predicted values of 725 cm^{-1}. Therefore, the spin-spin parameter, λ, was treated as a variable.

The hyperfine structure in the excited [19.07]1 and [19.20]0^+ states of AuCl is primarily due to interaction of ^{197}Au(I=3/2). Modelling of the hyperfine splitting of AuCl was divided into two parts: 1). the magnetic hyperfine Hamiltonian written in terms of the Frosch and Foley parameters [20]:

$$\hat{\mathrm{H}}_{\mathrm{mhf}} = a\hat{\mathrm{I}}_z\hat{\mathrm{S}}_z + b_{\mathrm{F}}\hat{\mathbf{I}}\cdot\hat{\mathbf{S}} + c(\hat{\mathrm{I}}_z\hat{\mathrm{S}}_z - \tfrac{1}{3}\hat{\mathbf{I}}\cdot\hat{\mathbf{S}}) - \tfrac{1}{2}d(\hat{\mathrm{S}}_+\hat{\mathrm{I}}_+ + \hat{\mathrm{S}}_-\hat{\mathrm{I}}_-) \tag{4.6}$$

and 2). the nuclear quadrupole Hamiltonian:

$$\hat{\mathrm{H}}_{\mathrm{Q}} = \frac{eQ}{4I(2I\text{-}1)}\left\{\sqrt{6}q_0\mathrm{T}^2_{q=0}(I,I) + \sum_{q=\pm1}\mathrm{e}^{-2\mathrm{i}q\phi}q_2\mathrm{T}^2_{2q}(I,I)\right\} \qquad (4.7)$$

Details of these two Hamiltonian operators have been introduced in the previous chapters.

The first stage of analysis was achieved by having measured transitions wavenumbers for the [19.07]1-$X^1\Sigma^+$ (0,0) band hyperfine splitting (e.g. the splitting between the "a" ,"b", "c", and "d" *Q*-branch spectral features, and the "A", "B" ,and "C", *P*-branch spectral features Figure 4.4) used as input to a least square fitting procedure of AuCl. The fitting procedure calculated both $X^1\Sigma^+$ energies, using the known parameters, and those for the [19.07]1 using the initial estimates of eQq_0(Au), eQq_2(Au), and a(Au). The eQq_0(Au), eQq_2(Au), and a(Au) parameters were optimized in a standard non-linear least squares procedure. The measured splittings and the differences between the observed and calculated splitting for AuCl are listed in Table 4.5. The optimized eQq_0(Au), eQq_2(Au), and a(Au) parameters are given in Table 4.6.

In the second stage of the fit the input data set consisted of 78 precisely measured optical transition wavenumbers (as shown in Table 4.4) for the [19.07]1 and [19.20]0^+ states. While the hyperfine parameters optimized from the first stage were held fixed, five fine structure parameters of the $^3\Pi$ (v=0) state were optimized in the second stage: $T_{0,0}$, B, p+2q, and q. The data set is primarily low-J and is relatively insensitive to the centrifugal distortion due parameters D and A_D and these parameters were held fixed to the previously determined values [35]. Similarly, the spin orbit constant, A, and the Λ-doubling parameter were constrained to theoretical values (see above). The results of the fitted parameter are listed in table 4.7 with a standard deviation of about 0.0014 cm^{-1}.

Table 0.4 Observed and calculated line positions of the [19.20]0^+–$X\ ^1\Sigma^+$(0,0) and [19.07]1 – $X\ ^1\Sigma^+$(0,0) band system of $^{197}Au^{35}Cl$.

Line	F_1'	F_1''	*Obs.*	Dif.[a] 10^{-4}	Line	F_1'	F_1''	Obs.	Dif.[a] 10^{-4}
$Q_1(3)$	3.5	3.5	^{190}73.7486	-10	$R_1(3)$	5.5	4.5	^{190}74.6096	-1
	2.5	2.5	73.7511	-12	$R_1(4)$	6.5	5.5	74.7478	-13
	4.5	4.5	73.7511	-9	$R_1(5)$	7.5	6.5	74.8696	0
	1.5	1.5	73.7580	59	$R_1(6)$	8.5	7.5	76.9699	-10
$Q_1(4)$	4.5	4.5	73.6748	-8	$R_1(7)$	9.5	8.5	75.0524	-7
	3.5	3.5	73.6779	1	$R_1(8)$	10.5	9.5	75.1155	-9
	5.5	5.5	73.6779	-9	$R_1(9)$	11.5	10.5	75.1601	-5
	2.5	2.5	73.6829	71	$R_1(10)$	12.5	11.5	75.1865	8
$Q_1(5)$	5.5	5.5	73.5828	-5	$P_1(4)$	4.5	5.5	72.8117	5
	4.5	4.5	73.5847	-4	$P_1(5)$	5.5	6.5	72.5022	7
	6.5	6.5	73.5872	3	$P_1(6)$	6.5	7.5	72.1721	-5
	3.5	3.5	73.5909	9	$P_1(7)$	7.5	8.5	71.8240	-5
$Q_1(6)$	6.5	6.5	73.4707	-18	$P_1(8)$	8.5	9.5	71.4571	-3
	5.5	5.5	73.4726	-15	$R_0(0)$	2.5	1.5	^{191}99.4715	15
	7.5	7.5	73.4757	-7	$R_0(1)$	3.5	2.5	99.6730	8
	4.5	4.5	73.4787	-4	$R_0(2)$	4.5	3.5	99.8571	-8
$Q_1(7)$	7.5	7.5	73.3423	-11	$R_0(3)$	5.5	4.5	^{192}00.0271	-4
	6.5	6.5	73.3435	-12	$R_0(4)$	6.5	5.5	00.1801	-8

	8.5	8.5	73.3467	-8	$R_0(5)$	7.5	6.5	00.3174	-5
	5.5	5.5	73.3498	0	$R_0(6)$	7.5	6.5	00.4373	27
$Q_1(8)$	8.5	8.5	73.1948	-10		6.5	5.5	00.4373	19
	7.5	7.5	73.1963	-7		8.5	7.5	00.4386	-1
	9.5	9.5	73.2001	1		5.5	4.5	00.4386	-9
	6.5	6.5	73.2027	6	$R_0(7)$	8.5	7.5	00.5409	17
$Q_1(9)$	9.5	9.5	73.0298	1		7.5	6.5	00.5409	10
	8.5	8.5	73.0311	2		9.5	8.5	00.5422	-11
	10.5	10.5	73.0348	8		6.5	5.5	00.5422	-19
	7.5	7.5	73.0367	8	$R_0(8)$	9.5	8.5	00.6294	18
$Q_1(10)$	10.5	10.5	72.8446	-6		8.5	7.5	00.6294	11
	9.5	9.5	72.8446	-16		10.5	9.5	00.6307	-10
	11.5	11.5	72.8497	1		7.5	6.5	00.6307	-17
	8.5	8.5	72.8515	3	$P_0(3)$	3.5	4.5	^{191}98.5013	4
$Q_1(11)$	11.5	11.5	72.6427	6	$P_0(4)$	4.5	5.5	98.2181	-2
	10.5	10.5	72.6427	-3	$P_0(7)$	6.5	7.5	97.2699	12
	12.5	12.5	72.6474	8		5.5	6.5	97.2699	2
	9.5	9.5	72.6490	10		7.5	8.5	97.2709	-19
$Q_1(12)$	12.5	12.5	72.4209	4		4.5	5.5	97.2709	-30
	11.5	11.5	72.4209	-5					
	13.5	13.5	72.4257	7					
	10.5	10.5	72.6096	9					

Std. dev. = 0.0014 cm^{-1}

[a] The differences between the observed and calculated values using the final set of optimized parameters given in Tables II and IV of text. The parameters for the $X\ ^1\Sigma^+$ were held fixed to those of Ref. [32].

Table 0.5 Observed and calculated hyperfine splitting in the [19.07]1 state of $^{197}Au^{35}Cl$.

Br,J',P	$F_1' - F_1''$	Obs	Obs-calc		*Br,J', P*	$F_1' - F_1''$	Obs	Obs-calc	
			Fit A	Fit B				Fit A	Fit B
Q, 3, *f*	4.5-3.5	85	-83	-15	*Q*, 12, *f*	13.5–12.5	144	-36	-7
Q, 3, *f*	2.5-3.5	85	-42	-11	*Q*, 12, *f*	10.5–12.5	197	11	-1
Q, 3, *f*	1.5-3.5	250	67	-8	*Q*, 12, *f*	10.5–12.5	197	-36	-1
Q, 4, *f*	3.5-4.5	100	58	24	*Q*, 13, *f*	14.5–13.5	147	11	-5
Q, 4, *f*	2.5-4.5	225	31	-16	*Q*, 13, *f*	11.5–13.5	194	-32	1

Q, 5, *f*	4.5-5.5	69	34	6	*Q*, 15, *f*	16.5–15.5	162	9	9
Q, 5, *f*	6.5-5.5	135	-45	5	*Q*, 15, *f*	13.5–15.5	204	-17	15
Q, 5, *f*	3.5-5.5	239	46	8	*R*, 3, *e*	2.5-1.5	30	20	-4
Q, 6, *f*	5.5-6.5	49	19	-4	*R*, 3, *e*	3.5-1.5	57	2	-19
Q, 6, *f*	7.5-6.5	132	-49	-5	*R*, 3, *e*	4.5-1.5	92	4	-15
Q, 6, *f*	4.5-6.5	215	24	-7	*R*, 4, *e*	5.5-2.5	74	30	-6
Q, 7, *f*	6.5-7.5	46	20	0	*R*, 4, *e*	5.5-3.5	49	21	-9
Q, 7, *f*	8.5-7.5	156	-25	15	*R*, 4, *e*	5.5-4.5	26	14	-5
Q, 7, *f*	5.5-7.5	246	36	11	*R*, 5, *e*	6.5-3.5	72	37	8
Q, 8, *f*	7.5-8.5	35	12	-6	*R*, 5, *e*	6.5-4.5	49	25	0
Q, 8, *f*	9.5-8.5	142	-39	-2	*R*, 5, *e*	6.5-5.5	25	12	-4
Q, 8, *f*	6.5-8.5	219	30	9	*R*, 6, *e*	7.5-4.5	70	41	17

Q, 9, *f*	8.5-9.5	20	-1	-16	*R*, 6, *e*	7.5-5.5	50	28	6
Q, 9, *f*	10.5-9.5	137	-44	-9	*R*, 6, *e*	7.5-6.5	20	7	-7
Q, 9, *f*	7.5-9.5	192	4	-13	*R*, 9, *e*	10.5-7.5	65	46	29
Q, 10, *f*	11.5-10.5	155	-25	7	*R*, 9, *e*	10.5-8.5	40	22	6
Q, 10, *f*	8.5-10.5	210	23	9	*R*, 15, *e*	16.5-13.5	50	39	28
Q, 11, *f*	12.5-11.5	144	-36	-6	*R*, 15, *e*	16.5-14.5	30	15	4
Q, 11, *f*	9.5-11.5	197	11	-1	*P*,3,*e*	2.5-1.5	40	12	5
					P,3,*e*	3.5-1.5	77	25	1
					P,3,*e*	4.5-1.5	112	50	4
	Std. Fit A=33 MHz ; Std. Fit B=12 MHz								

Table 0.6 The hyperfine parameters for the $^{3}\Pi_{1}$(v=0) state of $^{197}Au^{35}Cl$.

Parameter	AuCl[a,b]

$a(^{197}\mathrm{Au})$ *e*-parity	0.0039(3)
$a(^{197}\mathrm{Au})$ *f*-parity	-0.0035(5)
eq_0Q (^{197}Au)	-0.0116(5)
eq_2Q (^{197}Au)	0.0199(9)

[a] The determined from the fit of the hyperfine splitting of Table II. The fine structure parameters were held fixed to the values given in Table V.

[b] Numbers in parentheses represent a 2σ error estimate in the last quoted decimal point.

Table 0.7 The determined parameters for modeling the $^3\Pi_i - X^1\Sigma^+$ (0,0) band of $^{197}Au^{35}Cl$.

Parameter	AuCl
$T_{0,0}$	20024.013(1)
A	-2250.0(Fixed)
λ	712.694(1)
B	0.108159(1)
$10^6 \times D$	0.4397(Fixed)
$o+p+2q$	3550(Fixed)
$p+2q$	-0.248(2)
$10^3 \times q$	-0.581(27)
$a(^{197}Au)$	-0.0035(7)
$eq_0Q(^{197}Au)$	-0.0118(13)
$eq_2Q(^{197}Au)$	0.0061(2)

a)All units are cm^{-1}.

b) Numbers in parentheses represent a 2σ error estimate in the last quoted decimal point.

4.3.3 Discussion

The optimized fine and hyperfine structure parameters with associated errors of the $[19.20]0^+$ (v =0) and $[19.07]1$(v =0) states of AuCl are presented in Table 4.7. The assumption of treating the $[19.20]0^+$ (v =0) and $[19.07]1$(v =0) states as components of a

$^3\Pi$ state supported the fact that the two separate states could be fitted together into a $^3\Pi$ model and come up with a set of molecular constants.

For a $^3\Pi_0{}^+$ state, there is no magnetic hyperfine interaction to a first order approximation. This is consistent with the observation of really small hyperfine interaction in the [19.20]0^+ (v =0) state, but large hyperfine interaction in the [19.07]1(v =0) state. The only contribution in the magnetic hyperfine interaction is coming from the "*a*" term in Eq. (4.6). Only the electronic orbital term orbital term, $a\hat{I}_z\hat{S}_z$, has a non-zero expectation value in the Hund's case ($a_{\beta J}$) limit $1^3\Pi_1$ state. As pointed out in Ref. [33], the reasonable estimates suggest that the orbital magnetic hyperfine parameter, *a*, should be a small positive value (≈ 100 MHz), which in our analysis is around 105 MHz. The parity dependent term, $-\frac{1}{2}d(\hat{S}_+\hat{I}_+ + \hat{S}_-\hat{I}_-)$, which has selection rules $\Delta\Omega = \pm 1$ and $\Delta\Sigma = \mp 1$, and mixes the $1^3\Pi_1$ and $1^3\Pi_{0^+}$ states, is not determined (set to zero). It is noted that the observed energy separation between the $1^3\Pi_1$ and $1^3\Pi_{0^+}$ states for AuCl is only approximately 125 cm^{-1} and the contribution to the observed hyperfine splitting from *d* is expected to be negligible.

Unlike the small magnetic hyperfine interaction, the nuclear quadrupole coupling interactions are much larger in the $^3\Pi$ state of AuCl. As given in Eq. 4.7, two terms, eQq_0 and eQq_2, have contributions to the observed hyperfine splitting. The eQq_2 term effects the hyperfine splitting for the *e*-parity and *f*-parity levels in opposite sign, whereas eQq_0 contributes to both parity levels with the same sign. It is illustrated in Figure 4.9 that the observed negligible splitting in the *e*-parity levels (*P*- and *R*- branches) and relatively large

splitting in the *f*-parity levels (*Q*- branch) are coming from the combination of the two terms. For high-*J* branch features of the [19.20]0^+-$X^1\Sigma^+$ (0,0) band, the approximately 40 MHz splitting are coming from the contribution of the eQq_0(Au) term, which gives the value of -0.0118 cm^{-1}.

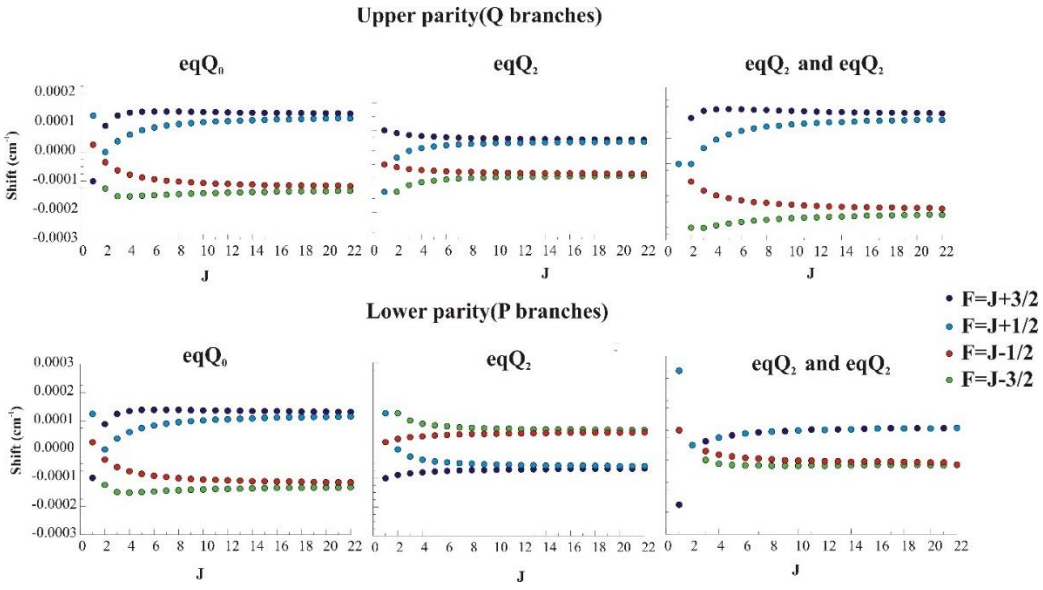

Figure 0.22 The shift of the *F* components varies with increasing J-level with the contribution from the eqQ0, eqQ2 and the combine of the two.

4.4 Optical Stark measurement of AuCl

As a complement to the previous field-free study of AuCl, the [19.20]0^+–$X^1\Sigma^+$ band system of AuCl has been studied using optical Stark spectroscopy. The observed Stark shifts were analyzed to determine the permanent dipole moment, μ_{el}, for the ground and excited states.

4.4.1 Observation

Only the [19.20]0^+–$X\ ^1\Sigma^+$ (0, 0) band of the $^{197}Au^{35}Cl$ isotopologue was studied by optical Stark spectroscopy because the low-J lines of the [19.07]0^+–$X\ ^1\Sigma^+$ (0, 0) sub-band were severely overlapped. The $R_0(1)$ (ν=19199.47 cm^{-1}) line recorded field free and in the presence of a 3686 V/cm with both the "∥" and "⊥" polarizations were employed in Figure 4.10. The energy levels as a function of applied field are also presented. The observed Stark shifts and the differences from the calculated values using the final optimized μ_{el} values are presented in Table 4.8.

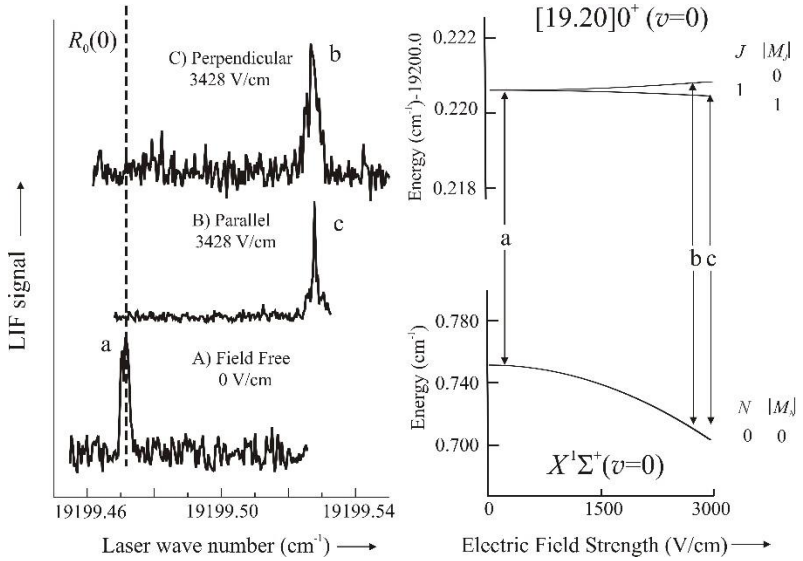

Figure 0.23 The observed and predicted spectra of the $R_0(1)$ (ν=19199.47 cm^{-1}) line recorded field free and in the presence of a 3686 V/cm with both the "∥" and "⊥" polarizations. The associated energy levels as a function of applied field are also given.

4.4.2 Analysis

Analysis of the Stark effect in the $[19.20]0^+ – X\,^1\Sigma^+$ (0, 0) band of AuCl was very similar to that of AuF as I discussed in the previous subchapters. The interaction of the molecule in the static electric field was modelled using the conventional Stark Hamiltonian:

$$\hat{H}^{\text{Stark}} = -\hat{\mu}_{\text{el}} \cdot \vec{E} \tag{4.2}$$

where $\hat{\mu}_{\text{el}}$ is the dipole moment operator and $\vec{E}$ is the applied static electric field vector. A similar procedure of matrices creation and diagonazation was processed to determine the permanent dipole moment, μ_{el}, with values of 3.69 ± 0.02 D and 0.32 ± 0.17 D for the $X\,^1\Sigma^+$ (v=0) and $[19.20]0^+$ (v=0) states, respectively.

Table 0.8 The Stark shifts for the $[19.20]0^+$- $X^1\Sigma^+$(0, 0) band.

Branch, Pol	Field (V/cm)	Assign.[a]	Shift (MHz)	Obs-Calc[b]
R (0), ∥	2285	A	794	-2
	3427	A	1648	-13
R (0), ⊥	1717	B	454	-6
	1717	B	447	-13
	2521	B	956	-13
	3432	B	1638	27
	3432	B	1679	30

	3432	B	1682	11
R (1), ‖	1714	A	-263	3
	2285	A	-450	-3
	2857	A	-656	-3
	3428	A	-879	-8
	1714	C	151	6
	2285	C	253	-2
	2857	C	397	0
	3428	C	553	-14
R (1), ⊥	1714	B	-282	-15
	3428	B	-848	23
	3428	B	-860	11
	1714	D	150	6
	3428	D	563	-1
	3428	D	543	-21
P (1), ⊥	1714	E	119	-20
	3428	E	537	-13

Std. dev. = 14 MHz

[a] A: $M_J''=0 \rightarrow M_J'=0$; B: $M_J''=0 \rightarrow M_J'=1$; C: $M_J''=1 \rightarrow M_J'=1$; D: $M_J''=1 \rightarrow M_J'=2$; E: $M_J''=1 \rightarrow M_J'=0$;

[b] Calculated shifts obtained using optimized μ_{el} values of 3.69D and 0.3178D for the $[19.20]0^+$ and $X^1\Sigma^+$ states, respectively.

4.4.3 Discussion

The experimental values of μ_{el} for the $X\ ^1\Sigma^+$ (v=0) and $[19.20]0^+$ (v=0) states of AuCl and those corresponding values for the $X\ ^1\Sigma^+$ (v=0) and $[17.7]0^+$ (v=0) states of AuF [28] are presented in Table 4.9. It is expected that μ_{el} value for the $X\ ^1\Sigma^+$ (v=0) state of AuCl (=3.69 D) is slightly smaller than that of AuF for the $X\ ^1\Sigma^+$ (v=0) states, where μ_{el} is 4.13D. This result is consistent with the difference in electronegativities of Cl and F as mentioned in the introduction part. However, the large difference between the μ_{el} value for the $[19.20]0^+$ (v=0) stats of AuCl (=0.32D) and the $[17.7]0^+$ (v=0) state of AuF (=2.03D) is unexpected. This inconsistency indicates that there is a considerable differences between the electronic structures of the two excited states.

To better explain and understand the excited electronic structures of the two molecules, a comprehensive computational study preformed Prof. Cheng and Prof. Stanton will be introduced here [51]. As summarized in Table 4.10, among the predicted results for dipole moments of the low-lying excite states of AuCl, only the $^3\Pi$ state has a relative small μ_{el} value which is close to my experimental result. At the same time, the μ_{el} value for the same electronic configuration with a $^3\Pi$ state in AuF is in consistent with my previous study [28]. This theoretical work gives additional evidence that the states of the AuF and AuCl I discussed above are both components of the $^3\Pi$ state.

The reason that the same $^3\Pi$ state behaves extremely different on AuF and AuCl is from their orbital natures. The excitation process from the $X\,^1\Sigma^+$ to the $1^3\Pi$ state is dominated by the $2\pi \rightarrow 3\sigma$ transitions. As shown in Figure 4.10, the 2π orbital is a nearly half-half mixture of the Au $5d_{xz}$ orbital and F $2p_x$ orbital, while the 3σ orbital is mostly localized on the Au atom. Therefore, the charge transfer will result in a reduction on the dipole moment between the $X\,^1\Sigma^+$ and $1^3\Pi$ states. In the case of AuCl, the electron occupation of the 3σ orbital is similar to that of AuF, while the 2π orbital is more localized on the Cl atom (Shown in Figure 4.11). The difference on the occupation between the ground and excited states of AuCl will drive a bigger reduction on the dipole moment of the two states and results in a much smaller μ_{el} value on the $1^3\Pi$ state of AuCl than that of AuF. This effect is even more significant for the bonding of other halogen atoms, like AuBr and AuI, as the results shown in Table 4.11. The $2\pi \rightarrow 3\sigma$ transitions in AuBr and AuI bring more charge densities from the $X\,^1\Sigma^+$ state to the $1^3\Pi$ state, and even flips the sign of the dipole moment in the $1^3\Pi$ state.

Table 0.9 The electric dipole moments of AuCl and AuF (in Debye, D).

	AuCl		AuF	
Method	$X^1\Sigma^+$	$[19.20]0^+$	$X^1\Sigma^+$	$[17.8]\ 0^+$
Experiment	3.69(2)	0.31(17)	4.13(2)	2.03(5)
SFX2C-1e-CC	3.70	0.38	4.27	1.98
MRCI	4.91	1.39	4.90	2.68

Table 0.10 Properties of low-lying excited states of AuCl and AuF calculated at SFX2C-1e/EOM-CCSD/unc-ANO-RCC level. The gold 1*s*, 2*s*, 2*p*, 3*s*, 3*p*, 3*d* electrons were kept frozen in the electron-correlation treatment.

	AuCl		AuF	
	R_e (Å)	μ_{el} (D)	R_e (Å)	μ_{el} (D)
$^3\Sigma$	2.297	1.69	1.978	2.72
$^3\Pi$	2.275	0.38	1.950	1.98
$^3\Delta$	2.361	3.31	2.019	3.59
$^1\Sigma$	2.339	2.30	1.961	2.12
$^1\Pi$	2.296	-0.06	1.975	1.91
$^1\Delta$	2.342	2.80	2.003	3.21

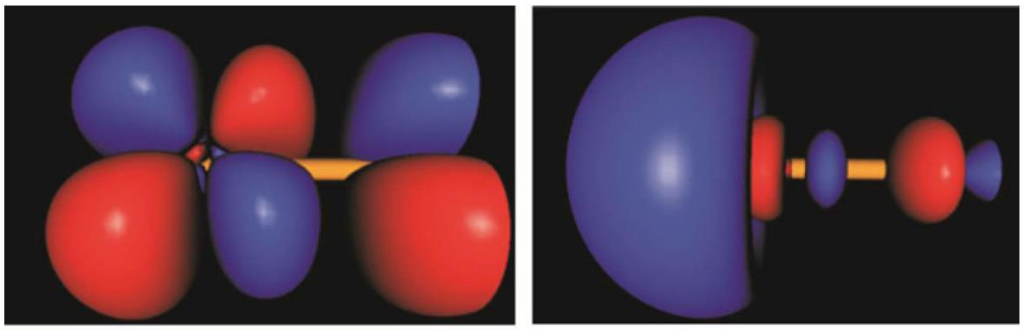

Figure 0.24 The excitation from the ground state to the $^3\Pi$ state of AuF mainly consists of the promotion of an electron from the 2π orbital to the 3σ orbital. In the graphs, the gold atom is placed on the left hand side and the chlorine atom on the right hand side.

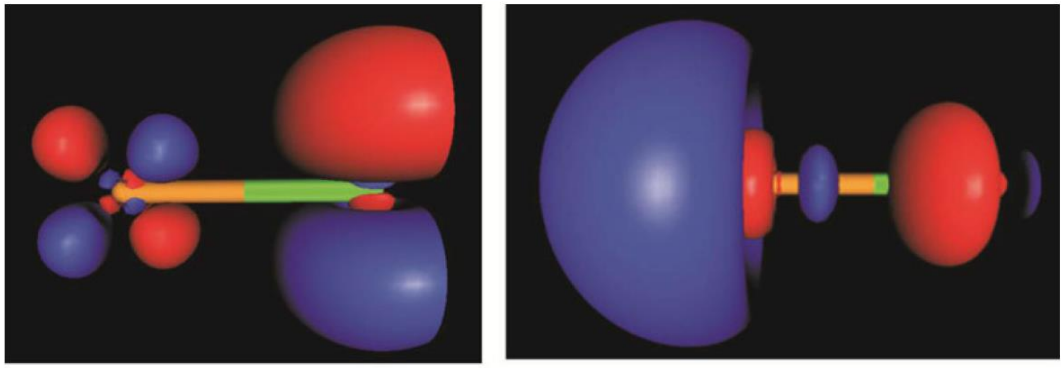

Figure 0.25 The excitation from the ground state to the $^3\Pi$ state of AuCl mainly consists of the promotion of an electron from the 2π orbital to the 3σ orbital. In the graphs, the gold atom is placed on the left hand side and the chlorine atom on the right hand side.

Table 0.11 Properties of the $^3\Pi$ states of AuX (X=F, Cl, Br, and I) calculated at SFX2C-1e/EOM-CCSD/ANO2 level. During the geometry optimization, the 5*d*, 6*s* electrons of

gold and the valence s and p orbitals of halogen were correlated. In the dipole moment calculations, the Au 4*s*, 4*p*, and 4*d* electrons were also included in the electron-correlation treatment.

	R_e (Å)	μ_{el} (D)
AuF	1.959	2.17
AuCl	2.280	0.45
AuBr	2.424	-0.39
AuI	2.636	-1.56

4.5 Summary

In this chapter, the spectroscopic studies have been described on the $[17.8]0^+$-$X^1\Sigma^+$ band of AuF and the $[19.07]1$–$X^1\Sigma^+$ and $[19.20]0^+$–$X^1\Sigma^+$ bands of AuCl. Accurate spectroscopic parameters for the [17.7]1, $[17.8]0^+$ and $X^1\Sigma^+$ states of AuF and [19.07]1, $[19.20]0^+$ and $X^1\Sigma^+$ states of AuCl are determined through high-resolution field-free spectroscopy. Stark measurement were applied for the determination of the dipole moments for ground and excited states of AuF and AuCl. Comparison and discussion were made based upon the results of the hyperfine parameters and dipole moments between the two molecules (See above). Both of these results support the assignments of the [17.7]1 and $[17.8]0^+$ states to components of the $^3\Pi$ state of AuF, and the corresponding [19.07]1 and $[19.20]0^+$ states to components of the $^3\Pi$ state of AuCl.

5. OPITICAL SPECTROSCOPIC STUDY OF GOLD OXIDE, AuO, AND GOLD SULFIDE, AuS

5.1 Introduction

In the previous chapters the spectroscopic studies and bonding properties between gold and halogen have been introduced. In this chapter I will introduce the related work on the nature of the bond between gold and chalcogen, i.e. oxygen (O) and sulfur (S). Understanding the nature of AuO and AuS bonds can provide insight into the expanding field of gold chemistry. For example, the strong affinity of sulfur to gold has been exploited to make molecular contacts in the field of single molecule electronics [53-56]. An individual molecule was attached to gold electrodes via the Au-S bond and the properties of charge transport were investigated via this application. Studies involved Au-S bonding also have applications in the generation of self-assembled monolayers (SAMs) on planar gold surfaces and gold nanoparticles resulting from the interaction with organothiols and disulfides [57-61]. The Au-O bond is also very important highlighted by the recent studies that unsupported nonporous Au shows the activity for low-temperature CO oxidation and is attributed to the uncoordinated Au [62-64].

Elements of the chalcogen group have relatively small electronegativities compared with fluorine and chlorine, with oxygen and sulfur, being 3.44[2] and 2.58[3], respectively. The bonding between gold and oxygen or sulfur is less polar, and more like a covalent

[2] In Pauling Scale
[3] In Pauling Scale

bond. As discussed in the previous chapter, the orbital contraction cause by relativistic effects may lead to a larger reduction of charge transfer to the bonding partner on the covalent bonds than that on the polar bond. Therefore, the effect of reducing the polar character of bonding will be more significant for AuO and AuS, than that of AuF and AuCl. My studies of measuring the permanent electric dipole moment, μ_{el}, is one of the most effective way to understand the polarity of the Au-O and Au-S bond. Given that the 6*s* electrons will be more involved in bonding it is expected that theoretical predations will be more challenging.

Gas-phase spectroscopic studies of AuO and AuS are very limited. The first studies were performed via the photoelectron spectroscopy (PES) on the anions, AuO^- and AuS^-, by Lineberger's group [65] and more recently by Wang's group [66, 67]. The PES studies shows the results that AuO has a $^2\Pi_i$ ground state with a spin-orbit splitting of 1440±80 cm^{-1} and a vibrational frequency of 590±70 cm^{-1}, whereas AuS has the same $^2\Pi_i$ ground state with a spin-orbit splitting of 1280±60 cm^{-1} and a vibrational frequency of 400±30 cm^{-1}. Assignments of numerous excited states were made as well in those PES studies. Pure rotational transitions in the $X^2\Pi_{3/2}$ (v=0) and $X^2\Pi_{3/2}$ (v=1) states of AuO have also been recorded and analyzed by Tanimoto's group to precisely determine the fine and hyperfine parameters [68]. The electronic spectroscopy of AuO has been investigated by O'Brien and co-worker on several different bands at medium spectral resolution [69-72]. Their most recent study utilized intra-cavity absorption spectroscopy of vibrational progressions of the $B^2\Sigma^-$-$X^2\Pi_{3/2}$ transition in the 16900-18900 cm^{-1} spectral region [72].

Unlike the studies on AuO, no previous pure rotational measurement or electronic studies were performed on AuS, until the recent work carried out by our laboratory [73]. In that work the electronic spectrum of AuS covering the 440–740 nm wavelength regions was recorded at medium spectral resolution and analyzed. The electronic spectra were assigned to progressions involving transitions from the ground state to four excited states: $X\,^2\Pi_{3/2} \rightarrow a\,^4\Sigma^-_{3/2}$ (T_e= 12211.08 cm^{-1}), $\rightarrow A^2\Sigma^+$ (T_e=15570.48 cm^{-1}), $\rightarrow B^2\Sigma^-$ (T_e = 16330.02 cm^{-1}), $\rightarrow C\,^2\Delta_{3/2}$ (T_e= 18508.02 cm^{-1}), and $\rightarrow C\,^2\Delta_{5/2}$ (T_e=19010.02 cm^{-1}). The dispersed fluorescence and radiative fluorescence decay curves were also recorded and analyzed.

5.2 Optical field-free and Zeeman study in AuS

The high-resolution spectrum of the $B^2\Sigma^-$–$X^2\Pi_{3/2}$ (0, 0) band of $^{197}Au^{32}S$ in the region 16284 cm^{-1} to 16291 cm^{-1} was recorded field-free and in the presence of a static magnetic field. Fine and hyperfine molecular parameters of AuS in the $X^2\Pi_{3/2}$ (v=0) and $B^2\Sigma$ (v=0) states were precisely determined. Magnetic hyperfine parameters for the $X^2\Pi_{3/2}$ (v=0) and $B^2\Sigma^-$ (v=0) states of AuS were interpreted to gain insight into the nature of the chemical bond. A comparison with the theoretical prediction is made.

5.2.1 Observation

The observed excitation spectra of AuS with the assignments are presented in Figure 5.1. For these transitions, a conventional $^2\Pi$ (case a) - $^2\Sigma^-$ (case b) labeling scheme of $^{\Delta N}\Delta J_{F_i'F_i''}(N'')$ will be used, where the subscript "F_i" (i=1 or 2 for J=N+1/2 or N-1/2) designates the electronic spin components. The "ΔN" superscript is dropped when ΔN=ΔJ.

The transition wavenumbers of the low-rotational branch features of all six branches for the $B^2\Sigma^-$–$X^2\Pi_{3/2}$ (0, 0) band of AuS were precisely measured and are given in Table 5.1 along with the difference between the observed and calculated wavenumbers (see below) and the quantum number assignments.

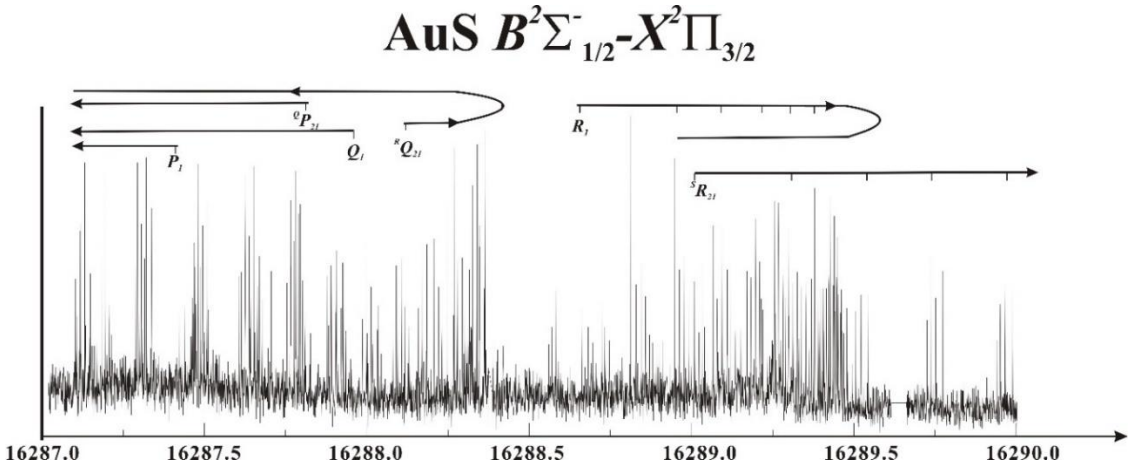

Figure 0.26 The observed excitation spectrum of *the* $B^2\Sigma^-$–$X^2\Pi_{3/2}$ (0, 0) band of AuS in the region 16284 cm^{-1} to 16291 cm^{-1}

The observed and predicted field-free spectra in the region of the $^SR_{21}(5/2)$($\nu\cong$16289.27 cm^{-1}) and R_1 (5/2) ($\nu\cong$19288.84cm^{-1}) lines of AuS are presented in Figure 5.2. In the right-hand portion the associated energy levels and assigned transitions are given. The energy level pattern of the $B^2\Sigma^-$ state is not that of a typical molecule near the Hund's case ($b_{\beta J}$) limit [20]. A typical Hund's case ($b_{\beta J}$) limit $^2\Sigma$ state has widely spaced rotational levels designated by the approximately good quantum number of N (=R). A typical Hund's case ($b_{\beta J}$) has each rotational level consist of a relatively closely spaced doublet (called "ρ-doubling") caused by interaction of the electronic spin angular

momentum, S, with the *N* (referred to as the "spin-rotation interaction). The resulting momentum *J* (=*N*+*S*) is an approximately good quantum number. For a typical Hund's case ($b_{\beta J}$) molecule the ρ-doubling is an order of magnitude smaller than the rotational spacing. In the case of the $B^2\Sigma^-$ state of AuS the ρ-doubling is a comparable to the rotational spacing. The unusually large spin rotation interaction parameter (γ~-0.357 cm^{-1}) relative to the rotational constant (*B*= 0.125 cm-1) cause the *J*=*N*+1/2 level to be in close proximity to the *J*=(*N*+1)-1/2 level (see Figure 5.2). As a consequence the energy level pattern of the $B^2\Sigma^-$ state is very unusual being more similar to a state having non-zero electronic orbital angular momenta (e.g. a $^2\Pi_{1/2}$ state). Note that the *J*=*N*+1/2 and *J*=(*N*+1)-1/2 levels have opposite parity. The coupling between *J* and the ^{197}Au(I=3/2) nuclear spin angular momentum, I, gives a total angular momentum quantum number, *F*, which consists of up to four possible values: *J*-3/2, *J*-1/2 *J*+1/2, and *J*+3/2. As can be seen in Figure 5.2, the magnetic hyperfine splittings in the $B^2\Sigma^-$ state are relatively large and correspondingly so are the hyperfine parameters (b_F=-686(12) MHz, *c*=694(30) MHz). Also note that the combination of the b_F and *c* terms results in the opposite order of the hyperfine patterns between the *J*=*N*+1/2 and *J*=(*N*+1)-1/2 levels have opposite parity those two different parities. The electric quadrupole hyperfine interaction within the $B^2\Sigma^-$ state is relatively small (eQq_0=148 (12) MHz). The hyperfine structure of the spectra presented in Figure 5.2 is primarily due to the $B^2\Sigma^-$ state.

The energy level pattern of the low-rotational levels of the $X^2\Pi_{3/2}$ state of AuS is that of a molecule near the Hund's case ($a_{\beta J}$) limit. It is a Hund's case (*a*) because the electron spin is approximately quantized in the molecular axes frame due to the large spin

orbit coupling (A''≅1300 cm^{-1}) relative to the rotational spacing (B''=0.13156(1) cm^{-1}). It is a "βJ" coupling because nuclear spin, I, is strongly coupled to the angular momentum J. No Λ-doubling was observed for lower rotational levels of the $X^2\Pi_{3/2}$ state of AuS studied here. Therefore, lower rotational levels of the $X^2\Pi_{3/2}$ sub-state consist of two sets of 4 (=2I+1) very nearly degenerate hyperfine levels of opposite parity. In Figure 5.2, some weaker transitions on the shoulder of the stronger features were partially resolved, and these are due to small hyperfine splitting in the $X^2\Pi_{3/2}$ state. The small broadening of the spectral features due to the $X^2\Pi_{3/2}$ state could be modelled using an effective magnetic hyperfine interaction parameter $h_{3/2}$ of -46.01(5) MHz and nuclear electric quadrupole hyperfine parameter eQq_0=182.24(11) MHz. These two parameters were determined by the combination-difference method and the results of the least-square fitting. The effective $h_{3/2}$ parameter is a linear combination of the Frosch and Foley magnetic hyperfine parameters [20]. The determined hyperfine splittings together with calculated difference were listed in Table 5.2. All fitted parameters for both the $X^2\Pi_{3/2}$ and $B^2\Sigma^-$ states of AuS are presented in Table 5.3, with errors associated with them.

Zeeman spectroscopy can provide insight into the nature of the electronic spin and orbital angular momenta and help verify electronic state designations (i.e. Does the $X^2\Pi_{3/2}$ level have Λ=+1 and Σ=1/2?). The observed spectrum in the region of the $^QP_{21}$(5/2) (ν ≅16287.70 cm^{-1}) and P_1 (3/2) (ν ≅19287.82cm^{-1}) lines recorded in the presence of a 328 Gauss magnetic field oriented perpendicular (ΔM_J = ±1) to the electric field of the laser radiation is presented in Figure 5.3. Also presented are the predicted spectra calculated using the determined magnetic g-factors of the $X^2\Pi_{3/2}$ and $B^2\Sigma^-$ states from Table 5.4 for

the tuning of the associated energy levels in the magnetic fields ranging from 0 G to 400 G. The Zeeman tunings in the $X^2\Pi_{3/2}$ state is changing rapidly with the increasing magnetic fields. Due to the small hyperfine interaction in the $X^2\Pi_{3/2}$ state, M_J is the approximately good quantum number, resulting in the splitting of the J=3/2 and J=5/2 level into four and six groups of energy patterns (i.e. M_J varies from M_J =-J to M_J =+J). The large hyperfine interaction in the $B^2\Sigma^-$ state leads to M_F being the approximately good quantum number in the presence of the applied magnetic field for this state. The Zeeman effect in the $B^2\Sigma^-$ state are relatively small comparing with the $X^2\Pi_{3/2}$ state, and observed Zeeman spectral shifts in Figure 5.3 were primarily from the tuning in the ground state. The transition represented by the dashed lines were not present here because they were overlapped with complicated Zeeman shift from other lines. Forty magnetically-induced Zeeman shifts were precisely measured and are presented in Table 5.4 along with the assignments and the difference between the observed and calculated shifts.

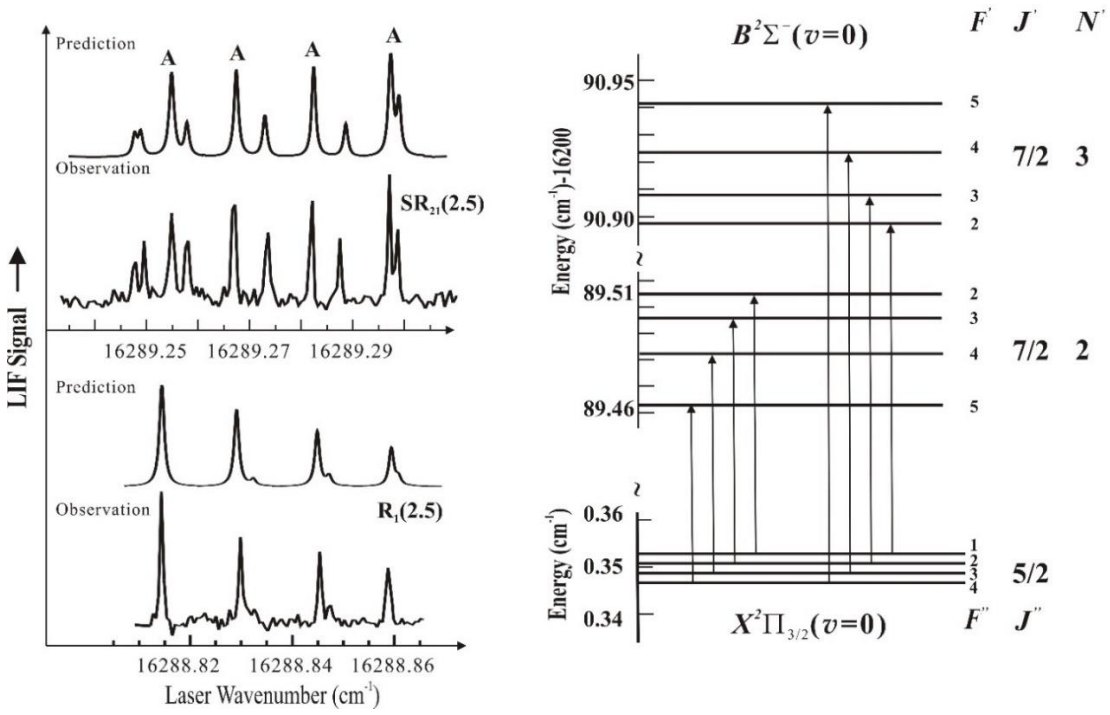

Figure 0.27 The observed and predicted field-free spectra in the region of the $^{S}R_{21}$ (5/2) ($\nu \cong 16289.27\ cm^{-1}$) and R_1 (5/2) ($\nu \cong 19288.84 cm^{-1}$) lines of AuS

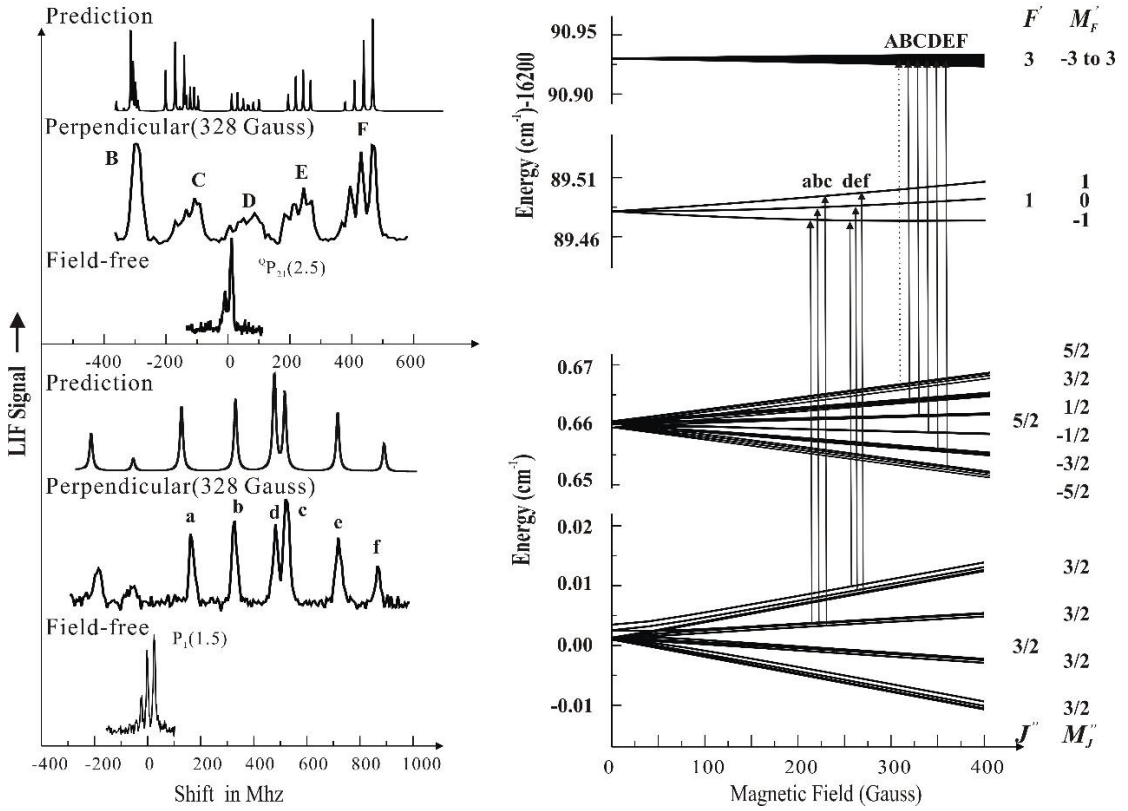

Figure 0.28 The observed and predicted spectra in the region of the $^{Q}P_{21}(5/2)$ ($\nu \cong 16287.70$ cm^{-1}) and P_1 (3/2) ($\nu \cong 19287.82$cm^{-1}) lines recorded field-free and in the presence of a 328 Gauss magnetic field oriented in perpendicular polarization.

Table 0.12 The observed and calculated transition wavenumber (cm^{-1}) for the $B^2\Sigma^- - X^2\Pi_{3/2}$ (0, 0) band system of $^{197}Au^{32}S$.

Line	F_1'	F_1''	*Obs.*	Dif.[a] 10^{-4}	Line	F_1'	F_1''	Obs.	Dif.[a] 10^{-4}
$R_1(3/2)$	3.5	3.5	^{190}73.7486	-10	$R_1(3)$	5.5	4.5	^{190}74.6096	-1
	2.5	2.5	73.7511	-12	$R_1(4)$	6.5	5.5	74.7478	-13
	4.5	4.5	73.7511	-9	$R_1(5)$	7.5	6.5	74.8696	0
$R_1(5/2)$	1.5	1.5	73.7580	59	$R_1(6)$	8.5	7.5	76.9699	-10
	4.5	4.5	73.6748	-8	$R_1(7)$	9.5	8.5	75.0524	-7
	3.5	3.5	73.6779	1	$R_1(8)$	10.5	9.5	75.1155	-9
	5.5	5.5	73.6779	-9	$R_1(9)$	11.5	10.5	75.1601	-5
$R_1(7/2)$	2.5	2.5	73.6829	71	$R_1(10)$	12.5	11.5	75.1865	8
	5.5	5.5	73.5828	-5	$P_1(4)$	4.5	5.5	72.8117	5

	4.5	4.5	73.5847	-4	$P_1(5)$	5.5	6.5	72.5022	7
	6.5	6.5	73.5872	3	$P_1(6)$	6.5	7.5	72.1721	-5
	3.5	3.5	73.5909	9	$P_1(7)$	7.5	8.5	71.8240	-5
$Q_1(6)$	6.5	6.5	73.4707	-18	$P_1(8)$	8.5	9.5	71.4571	-3
	5.5	5.5	73.4726	-15	$R_0(0)$	2.5	1.5	^{191}99.4715	15
	7.5	7.5	73.4757	-7	$R_0(1)$	3.5	2.5	99.6730	8
	4.5	4.5	73.4787	-4	$R_0(2)$	4.5	3.5	99.8571	-8
$Q_1(7)$	7.5	7.5	73.3423	-11	$R_0(3)$	5.5	4.5	^{192}00.0271	-4
	6.5	6.5	73.3435	-12	$R_0(4)$	6.5	5.5	00.1801	-8
	8.5	8.5	73.3467	-8	$R_0(5)$	7.5	6.5	00.3174	-5
	5.5	5.5	73.3498	0	$R_0(6)$	7.5	6.5	00.4373	27
$Q_1(8)$	8.5	8.5	73.1948	-10		6.5	5.5	00.4373	19
	7.5	7.5	73.1963	-7		8.5	7.5	00.4386	-1
	9.5	9.5	73.2001	1		5.5	4.5	00.4386	-9
	6.5	6.5	73.2027	6	$R_0(7)$	8.5	7.5	00.5409	17
$Q_1(9)$	9.5	9.5	73.0298	1		7.5	6.5	00.5409	10
	8.5	8.5	73.0311	2		9.5	8.5	00.5422	-11
	10.5	10.5	73.0348	8		6.5	5.5	00.5422	-19
	7.5	7.5	73.0367	8	$R_0(8)$	9.5	8.5	00.6294	18
$Q_1(10)$	10.5	10.5	72.8446	-6		8.5	7.5	00.6294	11
	9.5	9.5	72.8446	-16		10.5	9.5	00.6307	-10
	11.5	11.5	72.8497	1		7.5	6.5	00.6307	-17
	8.5	8.5	72.8515	3	$P_0(3)$	3.5	4.5	^{191}98.5013	4
$Q_1(11)$	11.5	11.5	72.6427	6	$P_0(4)$	4.5	5.5	98.2181	-2
	10.5	10.5	72.6427	-3	$P_0(7)$	6.5	7.5	97.2699	12
	12.5	12.5	72.6474	8		5.5	6.5	97.2699	2
	9.5	9.5	72.6490	10		7.5	8.5	97.2709	-19
$Q_1(12)$	12.5	12.5	72.4209	4		4.5	5.5	97.2709	-30

Std. dev. = 0.0014 cm^{-1}

[a] The differences between the observed and calculated values using the final set of optimized parameters given in Tables II and IV of text. The parameters for the $X\ ^1\Sigma^+$ were held fixed to those of Ref. ??.

Table 0.13 The observed and calculated Zeeman shifts (MHz) for the lines of the $B^2\Sigma^-$-$X^2\Pi_{3/2}$ (0, 0) band system of $^{197}Au^{32}S$.

Branch	Field[a]	Pol.	M_F'	M_F''	Obs.	Diff.
$R_1(1/2)$	3080	⊥	0	1	-5171	47
			-1	0	-5060	48
			2	1	-1589	17
			1	0	-1404	51
			-2	-1	1583	12
			-1	0	1472	51
			0	-1	5210	-10
			1	0	5082	12
	3080	∥	1	1	-3360	43
			0	0	-3191	62
			-1	-1	3408	3
			0	0	3281	26
	1060	⊥	2	1	-583	-34
			1	0	-393	10
			-2	-1	573	28
			-1	0	469	69
	1060	∥	1	1	-1210	-38
			0	0	-1058	-32
			-1	-1	1218	46
			0	0	1075	48
$Q_1(1/2)$	3080	⊥	0	1	-4351	-26
			-1	0	-4161	10
			0	-1	4303	1
			1	0	4222	74
	3080	∥	1	1	-4301	24
			0	0	-4213	-38
			-1	-1	4308	6
			0	0	4190	39
	1060	⊥	0	1	-1546	-60
			-1	0	-1402	-62
			0	-1	1456	-27
			1	0	1380	43
	1060	∥	1	1	-1538	-52
			0	0	-1387	-46
			-1	-1	1538	55
			0	0	1345	7
$^SR_{21}(1/2)$	1060	⊥	0	1	-1814	-54
			-1	0	-1661	-46
			2	1	-646	-13

			1	0	-492	-4
			-2	-1	674	30
			-1	0	530	31
			0	-1	1823	51
			1	0	1702	75
	1060	∥	1	1	-1231	-35
			0	0	-1052	-2
			-1	-1	1239	-31
			0	0	1115	-52
	3080	⊥	0	1	-5098	-20
			-1	0	-4953	-26
${}^{S}R_{21}(1/2)$	3080	⊥	2	1	-1806	2
			1	0	-1662	-4
			-2	-1	1904	-3
			-1	0	1710	-39
			0	-1	5260	75
			1	0	5060	25
	3080	∥	1	1	-3431	8
			0	0	-3270	18
			-1	-1	3528	-18
			0	0	3399	3
$R_2(1/2)$	3080	⊥	-1	0	3036	-30
			0	1	3203	-17
			1	0	6357	29
			2	1	6475	-13
	3080	∥	-1	-1	2622	-54
			0	0	2977	27
			0	0	4639	-61
			1	1	4801	-53
	1060	⊥	-1	0	774	-15
			0	1	978	40
			1	0	1965	50
	1060	∥	-1	-1	446	21
			0	0	715	29
			0	0	1327	-25
			1	1	1530	29
${}^{R}Q_{21}(1/2)$	3080	⊥	-1	0	-6115	33
			-2	-1	-5746	69
			1	0	-2848	24
			0	-1	-2494	45
			2	1	-1617	22
			1	0	-1297	8
			-2	-1	1023	-11

			-1	0	1325	16
	3080	∥	0	0	-4503	3
			-1	-1	-4165	8
			1	1	-3270	-3
			0	0	-2932	0
			2	2	-1851	-36
			1	1	-1709	-44
			-2	-2	-1898	-7
			-1	-1	-1881	5
	1060	⊥	2	1	-574	-66
			1	0	-250	-58
	1060	∥	0	0	-1310	-50
			-1	-1	-991	-43
			2	2	-668	-33
			1	1	-516	-25
			-2	-2	663	17
			-1	-1	629	9

a) Magnetic field in Gauss.
b) Standard deviation of fit: 37 MHz

5.2.2 Analysis

The analysis of the field-free spectrum was performed in a two-steps method. In the first step, the precisely measured splitting between the components in the observed branch features of the low-*J* lines were used as input into a least squares fitting procedure to optimize the $X^2\Pi_{3/2}$ state hyperfine parameters $h_{3/2}(= a +(b_F+c)/2)$ and eQq_0. In the second step the ground state hyperfine parameters were held fixed and the transition wavenumbers were least squares fitted to produce an optimized set of hyperfine structure parameters of the $B^2\Sigma^-$ state and fine structure parameters for both of states.

In $^{197}Au^{32}S$ the hyperfine interactions in the $X^2\Pi_{3/2}$ and $B^2\Sigma^-$ states are only due to the ^{197}Au(I=3/2). Modelling the hyperfine structure in the $X^2\Pi_{3/2}$ state of AuS consists of two parts: the magnetic hyperfine Hamiltonian and the nuclear quadrupole Hamiltonian.

The magnetic hyperfine Hamiltonian written in terms of the Frosch and Foley parameters is [20]:

$$\hat{H}_{mhf} = a\hat{I}_z\hat{S}_z + b_F\hat{I}\cdot\hat{S} + c(\hat{I}_z\hat{S}_z - \tfrac{1}{3}\hat{I}\cdot\hat{S}) \qquad (5.1)$$

where $\hat{S}_{\pm}$ and $\hat{I}_{\pm}$ are the shift operators of the total electron spin, S, and nuclear spin angular momentum, I. The magnetic hyperfine parameters, *a*, b_F, *c* and *d*, are averages over the spatial coordinates of the unpaired electrons. In the Hund's case ($a_{\beta J}$) limit the energy contribution due to the magnetic hyperfine interactions in the $^2\Pi_{3/2}$ spin-orbit component is given by [20]:

$$E^{hyf} = \frac{3h_{3/2}(F(F+1) - I(I+1) - J(J+1)}{4J(J+1)}. \qquad (5.2)$$

where $h_{3/2}$ is a linear combination of the Frosch and Foley magnetic hyperfine parameter, *F, I,* and *J*= total, nuclear spin, and total in the absence of nuclear spin angular momenta quantum numbers. The energies of the $^2\Pi_{3/2}$ spin-orbit are insensitive to the parity dependent term magnetic hyperfine term, *d.*

Modelling of the nuclear quadrupole hyperfine interaction in AuS is the same as AuCl and AuF which I introduced in the previous chapter. The general form of the nuclear quadrupole nuclear quadrupole Hamiltonian is given as [20]:

$$\hat{H}_Q = \frac{eQ}{4I(2I\text{-}1)}\left\{\sqrt{6}q_0 T^2_{q=0}(I,I) + \sum_{q=\pm1} e^{-2iq\phi} q_2 T^2_{2q}(I,I)\right\} \qquad (5.3)$$

As indicated in Eq. 5.3 there are generally two parameters: the diagonal eQq_0 term and an off-diagonal eQq_2 term. In the present study the data set was only sensitive to the eQq_0 term. Under these conditions Eq. 5.3 reduces to

$$\mathbf{H}^{Quad.}(X\,^2\Pi_{3/2}) = eQq_0\,\frac{(3\hat{I}_Z - \hat{\mathbf{I}}^2)}{4\mathrm{I}(2\mathrm{I}-1)} \qquad (5.4)$$

The first stage of analysis was achieved by having measured transitions hyperfine splitting for the $X^2\Pi_{3/2}$ (v=0) state used as input to a least square fitting procedure of AuS. The initial estimates of the AuS parameters for the fitting were taken as the measured parameters for the same $X^2\Pi_{3/2}$ (v=0) state of AuO [68]. The eQq_0(Au) and $h_{3/2}$(Au) parameters were optimized in a standard non-linear least squares procedure. The determined splittings and the differences between the observed and calculated splitting for $X^2\Pi_{3/2}$ (v=0) state of AuS are listed in Table 5.2.

With determined hyperfine parameters for the $X^2\Pi_{3/2}$ state of AuS, the modeling of the energy levels of the $X^2\Pi_{3/2}$ state was straightforward by adding to Eqs. 5.1 and 5.4 the spin-orbit interaction, and rotation, [20]:

$$\mathbf{H}^{eff}(X\,^2\Pi_{3/2}) = A\hat{L}_z\hat{S}_z + B\hat{\mathbf{N}}^2, \qquad (5.5)$$

where A is the spin-orbit parameter, and B is the rotational constant. An 16 × 16 matrix representation was constructed in a Hund's case ($a_{\beta J}$), nonparity basis set, ψ(case $a_{\beta J}$) = $\left|\mathrm{n}\Lambda;S\Sigma;(\mathrm{JI})\Omega\mathrm{FM}_F\right\rangle$, and diagonalized to produce the eigenvalues and eigenvectors for the $X^2\Pi_{3/2}$ state.

The energy levels of the $B^2\Sigma^-$ state were modeled by including the rotation and its centrifugal distortion, the spin-rotation, the proton magnetic hyperfine, and nuclear electric quadrupole interactions [20]:

$$\mathbf{H}^{eff}(^2\Sigma) = B\mathbf{N}^2 - D\mathbf{N}^4 + \gamma\mathbf{N}\cdot\mathbf{S} + \tfrac{1}{2}\gamma_D\left[\mathbf{N}\cdot\mathbf{S},\mathbf{N}^2\right]_+ + b_F\mathbf{I}\cdot\mathbf{S} + c(I_zS_z - \tfrac{1}{3}\mathbf{I}\cdot\mathbf{S}) \qquad (5.6)$$

where N is the angular momentum operator excluding the electronic and nuclear spin, S and I, respectively, and $\left[\mathbf{N}\cdot\mathbf{S},\mathbf{N}^2\right]_+$ indicates the anti-commutator. An 8 × 8 matrix representation was constructed in a Hund's case ($a_{\beta J}$) nonparity, basis set, ψ(case $a_{\beta J}$) = $\left|\mathrm{n}\Lambda;S\Sigma;(\mathrm{JI})\Omega\mathrm{FM}_F\right\rangle$, and diagonalized to produce the eigenvalues and eigenvectors for the $B^2\Sigma^-$ states. A nonlinear least-squares fitting procedure program was written to optimize the parameters for the $B^2\Sigma^-$ state and the fine structure parameters for the $X^2\Pi_{3/2}$ state. The determined parameters and associated errors are presented in Table 5.3. The standard deviation of the fit (= 0.0011 cm^{-1}) is commensurate with estimated measurement uncertainties of the field-free spectrum.

Similar to the previous AuF study, the effective Zeeman Hamiltonian was taken as [20]:

$$\begin{aligned}\hat{\mathbf{H}}^{Zee}(eff) = {} & g_S\mu_B\hat{\mathbf{S}}\cdot\hat{\mathbf{B}} + g_L'\mu_B\hat{\mathbf{L}}\cdot\hat{\mathbf{B}} + \\ & g_\ell\mu_B(\hat{S}_x\hat{B}_x+\hat{S}_y\hat{B}_y) + g_\ell'\mu_B(e^{-2i\varphi}\hat{S}_+\hat{B}_+ + e^{+2i\varphi}\hat{S}_-\hat{B}_-)\end{aligned} \tag{5.7}$$

The eigenvalues and eigenvectors of the $X^2\Pi_{3/2}$ (v=0) and $B^2\Sigma^-$ (v=0) states were determined by diagonalization of a 64×64 and 64×64 matrix representations, respectively, constructed using the Hund's case ($a_{\beta J}$) basis set functions for $F \leq 7$ level. The 113 magnetically-induced Zeeman shifts (Table 5.4), and initial estimates for g-factors for the $B^2\Sigma^-$ (v=0) and $X^2\Pi_{3/2}$ (v=0) states were used as input for a nonlinear least square fitting procedure. Numerous least squares fits were performed in an attempt to optimize various combinations of g_S, g_L, g_l and g_1'. To within the estimated error, the optimized values for

g_L did not deviate from that9 expected for a free electron and g_l and g_l' were =0 for the $X^2\Pi_{3/2}$ (v=0) state . It was determined that g_S=2.150(1), and g_L =1.000(fixed) for the $X^2\Pi_{3/2}$ (v=0) state and g_S=2.671(2) and g_l =–1.616(4) for the $B^2\Sigma^-$ (v=0) resulted in a standard deviation of a fit (= 40 MHz) consistent with the experimental measurement uncertainty.

The predicted spectra, such as those given in Figures 5.1-3, were obtained by co-adding the individual spectral features obtained using a rotational temperature of 10 K and a Lorentzian linewidth of 30 MHz full width at half maximum. The prediction used a slightly higher resolution than actually observed in order to reveal underlying structure.

Table 0.14 The determined spectroscopic parameters from the analysis of the $B^2\Sigma^-$-$X^2\Pi_{3/2}$ (0, 0) band system of $^{197}Au^{32}S$ transition wavenumbers (Table 5.1).

$X^2\Pi_{3/2}$	
B''	0.13155(1)
$D''(\times10^7)$	0.64(1)
$h_{3/2}''$	-0.00261(5)
eq_0Q''	0.0027(1)
$B^2\Sigma^-$	
B'	0.12347(1)
$D'(\times10^7)$	0.54(1)
γ'	0.35460(6)
$g_D'(\times10^5)$	-1.18(6)
b_F'	-0.0216(4)
c'	0.027(1)
eq_0Q'	0.0062(4)
T_{00}'	15638.0666(2)

Table 0.15 The determined magnetic g-factor for the $B^2\Sigma^-$(v=0) and $X^2\Pi_{3/2}$ (v=0) states of AuS.

$X^2P_{3/2}$

g_S	2.150(1)
g_L	1.00(fixed)
B^2S^-	
g_S	2.671(2)
g_l	1.616(4)

5.2.3 Discussion

The lowest rotational features of the $B^2\Sigma^- – X^2\Pi_{3/2}$ (0, 0) band of AuS have been detected and analyzed for the first time. The hyperfine interaction observed in the $X^2\Pi_{3/2}$ state is determined small. The magnetic hyperfine parameter $h_{3/2}$ (=-46.01(8) MHz) and nuclear quadrupole parameters eQq_0 (=182.24(11) MHz) of AuS have been determined precisely using the combination-difference fitting process. These values are consistent with the previous determined parameters for the $X^2\Pi_{3/2}$ state of AuO ($h_{3/2}$=-48.10 MHz, eQq_0= 188.11 MHz) which come from the microwave measurement [68]. Unlike the small hyperfine interaction in the ground state, the $B^2\Sigma^-$ (v=0) state has a relative large magnetic hyperfine interaction (b_F = -647(11) MHz, c=809(30) MHz) and somewhat smaller nuclear quadrupole interaction (eQq_0 =146(10) MHz).

The determined anisotropic Zeeman parameter, g_l, for the $B^2\Sigma^-$ (v=0) state can be qualitatively understood. This parameter is introduced into the effective Hamiltonian to account for spin-orbit and rotational mixing of electronic states. Such mixing is extensive for the $B^2\Sigma^-$ (v=0) state due to the density of excited states and the large spin-orbit interaction. The major contribution to the spin-rotation parameter, γ, also comes from state mixing and the two parameters are related by the Curl relationship [23]:

$$g_l \approx -\gamma/2B, \tag{5.8}$$

where γ and B, are the spin-rotation and rotational parameters. Using the experimentally determined parameters (γ=0.357 cm^{-1} and B=0.126 cm^{-1}) from Table 5.5 gives g_l ($B^2\Sigma^-$) =-1.41, which is in the same sign and close to the experimental determined value(g_l=-1.62).

It is more difficult to rationalize why the determined g_S parameters of $B^2\Sigma^-$ (v=0) state(=2.67), and the $X^2\Pi_{3/2}$ (v=0) state(=2.15) deviate so markedly from that expected for a free electron (=2.0023). We are currently working with Prof. Lan Chang (Johns Hopkins) in effort to shed light on this mystery. The analysis for the high-solution field-free spectra of the $B^2\Sigma^-$–$X^2\Pi_{3/2}$ (0, 0) band of AuO was very similar to that of AuS. This is at the limit of an "effective Hamiltonian" approach which is a perturbation approximation.

5.3 Optical Stark measurement of AuO and AuS

The observed Stark shifts in the $B^2\Sigma^-$–$X^2\Pi_{3/2}$ (0, 0) band system of AuS and AuO were analyzed to determine the permanent dipole moment, μ_{el}, for the ground states of the two molecules. It is expected that μ_{el} values for the two molecules should be very similar.

5.3.1 Observation

Due to complexity and congestion of spectra caused by the strong hyperfine interaction of ^{197}Au(I=3/2), only very few lines of both AuS and AuO were suitable for Stark measurement. The observed Stark tuning in the $X^2\Pi_{3/2}$ (v=0) state of both AuO and AuS are very rapidly, due to the near degeneracy of levels of opposite parity (Λ-doublets). In contrast the energy levels of opposite parity in the $B^2\Sigma^-$ (v=0) states are well separated

and there was no evidence of observed spectral Stark shifts due to the contribution of these levels for the relatively low electric fields employed in the current study .

The $Q_{21}(3/2)$ (ν =16899.26 cm^{-1}) and $P_1(3/2)$ (ν =16897.43cm^{-1}) lines in the $B^2\Sigma^- – X^2\Pi_{3/2}$ (0, 0) band of AuO were selected for optical Stark measurements. The observed and predicted field-free and Stark spectra for the $P_1(3/2)$ line of AuO are presented in Figure 5.4 associated with the energy levels and quantum number assignments. The predicted spectra and simulated energy level shifts were obtained using the optimizing parameter. The F=2 and F=1 hyperfine components of the N=0, J=1/2 level in the $B^2\Sigma^-$ (v=0) state are well separated by 450 MHz and stay constant with the applied electric field. The lower energy patterns for the $X^2\Pi_{3/2}$ (v=0), J=3/2 level are much more complicated as a function of applied electric field. The nuclear spin angular momentum, $\vec{I}$, remains coupled to the rotational angular momentum, $\vec{\mathbf{J}}$, over the applied field range, making the projection of total angular momentum, M_F, to be the only appropriate quantum number. Therefore, the selection rules are $\Delta M_F = 0$ for the parallel polarization and $\Delta M_F = \pm 1$ for the perpendicular polarization, respectively. The 24 Stark shifts of AuO were precisely measured and presented in Table 5.5 along with the quantum number assignments and difference between the observed and calculated values.

Similar to the $B^2\Sigma^- – X^2\Pi_{3/2}$ (0, 0) band of AuO, only the $F'' = 4, 3 \rightarrow F'$=3 components of the ${}^{Q}P_{21}(5/2)$ (ν =16287.7022 cm^{-1}) line and the $F'' = 4 \rightarrow F'$=3 component of the $R_1(3/2)$ (ν =16288.6629 cm^{-1}) line of AuS are suitable for Stark measurements. The observed field-free spectrum and the predicted and observed Stark

spectra for the $^{Q}P_{21}(5/2)$ transition with the associated energy levels and Stark tuning are given in Figure 5.5. Exactly the same as the upper energy terminus of AuO, the hyperfine components of the N=2, J= 3/2 level in the $B^2\Sigma^-$ (v=0) state of AuS are well separated and have no Stark tuning in the applied field. However, unlike the lower energy level pattern for AuO, the applied electric field (i.e. 600 V/cm) is sufficient to uncouple the nuclear spin angular momentum, $\vec{\mathbf{I}}$, from the rotational angular momentum, $\vec{\mathbf{J}}$. Therefore, the appropriate approximately good quantum numbers are transformed from F and M_F at low field to M_J and M_I at high field in the presence of the electric field. This leads to a result of energy level patterns in 6 groups due to M_J in the high field as shown in Figure 5.5. The difference of the coupling case between AuO and AuS are due to the fact that the hyperfine splitting for the J=5/2 level of AuS (≅ 69 MHz) is significantly smaller than that for the J=3/2 level of AuO (≅ 155 MHz). The spectral Stark shifts of 68 features for AuS were precisely measured and presented in Table 5.6 with the quantum number assignments and difference between the observed and calculated values.

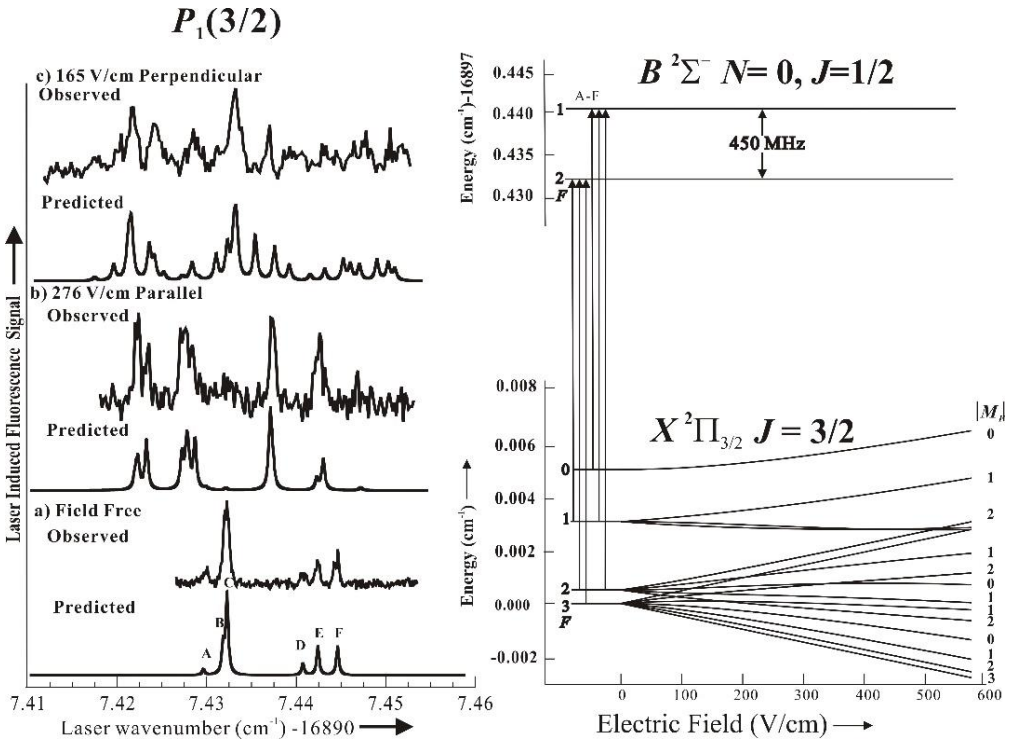

Figure 0.29 The observed and predicted spectra of the $Q_{21}(3/2)$ (ν=16899.26 cm^{-1}) and $P_1(3/2)$ (ν=16897.43cm^{-1}) lines in the $B^2\Sigma^- – X^2\Pi_{3/2}$ (0, 0) band of AuO recorded both field-free and in the present of electric field

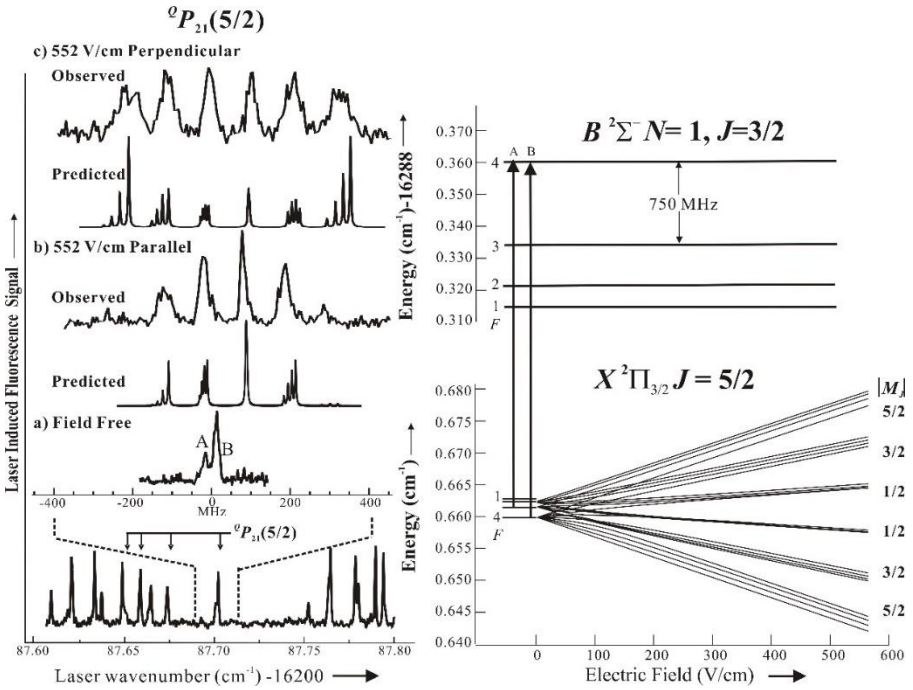

Figure 0.30 The observed and predicted spectra of the $^{Q}P_{21}(5/2)$ (ν=16287.7022 cm^{-1}) $R_1(3/2)$ (ν=16288.6629 cm^{-1}) lines in the $B^2\Sigma^- – X^2\Pi_{3/2}$ (0, 0) band of AuS recorded both field-free and in the present of electric field

Table 0.16 The observed and calculated Stark shifts of lines in AuO.

Branch, pol.	Field (V/cm)	F'	M_F'	F''	M_F''	Obs[a] (MHz)	Dif[b] (MHz)
$Q_{21}(3/2)$,⊥	138.0	0	0	1	1	-72	4.3
	193.0	3	2	3	1	32	1.3
		3	3	3	2	-62	-13.2
		1	1	1	0	-116	4.4
	221.0	0	0	1	1	-142	1.2
		1	1	0	0	-144	5.0
		3	2	3	1	179	-10.4
$Q_{21}(3/2)$, ‖	55.2	3	3	3	3	-39	10.0
		3	-3	3	-3	39	-10.0
	110.4	3	3	3	3	-93	4.8
		3	-3	3	-3	93	-4.9
	165.7	3	3	3	3	-152	-5.0

		221.0	3 3 3	-3 3 -3	3 3 3	-3 3 -3	152 -197 197	4.7 -1.0 0.5
$P_1(3/2)$, ⊥		165.7	2 2 2 2 2	0 -2 -2 2 2	3 3 3 3 3	1 -3 -1 1 3	-193 -155 -92 29 165	3.4 -8.0 6.0 5.4 17.7
$P_1(3/2)$, ||		276.2	2 2 1 1	-2 0 0 1	3 3 1 2	-2 0 0 1	-82 48 -37 134	6.6 17.4 -4.0 -12.1
Std. dev. =8.1 MHz								

[a] Observed Stark shift relative to the field-free line.

[b] Difference between the observed and calculated Stark shift.

Table 0.17 The observed and calculated Stark shifts of lines in AuS

Branch, pol.	Field (V/cm)	F'	M_F'	F''	M_F''	Obs[a] (MHz)	Dif[b] (MHz)	Branch, pol.	Field (V/cm)	F'	M_F'	F''	M_F''	Obs[a] (MHz)	Dif[b] (MHz)
$^QP_{21}(5/2)$, ⊥	376.3	3	3	4	4	-200	-21	$^QP_{21}(5/2)$, ||	276.2	2	2	3	-2	-75	-6
		3	2	4	3	-144	-25			2	0	3	0	-12	11
		3	0	4	1	-73	-7			2	2	3	2	21	-9
		3	1	4	0	2	-4			2	0	3	0	85	-6
		3	1	4	2	79	-3		276.2	2	2	3	-2	-70	11
		3	3	4	4	171	-10			2	0	3	0	-7	-10
	552.5	3	3	4	4	-236	26			2	2	3	2	35	6
		3	2	4	3	-164	6			2	0	3	0	94	-1
		3	0	4	1	-69	12		331.5	3	3	4	3	-110	16
		3	1	4	0	24	2			3	2	4	2	-44	3
		3	1	4	2	114	-19			3	0	4	0	0	15

		3	3	4	4	228	-37			3	3	-3	4	-3	84	-5
						-			331						-	
		3	3	4	4	247	15		.5	3	3	4	3	110	9
						-										
		3	2	4	3	173	-2			3	2	4	2	-45	-1
		3	0	4	1	-73	9			3	0	4	0	-5	11
											-					
		3	1	4	0	19	-3			3	3	4	-3	70	-5
									552					-		
		3	1	4	2	110	-23		.5	3	3	4	3	185	-15
		3	3	4	4	242	-24			3	2	4	2	-84	-6
R_1(3/2	220					-										
), ||	.9	4	3	3	3	156	0			3	0	4	0	16	-6
											-					
		4	2	3	2	-85	-28			3	3	4	-3	131	-7
									552					-		
		4	0	3	0	21	24		.5	3	3	4	3	191	-21
			-													
		4	2	3	-2	141	2			3	2	4	2	-90	-10
	220					-										
	.9	4	3	3	3	154	-6			3	0	4	0	10	-12
											-					
		4	2	3	2	-82	-25			3	3	4	-3	135	-4
									552					-		
		4	0	3	0	20	22		.5	3	3	4	3	191	-20
			-													
		4	2	3	-2	146	6			3	2	4	2	-91	-13
	276					-										
	.2	4	3	3	3	196	-11			3	0	4	0	10	-12
											-				-	
		4	2	3	2	-98	-29			3	3	4	-3	132	7	
		4	0	3	0	26	15									
			-													
		4	2	3	-2	187	10									
	276					-										
	.2	4	3	3	3	190	-6									
		4	2	3	2	-90	-20									
		4	0	3	0	24	12									
			-													
		4	2	3	-2	177	0									

Std. dev. =8.6 MHz

[a] Observed Stark shift relative to the field-free line. [b] Difference between the observed and calculated Stark shift.

5.3.2 Analysis

Since no Stark shifts were observed for the $B^2\Sigma^-$ (v=0) states of AuO and AuS at the relatively low applied electric fields, only the Stark effect of the $X^2\Pi_{3/2}$ (v=0) states needed to be considered and analyzed. The fine and hyperfine parameters for the $X^2\Pi_{3/2}$ (v=0) of AuS has been determined in the previous chapter, and those for the ground state of AuO were measured precisely by the pure rotational studies [68]. Those parameters are used for modelling the energies and wavefunctions of the $X^2\Pi_{3/2}$ (v=0) states.

The interaction with the static electric field was modeled using the conventional Stark Hamiltonian [20]:

$$\mathbf{H}^{stark} = -\vec{\mu}_{el} \cdot \vec{E}\,, \tag{5.9}$$

where $\vec{E}$ is the external electric field, and $\vec{\mu}_{el}$ is the electric dipole moment operator. A 128×128 matrix was generated for the $X^2\Pi_{3/2}$ (v=0) state to represent the F=0-7 Hund's case $a_{\beta J}$, non-parity, basis set: ψ(case $a_{\beta J}$) = $\left|\mathrm{n}\Lambda; S\Sigma; (\mathrm{JI})\Omega \mathrm{FM}_F\right\rangle$. The matrix was numerical diagonalized to produce eigenvalues and eigenvectors and the Stark shift energies was obtained. A non-linear least squares fitting was preformed using the observed Stark shifts in Table 5.5 to determine μ_{el} values of 2.94 ± 0.06 D and 2.22 ± 0.05 D for the $X^2\Pi_{3/2}$ (v=0) states of AuO and AuS, respectively. The standard deviation of the AuO and AuS fits are 8.1 MHz and 8.6 MHz, which are much less than the estimated uncertainty (20 MHz). The standard deviation statistical errors (± 0.06 D and ± 0.05D) of the determined μ_{el} values are comparable to the estimated 2% possible systematic error.

5.3.3 Discussion

The experimentally determined μ_{el} values for $X^2\Pi_{3/2}$ (v=0) states of AuO and AuS are listed in Table 5.7 comparing with the selected predicted values from various reference [74, 75] and the most recent prediction from our collaborator, Prof. Cheng [76]. The experimentally determined μ_{el} value of AuO (μ_{el}=2.94 ± 0.06 D) is slightly larger than that of AuS (μ_{el}=2.22± 0.05 D), which is consistent with the electronegativity of S being less than that of O. The prediction using The relativistic Hartree-Fock (HF) and configuration interaction (CI) method are in very poor agreement with the determined values by giving the μ_{el} values of 5.53 D and 4.69 D [74]. Later the predicted values of 3.39 D and 2.63 D for AuO and AuS obtained using the NESC/DFT method are both approximately 0.4 D higher possibly because of insufficient modelling of the nature of the valence 2π and 2σ orbitals [75]. The most recent work by Prof. Cheng was performed using various methods. The results given by lower level computation methods (i.e. HF-SCF) are larger than the experimental values by more than 50%. The higher-level prediction with considering of electron correlation contributions and zero-point vibrational corrections greatly improved the results, i.e. CCSD(T). The best computational values presented here, 3.12 D for AuO and 2.44 D for AuS, agree reasonably well with the experimental results (2.94 D for AuO and 2.22 D for AuS).

	Exp.	Previous Prediction		Prof. Cheng's Prediction				
Theo.		HF-CL	NESC/DFT	HF-SCF[a,b]	CCSD(T)[a,b]	+TQ[a,c]	+SO[d]	+vib[a,c]

AuO	2.94(6)	5.53	3.39	4.46	3.21	3.20	3.12	3.12
AuS	2.22(5)	4.69	2.63	4.14	2.44	2.44	2.37	2.37

Table 0.18 Calculated $|\vec{\mu}_{el}|$ for AuO and AuS (in Debye).

[a] SFX2C-1e. [b] unc-ANO-RCC basis sets. [c] ANO1 basis sets. [d] Dyall's double-zeta basis.

5.4 Summary

In this chapter, the high-resolution field-free spectra for the $B^2\Sigma^- – X^2\Pi_{3/2}$ (0, 0) band of AuS have been recorded and analyzed to precisely determine fine and hyperfine molecular parameters for the $X^2\Pi_{3/2}$ (v=0) and $B^2\Sigma$ (v=0) states. Optical Zeeman spectroscopic study was performed to determine the magnetic dipole moments for the $X^2\Pi_{3/2}$ (v=0) and $B^2\Sigma^-$ (v=0) states of AuS.

The ground state permanent electric dipole moments, $\vec{\mu}_{el}$, for the two most fundamental gold-containing molecules, AuO and AuS, have been experimentally determined and theoretically predicted. A quantum-chemical calculation using the new developed SFX2C-1e scheme predicted $\vec{\mu}_{el}$ values (3.12 D for AuO and 2.44 D for AuS) agrees well with the experimental values (2.94 ± 0.06 D for AuO and 2.44 ± 0.05 D for AuS). In contrast to the SFX2C-1e scheme, non-relativistic methodologies perform poorly. Somewhat surprising is the observation of the large reduction in $\vec{\mu}_{el}$ due to the inclusion of higher order electron-correlation (see Table 5.7). An important conclusion is that developing methods treat electron correlation is more important that methods to treat relativistic effect in diatomic Au-containing molecules.

6. OTHER STUDIES

6.1 Introduction

The systematic spectroscopic studies of diatomic gold-containing molecules, i.e. AuF, AuCl, AuS, and AuO, have been described in the previous chapters. In addition to those works, I have been involved, and made contributions, to other projects. These projects are highly related with the topic of my thesis (metal bonding). Therefore, I will briefly describe these works in this chapter. There are two subjects:

1) The optical spectroscopic studies of PtC and PtF [77, 78],
2) The optical Zeeman and Stark spectroscopy of MgH and MgD [79, 80].

Pt (Z=78) sits right next to Au (Z=79) on the periodic table with an electron configuration of [Xe][$4f^{14}$]$5d^{9}6s^{1}$. As shown in Figure 1.2, Pt has a similar strong 6*s* orbital contraction as Au due to relativistic effects. Therefore, the chemical properties performed by Pt are very like those of Au. With gaining an electron, the Pt ion (Pt^{-}) will have the same electronic structure as Au. The platinide anion Pt_2^{2-} has been found and considered to as the first member of the continuous series with Au_2 and Hg_2^{2+} [81]. Not just the ions, but Pt also has unusual higher oxidation states (Pt^{2+}, Pt^{4+}, and Pt^{6+}) which is very similar to Au. All the common "personalities" between Pt and Au make the Pt chemistry equally interesting and important in studying and modelling the relativistic effect. The current studies of PtF and PtC examine proto-typical ionic and covalent bonding.

The spectra of magnesium hydride, MgH, and magnesium deuteride, MgD are routinely used for the characterization of effective temperature, gravities, and isotopic abundance of the stars [82-84]. Especially the $A^2\Pi_r$–$X^2\Sigma^+$ band, which are Zeeman active

and in the 515 nm visible range, has applications on the investigation of solar and stellar magnetism [80]. For example, this band has been used in the detection and analysis of the Zeeman split Stokes V spectra in spatially resolved sunspots with a probed magnetic field at around a few kG [85-87]. In addition being a light polar ($\vec{\mu}_{el}$ >> 0D), paramagnetic ($\vec{\mu}_{m}$ >> 0 JT^{-1}) neutral molecules, MgH and MgD have attractive properties for kinetic energy manipulation to produce ultra-cold molecules. MgH is a candidate slowing and trapping experiment vaia the interaction of $\vec{\mu}_{el}$ with a static electric field (i.e. the Stark effect) or $\vec{\mu}_{m}$ with a static magnetic field (i.e. the Zeeman effect) to generate cold and ultra-cold molecular samples [88-90]. Therefore, these two important properties electric dipole moment, $\vec{\mu}_{el}$, and magnetic dipole moment, $\vec{\mu}_{m}$, will be investigated and discussed in this chapter.

6.2 The spectroscopic studies of PtC and PtF

The spectroscopic studies of a serious of Pt-containing molecules have been previously investigated by my former lab-mates, including PtC, PtN, PtO, PtF, etc. [77, 78, 91-94]. Here I will introduce our most recent studies on PtF and PtC. The pure rotational spectrum of PtC has been recorded using pump/probe microwave optical double resonance technique and analyzed to determine the fine and hyperfine parameters for the $X^1\Sigma^+$ (v=0) state. Also presented here are the experimental determination of $\vec{\mu}_{el}$ and the ^{19}F(I=1/2) and ^{195}Pt(I=1/2) magnetic hyperfine interactions for PtF in the [11.9]Ω =3/2 (v= 0 and 1) and $X^2\Pi_{3/2}$ (v = 0) states.

6.2.1 Pure rotational spectrum of PtC

A block diagram of the pump/probe microwave optical double resonance set-up is given in Figure 6.1. Molecular beam pump/probe microwave optical double resonance (PPMODR) [95, 96] was used to record the pure-rotational spectrum of the $^{194}Pt^{12}C$, $^{195}Pt^{12}C$, and $^{196}Pt^{12}C$ isotopologues. Radiation from a continuous wave dye laser was used to excite lines in the $A^1\Pi$–$X^1\Sigma^+$ (0, 0) band near 540 nm. The resulting LIF signal was viewed through a 570 ± 10 nm band pass filter and detected with a cooled photo-multiplier tube. Photon-counting techniques were used to process the signal. An intense (~200 mW) laser pump beam was used to deplete the population in either the J''=1 or J''=2 levels of the $X^1\Sigma^+$ (v = 0) state. Tunable microwave radiation repopulated the depleted level. The repopulation detected as an increase in the LIF signal induced using a weak (~10 mW) probe laser beam operating at the same wavelength as the pump beam. The tunable microwave radiation was generated by the second or fourth harmonic of nominally 15.86 GHz radiation from a frequency synthesizer. A rubidium frequency standard was used to generate the time-base for the frequency synthesizer. The stabilized microwave radiation was introduced into the chamber via a homemade 26˚ 'H-plane' horn antenna (approximately 3 × 0.4 cm).

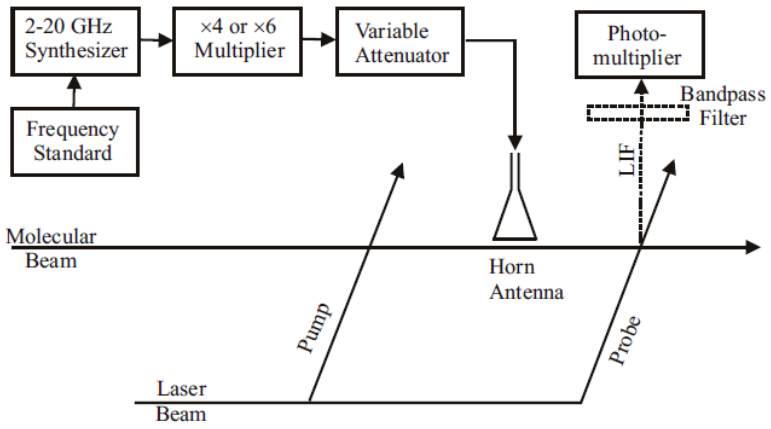

Figure 0.31 A schematic diagram of the PPMODR experimental.

Two pure rotational transitions were measured for $^{194}Pt^{12}C$, $^{195}Pt^{12}C$ and $^{196}Pt^{12}C$:

1) $R(1)$ line for the $J=0\rightarrow J=1$ pure rotational measurements

2) $R(2)$ and $Q(2)$ lines for the $J=1\rightarrow J=2$ pure rotational measurements

The optical transition frequency of these lines were taken from the previous study [92]. A portion of the LIF spectrum in the region of the $R(2)$ transition over the three isotopologues is presented in Figure 6.2. The associated energy levels of the $^{195}Pt^{12}C$ isotopologues are demonstrated on the right portion. The two widely spaced features (a and b) of the $^{195}Pt^{12}C$ transition are due to the large magnetic hyperfine splitting in the $A^1\Pi(v=0)$ state. The $J=1\rightarrow J=2$ pure rotational spectrum of $^{194}Pt^{12}C$ obtained by pumping the $R(2)$ (ν=18512.8289 cm^{-1}) transitions is presented in Figure 6.3. The measured frequencies, associated quantum number assignments, and the difference between the observed and calculated frequencies are presented in Table 6.1.

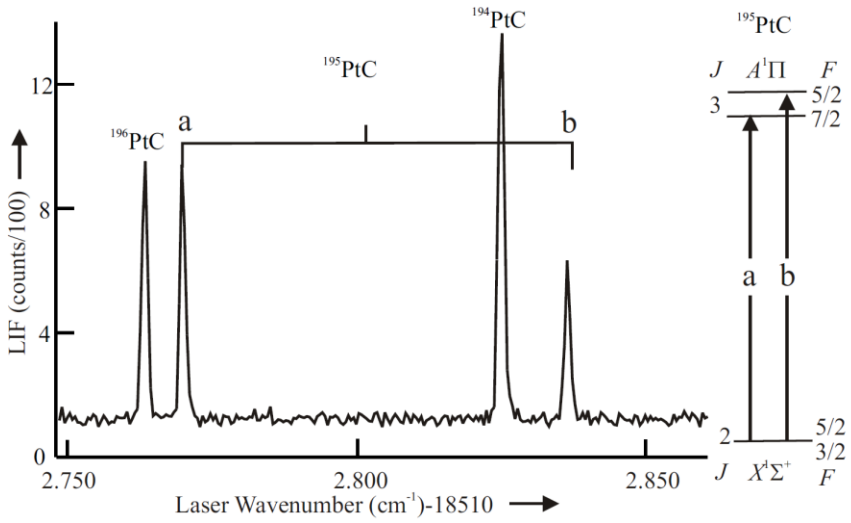

Figure 0.32 The LIF spectrum of the $A^1\Pi \leftarrow X^1\Sigma^+$ (0, 0) in the region of the $R(2)$ branch feature and associated energy levels for the ^{195}PtC isotopologue. The $R(2)$ branch for ^{195}PtC is split due to the orbital magnetic hyperfine splitting in the $A^1\Pi(v=0)$ state. The nuclear spin hyperfine splitting is not resolved in the LIF spectrum and not indicated in the energy level diagram.

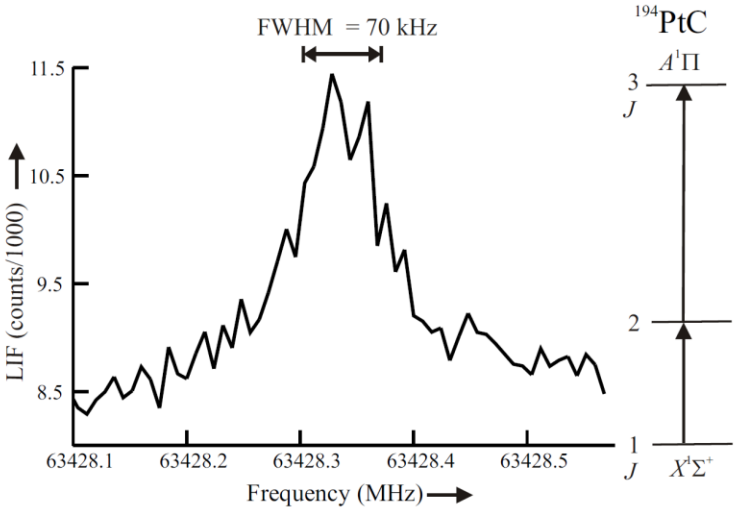

Figure 0.33 The J=2 ← J=1 rotational transition for the ^{194}PtC isotopologue obtained by pumping and probing the R(2) transitions (ν=18512.8289 cm^{-1}) of the $A\,^1\Pi \leftarrow X\,^1\Sigma^+$ (0,0) band near 540 nm.

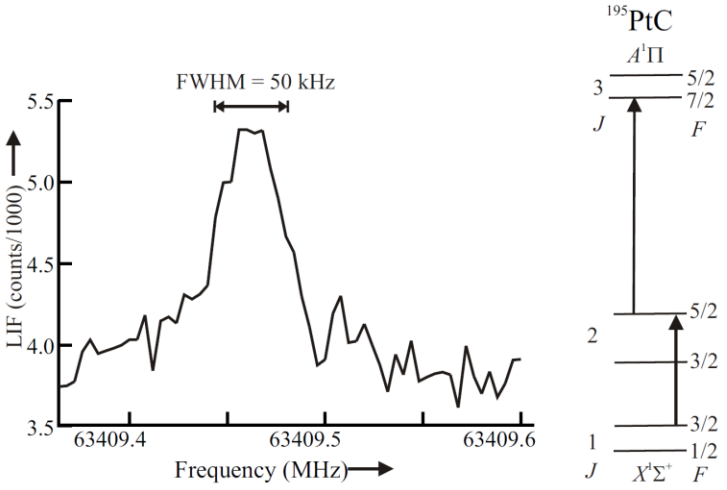

Figure 0.34 The J=2, F =5/2← J=1, F=3/2 rotational transition for the ^{195}PtC isotopologue obtained by pumping and probing the J=3, F=7/2← J=2, F=3/2,5/2 component of the R(2) transitions (ν=18512.7784 cm^{-1}) of the $A\,^1\Pi \leftarrow X\,^1\Sigma^+$ (0,0) band near 540 nm.

Table 0.19 Observed and calculated frequencies for the $X\,^1\Sigma^+$(v=0) pure rotational transitions[a].

	^{194}PtC[b]		^{195}PtC			^{196}PtC[b]	
	Observed	Dif.[c]	$F'\leftarrow F''$	Observed	Dif.[c]	Observed	Dif.[c]
J=1←J=0	31714.374	0.006	1/2←1/2	31704.740	-0.001	31695.504	-0.001
			3/2←1/2	31704.950	0.001		
J=2←J=1	63428.340	-0.003	3/2←3/2	63409.120	0.005	63390.617	0.001
			3/2←1/2	63409.312	-0.010		
			5/2←3/2	63409.466	0.006		
	Std. dev.= 0.006MHz			Std. dev.= 0.009MHz		Std. dev.= 0.001 MHz	

[a] All units are MHz.
[b] D constrained to optical value of 0.0164 MHz [97].
[c] Dif.=Obs.-Calc. obtained using optimized parameters.

Table 0.20 Spectroscopic parameters (in MHz) for the $X\,^1\Sigma^+$(v=0) state

	^{194}PtC		^{195}PtC		^{196}PtC	
	PPMODR[a]	Opt.[b]	PPMODR	Opt.	PPMODR	Opt.
B	15857.217(4)	15857(1)	15852.430(10)	15851(1)	15847.786(1)	15847
D	0.0164	0.0164	0.0124(16)	0.0164	0.0164[c]	0.0164
C_I^{eff}			0.138(12)			

[a] This work.
[b] Ref. [93].

The energies of the X $^1\Sigma^+$ state were modeled using the simple expression[20]:

$$E = BJ(J+1) - D[J(J+1)]^2 + \frac{C_I^{eff}}{2}\left[F(F+1) - J(J+1) - I(I+1)\right], \qquad (6.1)$$

where B is the rotational parameters, D is the centrifugal distrotion constant, and the last term was for the hyperfine interaction, which was omitted for ^{194}PtC and ^{196}PtC. The

determined spectroscopic parameters, along with those of the previous molecular beam study [93], are given in Table 6.2.

The rotational parameters, *B*, determined here are consistent with the previous values [93], but are approximately a factor of 100 more precise. For isotopologues with different mass, the ratio of the rotational parameters are in good agreement with the ratio of the reduced masses, $\rho(\equiv\mu/\mu^*)$. The determined ratios of rotational constant for B^{195}/B^{194}, B^{196}/B^{194} and B^{196}/B^{195} are 0.9996981, 0.9994052, and 0.9997070, whereas the ratio of reduced mass for ρ(194/195), ρ(194/196), and ρ(195/196) are 0.9997005, 0.9994047, and 0.9997041, respectively.

C_I^{eff} is the nuclear spin-molecular rotation coupling parameter. This interaction is unusually not detected using optical spectroscopy. The relatively large value of C_I^{eff} (=138(2) MHz) was rationalized using perturbation theory.

6.2.2 Optical Study of hyperfine interaction and Stark measurement of PtF

High resolution spectra of the [11.9] Ω=3/2 ← $X\,^2\Pi_{3/2}$(0, 0) and (1, 0) bands of PtF were recorded field-free in the region from 11932.6 to 11938.3 cm^{-1} and 12494.8 to 12489.6 cm^{-1}. The observed and predicted spectra for the *P*(9/2) (ν=11933.4 cm^{-1}) branch feature of the (0, 0) band are presented in Figure 6.5. Platinum has six naturally occurring isotopes: ^{190}Pt, 0.01%; ^{192}Pt, 0.79%; ^{194}Pt, 32.9%; ^{195}Pt, 33.8%; ^{196}Pt, 25.3%, ^{198}Pt, 7.23%. Spectral features for the four most abundant isotopologues of PtF are observed and identified in Figure 6.5. The observed and predicted spectra of the *R*(5/2) (ν =12494.25 cm^{-1}) branch feature for the^{195}PtF isotopologues in the (1, 0) band are presented in Figure 6.6, along with the associated energy level diagram and quantum number assignments. The

corresponding transitions for the ^{196}PtF and ^{194}PtF are at 12494.13 cm^{-1} and 12494.36 cm^{-1}, respectively. A total of precisely measured 289 field-free transition frequencies along with assignments is listed in Appendix B.

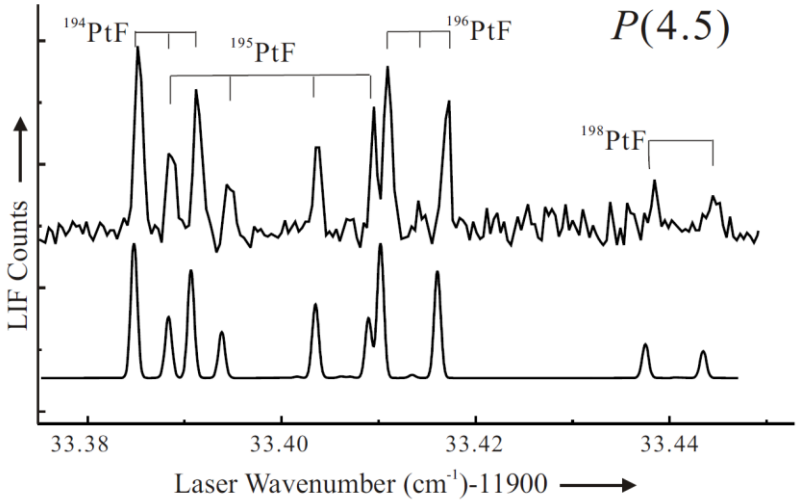

Figure 0.35 The observed (upper) and predicted (lower) spectra for the *P*(9/2) (ν=11933.4 cm^{-1}) branch feature of the (0, 0) [11.9] Ω=3/2 ← $X^2\Pi_{3/2}$ band of PtF. The splitting is due to the ^{195}Pt(I=1/2) and ^{19}F(I=1/2) magnetic hyperfine interaction.

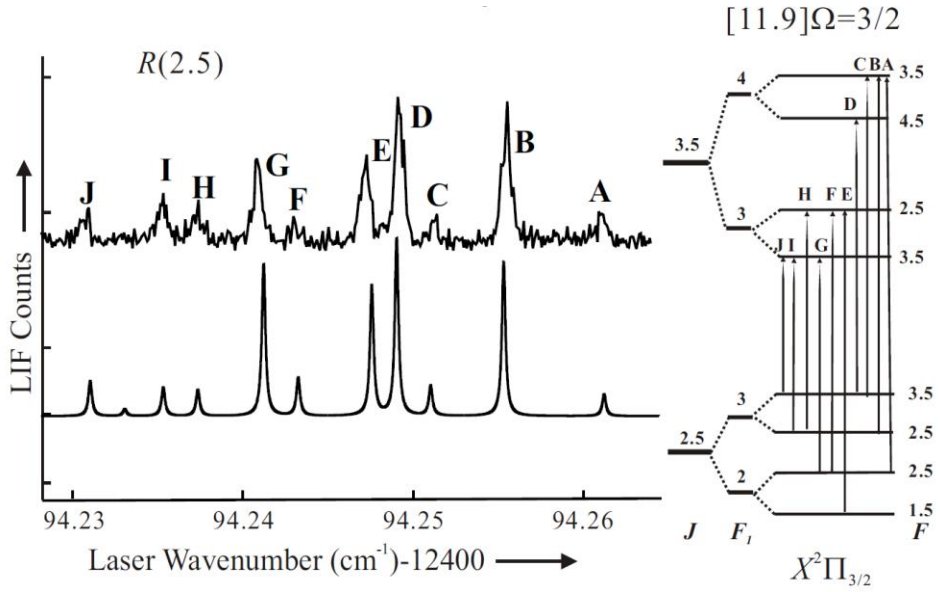

Figure 0.36 The observed (upper) and predicted (lower) spectra for the *R*(2.5) (ν=11933.4 cm^{-1}) branch feature of the for the Ω=3/2 ← $X\,^2\Pi_{3/2}$ (1,0) band of ^{195}PtF. The splitting is due to the ^{195}Pt(I=1/2) and ^{19}F(I=1/2) magnetic hyperfine interaction.

The isolated *R*(1.5) (ν =12493.7219 cm^{-1}) features of ^{194}PtF in the [11.9]Ω=3/2← $X^2\Pi_{3/2}$ (1,0) band were selected for optical Stark measurements. The spectra of the *R*(1.5) line recorded field-free and in the presence of a 187.9 V/cm field are presented in Figure 6.7 along with the predicted Stark spectrum using optimized parameters. The Stark tuning of the associated energy levels as a function of applied electric field is given on the right portion of Figure 6.7 with the spectral features assignments. The applied static electric field was oriented parallel to the linearly polarized laser radiation, resulting in ΔM_F=0 selection rules. The measured Stark shifts relative to the field-free feature and quantum number assignments are presented in Table 6.3.

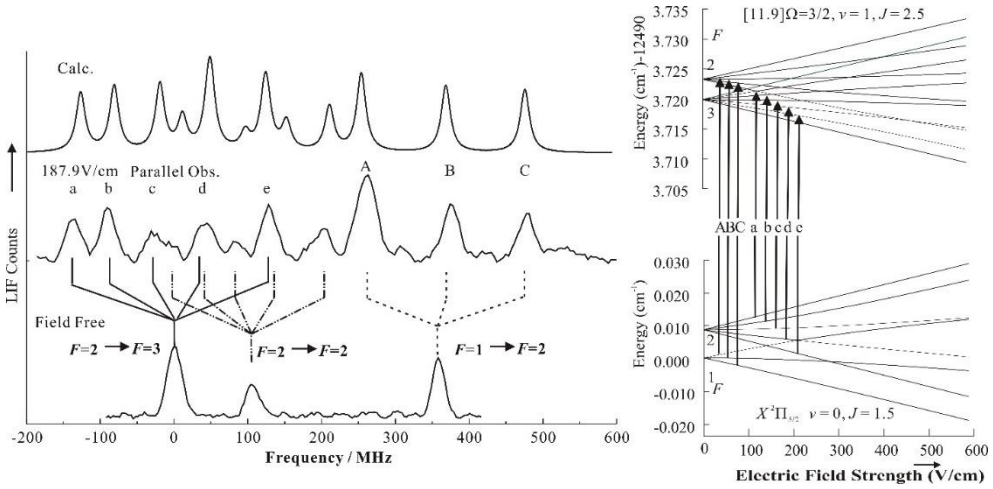

Figure 0.37 The observed field-free, Stark and predicted Stark spectra for the $R(1.5)$(v =12493.7219 cm^{-1}) features of the (1,0) [11.9] Ω=3/2 ← $X\,^2\Pi_{3/2}$ band of ^{194}PtF. The Stark tuning of the energy levels associated with the $R(1.5)$(v =12493.7219 cm^{-1}) features of the (1,0) [11.9] Ω=3/2 ← $X\,^2\Pi_{3/2}$ band of ^{194}PtF was given on the right along with the assignment.

Table 0.21 Observed and calculated Stark shifts for $R(1.5)$ branch of (1, 0) [11.9] Ω=3/2 ← $X^2\Pi_{3/2}$ band system of ^{194}PtF.

Polarized branch $F'\leftarrow F''$	$M'_F \leftarrow M''_F$	Field (V/cm)	Obs. (MHZ)	Dif. (MHz)
3←2 ‖	2←2	106.6	-68	4
	1←1		-42	0
	0←0		-10	-3
	1←1		34	2
	2←2		65	-6
	2←2	187.9	-134	-5
	1←1		-87	-4
	0←0		-19	0
	1←1		45	-5
	2←2		131	6
2←2 ‖	2←2	187.9	-106	6
	1←1		-60	7
	0←0		-20	3

	1←1		26	-7
	2←2		101	8
2←1 ‖	1←1	106.6	-50	9
	0←0		15	8
	1←1		74	3
2←1 ‖	1←1	187.9	-92	3
	0←0		22	1
	1←1		124	-5
3←1 ‖	1←1	187.9	-94	-6
3←2 ⊥	1←2	187.9	-162	1
	0←1		-120	-3
	3←2		-93	0
	-1←0		-54	-1
	2←1		-47	1
	2←1		19	1
	1←0		19	8
	3←2		90	-4
	1←2		156	-1
2←2 ⊥	-1←-2	187.9	-142	2
	0←1		-101	8
	1←0		-46	13
	0←-1		-14	12
	-2←-1		1	4
	-1←0		40	6
	0←1		87	-4
	1←2		161	10
2←1 ⊥	0←1	187.9	-141	0
	2←1		-58	-8
	1←0		-29	-3
	1←0		69	3
	2←1		78	-3
Std. dev. = 6 MHz				

Modeling the energy levels for both the [11.9]Ω=3/2 and $X^2\Pi_{3/2}$ states of PtF was treated as $^2\Pi_{3/2}$ states, which is very similar to that of the $X^2\Pi_{3/2}$ of AuO and AuS. The effective Hamiltonian was written by including the origin ($T_{v'v''}$), a rotational (B), and ^{195}Pt (I=1/2) and ^{19}F (I=1/2) magnetic hyperfine terms as:

$$\hat{H}^{eff} = T_{v'v''} + \hat{H}^{rot} + \hat{H}^{mhf}(Pt) + \hat{H}^{mhf}(F).$$

(6.6)

The description of each term in this Hamiltonian has been described in detail in the analysis of AuO and AuS (see Chapter 5.2). The field-free eigenvalues and eigenvectors were obtained by numerical diagonalization of a 4×4 or 8×8 matrix representation of $\hat{H}^{eff}$. The 289 precisely measured optical transition wavenumbers were least-squares fit directly to obtained the optimized set of parameters and associated errors given in Table 6.4 for the [11.9] Ω = 3/2 and $X\,^2\Pi_{3/2}$ states of the ^{194}PtF, ^{195}PtF, ^{196}PtF, and ^{198}PtF isotopologues.

As drove for all other Stark analysis of this thesis, the behavior of the energy levels in the presence of the applied electric field was modeled by including the operator

$$\hat{H}^{Stark} = -\hat{\mu}_{el} \cdot \vec{E},$$

(6.7)

where $\hat{\mu}_{el}$ is the dipole moment operator and $\vec{E}$ is the applied static electric field vector. The Stark shifts of the $X^2\Pi_{3/2}$ and [11.9] Ω=3/2 states given in Table 6.3 were modeled with a 16×16 matrix representation and used as an input file into a non-linear least-squares fitting procedure. The standard deviation of the fit (= 6 MHz) is commensurate with measurement uncertainty in the Stark shifts. The optimized $\vec{\mu}_{el}$ values for the [11.9]Ω = 3/2 and $X\,^2\Pi_{3/2}$ states were determined to be 2.47±0.11 D and 3.42±0.06 D, respectively.

Table 0.22 The determined field-free spectroscopic parameters for the [11.9] Ω=3/2 (v=1), [11.9] Ω=3/2 (v=0) and X $^2\Pi_{3/2}$ (v=0) states of PtF (in wavenumbers, cm^{-1}).

State	^{194}PtF	^{195}PtF	^{196}PtF	^{198}PtF
$X^2\Pi_{3/2}$				
B[a]	0.277316757(8)[b]	0.277190249(2) [b]	0.277065260(5) [b]	0.276818798(1) [b]
$h_{3/2}$(Pt)		0.02385(42) 0.023219(63) [b]		
$h_{3/2}$(F)	0.01118(59) 0.010870(16) [b]	0.01088(46) 0.010877(29) [b]	0.01109(53) 0.010872(10) [b]	0.0111(15) 0.010860(30) [b]
[11.9](v=0)				
B	0.25808(3)	0.25796(2)	0.25785(2)	0.25759(6)
$h_{3/2}$(Pt)		0.05900(57)		
$h_{3/2}$ (F)	-0.00654(77)	-0.00642(55)	-0.00623(70)	-0.00688(148)
$T_{0,0}$ *-11930*	6.15041(37)	6.16093(25)	6.17330(33)	6.19829(66)
[11.9](v=1)				
B	0.25680(4)	0.25680(4)	0.25674(4)	
$h_{3/2}$ (Pt)		0.05881(56)		
$h_{3/2}$ (F)	-0.00598(85)	-0.00597(57)	-0.00652(75)	
$T_{1,0}$*-12490*	2.48144(41)	2.59467(31)	2.71202(38)	
Std.dev.	0.00074	0.00079	0.00068	0.00108

[a] B ($X^2\Pi_{3/2}$) and D($X^2\Pi_{3/2}$) constrained to those of given in Ref. 16. D([11.9](v=1and 1)) constrained to $X^2\Pi_{3/2}$ values.
[b] Ref. [98],

6.3 MgH and MgD

6.3.1 The optical Zeeman spectroscopy of MgH

The primary motivation for this study was to measure the magnetic tuning (i.e. Zeeman effect) of the optical features of MgH such that this spectra can be used to probe solar magnetic fields. Precise determination of the Zeeman effect requires a precise determination of the field-free energies. Accordingly, the field free spectra of numerous low-J branch features were recorded. The observed wavenumbers, difference between the observed and calculated wavenumbers and the quantum number assignments are given in

Table 6.5. The field free transition frequencies determined here are approximately a factor of 10 more precise than those of the previous study [99] and unlike the previous study include the lowest members of the branches. The energy level pattern for the $A^2\Pi_r$ state rapidly transform from a Hund's case (a) limit to that of a Hund's case (b) limit because the ratio of the spin-orbit parameter, *A*, to that rotational parameter, *B*, is only 3.6. The electronic spin rapidly decouples from the orbital angular momentum and recouples to rotational angular momentum. Consequently the spectral pattern for even the could molecular beam sample is not the normally recognized 12 branches of a $A^2\Pi_r$ (case(a))–$X^2\Sigma^+$ (case(b)) electronic transition. The observed and predicted field-free spectra in the region of the $Q_1(3/2)$ (ν=19275.93 cm−1) and ${}^{Q}R_{12}(1/2)$ (ν = 19275.97 cm−1) lines are presented in Figure 6.8. Three most abundant isotopes of the magnesium has been observed in the three isotopologues: ^{24}MgH, ^{25}MgH, and ^{26}MgH. The spectrum for the ^{25}MgH isotopologue is complex because of unresolved ^{25}Mg (I=5/2) magnetic hyperfine splitting.

The ${}^{S}R_{21}(0.5)$(ν =19318.47 cm^{-1}), $R_2(0.5)$(ν=19307.04 cm^{-1}), and ${}^{R}Q_{21}(1.5)$(ν=19307.00 cm^{-1}) branch features of the $A^2\Pi_{3/2}$-$X^2\Sigma^+$ (0,0) sub-band and the $Q_1(0.5)$(ν =19273.27 cm^{-1}) and $R_1(0.5)$(ν =19287.37 cm^{-1}) branch features of the (0,0) $A^2\Pi_{1/2}$-$X^2\Sigma^+$ sub-band were selected for the Zeeman measurements. The spectra for the $R_1(0.5)$ feature recorded field-free and in the presence of a 3080 G magnetic field oriented perpendicular ($\Delta M_J = \pm 1$) to the electric field of the laser radiation are presented in the left side of the Figure 6.9. The associated energy level pattern as a function of magnetic field strength and spectral assignments are also given of Figure 6.8. The approximately 155 MHz splitting in the field-free spectrum is due to the proton magnetic hyperfine splitting between

the F=0 and F=1 (F=total angular momentum) of the N=0, J=0.5 level of the (v=0) $X^2\Sigma^+$ state. The Λ doubling in the J=1.5 level of the $A^2\Pi_{3/2}$ state is approximately 2 GHz. The electronic spin projection $M_S(=\pm\frac{1}{2})$ becomes approximately good quantum number upon application of only a modest magnetic field because the electronic spin is not strongly coupled to the molecular axis for the N=0, J=0.5 (v=0) $X^2\Sigma^+$ rotational level. Similarly, the nuclear spin is decoupled from the molecular axis at very small field strengths and the level patterns consist of nearly degenerate pairs that differ in nuclear spin projection quantum number, $M_I(=\pm\frac{1}{2})$. The hyperfine interaction is negligible in the $A^2\Pi_i$ state and J is the appropriate total angular momentum quantum number in the absence of the magnetic field.

The ${}^SR_{21}(0.5)$ feature recorded field-free and in the presence of a 3080 G magnetic field oriented parallel ($\Delta M_J = 0$) to the electric field of the laser radiation is presented in left-hand side of Figure 6.10. The associated energy level pattern as a function of magnetic field and spectral assignment are also given in Figure 6.10. The lower energy level for the ${}^SR_{21}(0.5)$ transition is identical to that of the $R_1(0.5)$ feature previously described. The J=1.5, $A^2\Pi_{3/2}$ levels rapidly tune upon the application of magnetic field. As before, the predicted spectrum indicated with the solid line was generated with optimized parameters g_L', g_l, and g_l.

The analysis of the field-free and Zeeman spectra for the $A^2\Pi_i - X^2\Sigma^+$ (0, 0) band of MgH was almost the same as that for the $B^2\Sigma^- - X^2\Pi_{3/2}$ (0, 0) band of AuS but with switching the order of the upper and lower states. Therefore, I will not repeat it again here. The determined field-free parameters for the $X^2\Sigma^+$ and $A^2\Pi_r$ states of MgH are given in Table

6.6 along with the previous studies [84]. The determined Zeeman parameters for the $X\ ^2\Sigma^+$ (v=0) and $A^2\Pi$ (v =0) states of MgH are presented in Table 6.7.

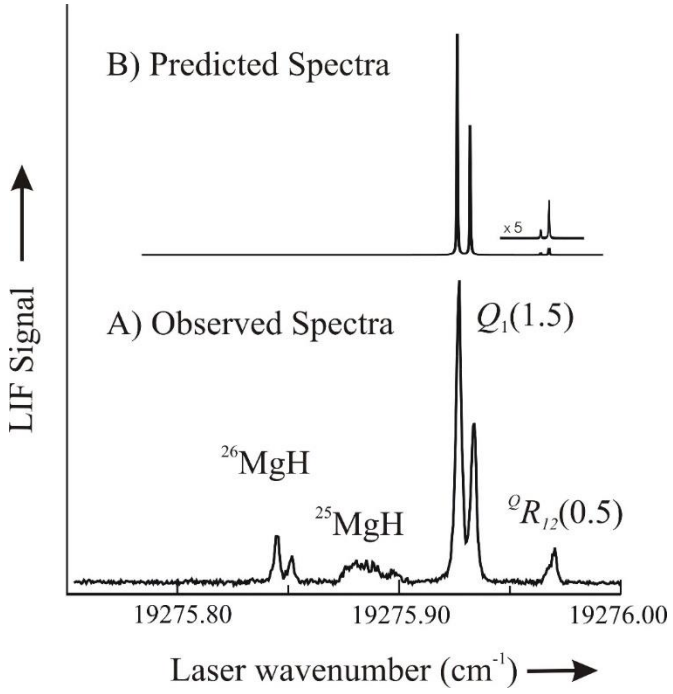

Figure 0.38 The observed Q_1 (3/2)(v =19261.9366 cm^{-1}) and $^{Q}R_{12}$ (1/2) (v =19261.9572 cm^{-1}) field-free spectrum.

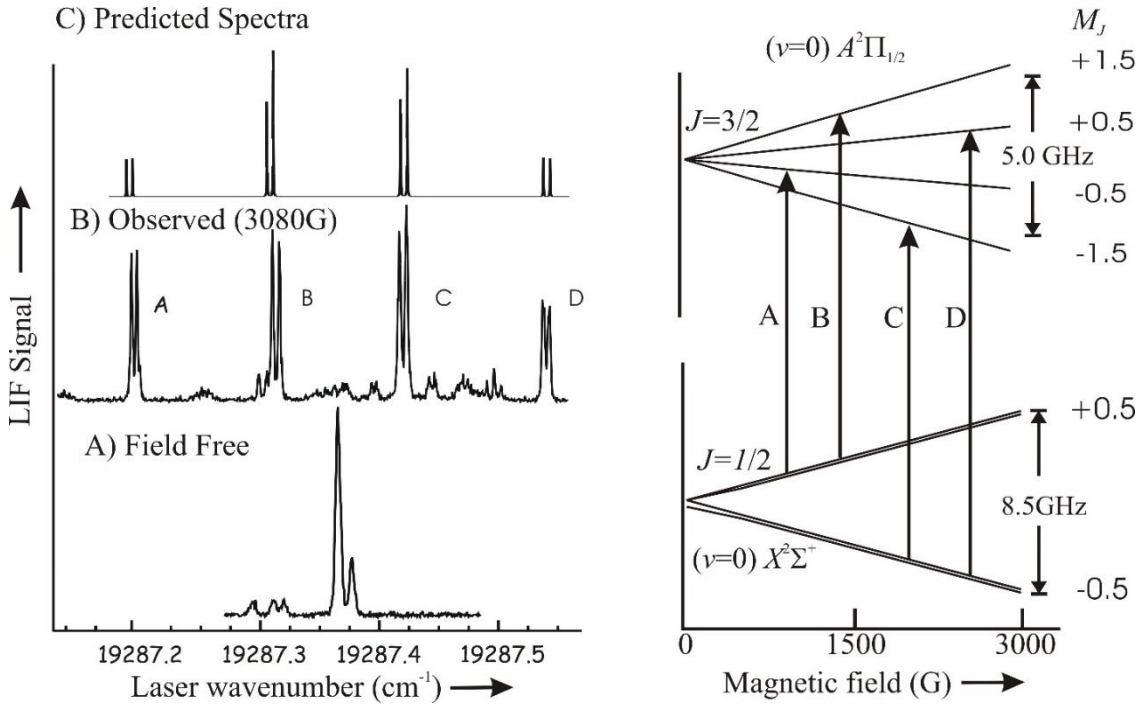

Figure 0.39 The Observed and predicted spectra of the $R_1(0.5)$ feature recorded field-free and in the presence of a 3080 G magnetic field oriented perpendicular ($\Delta M_J = \pm 1$) to the electric field of the laser radiation and the associated energy level pattern as a function of magnetic field.

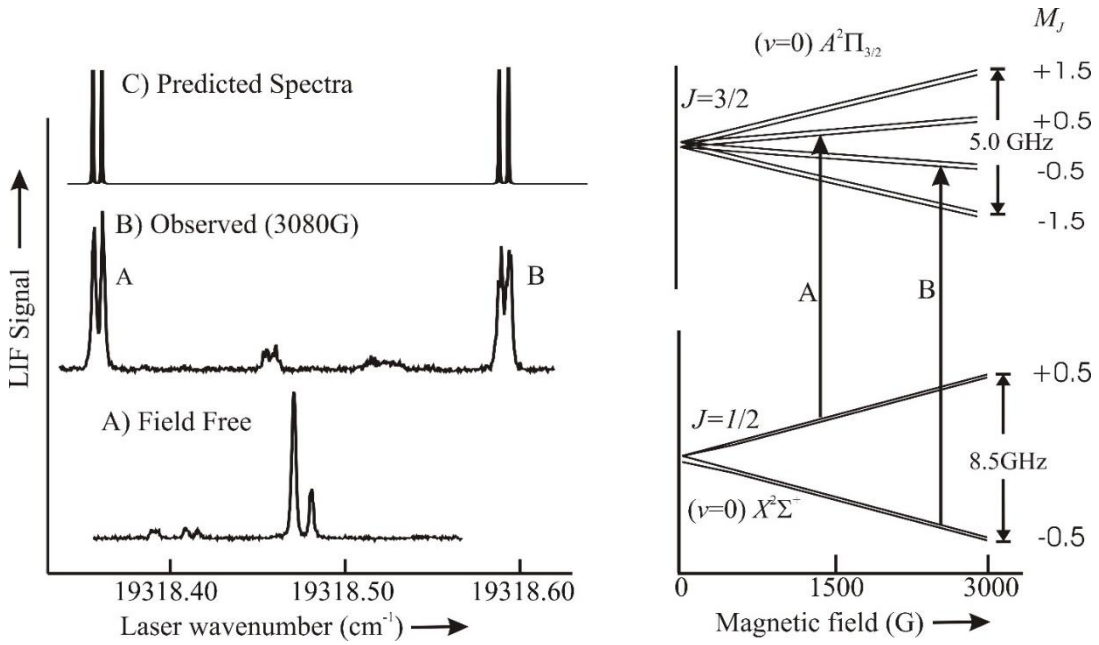

Figure 0.40 The Observed and predicted spectra of the ${}^{S}R_{21}(0.5)$ feature recorded field-free and in the presence of a 3080 G magnetic field oriented parallel ($\Delta M_J = 0$) to the electric field of the laser radiation and the associated energy level pattern as a function of magnetic field.

Table 0.23 The observed and calculated transition wavenumber (cm^{-1})for the $A\ ^2\Pi$- $X^2\Sigma^+$ (0, 0) band system of MgH .

$A\ ^2\Pi_{3/2}$ - $X^2\Sigma^+$				
Branch	J''	F''	Observed[a]	Obs.-calc.
${}^{S}R_{21}$	0.5	1	19318.4736	0.0039
		0	318.4838	0.0038
	1.5	2	342.5495	0.0030
		1	342.5556	0.0029
	2.5	3	367.7184	-0.0006
		2	367.7222	-0.0025
Q_2	1.5	2	284.1023	-0.0007
		1	284.1077	0.0002
	2.5	3	285.2908	-0.0061
		2	285.2976	-0.0039

	3.5	4	287.6270	-0.0019
		3	287.6397	0.0061
$^{R}Q_{21}$	1.5	2	306.9987	-0.0014
		1	307.0049	-0.0014
	2.5	3	319.6365	0.0023
		2	319.6409	0.0010
	3.5	4	333.3735	-0.0061
		3	333.3847	-0.0005
R_2	0.5	1	307.0385	-0.0015
		0	307.0427	-0.0010
	1.5	2	319.7010	0.0009
		1	319.7061	0.0016
	2.5	3	333.4716	-0.0001
		2	333.4782	0.0018
	3.5	4	348.1271	-0.0009
		3	348.1337	0.0009
P_2	2.5	2	284.0410	-0.0018
	3.5	4	239.5433	-0.0008
		3	239.5479	-0.0009
	4.5	5	230.5100	0.0022
		4	230.5155	0.0015
Std. Dev. = 0.0026 cm^{-1}				
A $^2\Pi_{1/2}$ - $X^2\Sigma^+$				
Branch	J''	F''	Observed[a]	Obs.-calc.
Q_1	0.5	1	19273.2679	-0.0006
		0	273.2793	0.0006
	1.5	2	275.9272	-0.0005
		1	275.9333	-0.0006
	2.5	3	278.3049	-0.0007
		2	278.3128	0.0015
$^{Q}R_{12}$	0.5	1	275.9675	0.0002
		0	275.9703	-0.0010
	1.5	2	278.3725	0.0010
		1	278.3748	-0.0012
R_1	0.5	1	287.3637	-0.0019
		0	287.3759	0.0000
	1.5	2	301.1958	-0.0015
		1	301.2043	0.0009
	2.5	3	315.3159	-0.0001
		2	315.3218	0.0001
P_1	1.5	2	261.7550	-0.0012
		1	261.7595	0.0007
	2.5	3	252.9340	0.0011
		2	252.9413	0.0026

$^{P}Q_{12}$	0.5	1	261.7971	-0.0008
		0	261.7974	-0.0005
	1.5	2	253.0000	0.0011
		1	253.0040	0.0007
$^{O}P_{12}$	1.5	2	238.9024	0.0007
		1	238.9078	0.0016
Std. Dev. = 0.0010 cm^{-1}				

[a] The total angular momentum for the $A\ ^2\Pi$ state, F', value is obtained from the $\Delta F = \Delta J$ relationship.

Table 0.24 The field-free parameters for the $X\ ^2\Sigma^+$ and $A^2\Pi$ states of MgH.

(v =0) $X\ ^2\Sigma^+$		(v =0) $A\ ^2\Pi_{3/2}$		(v =0) $A\ ^2\Pi_{1/2}$		(v =0) $A\ ^2\Pi$ (total)	
Par. [a]	Value[a]	Par.	Value	Par.	Value	Par.	Value
T_0	0.0	T_0	19278.5405(1)	T_0	19278.5451(1)	T_0	19278.5703(8)
B	5.7365	A	35.0581(2)	A	34.9474(1)	A	35.0158(2)
$D(\times 10^4)$	3.543	B	6.0962(3)	B	6.0930(2)	B	6.0934(7)
γ	0.0263	$D(\times 10^4)$	3.563	$D(\times 10^4)$	3.087(3)	$D(\times 10^4)$	2.833(1)
$\gamma_D(\times 10^6)$	-5.77	p	0.0843(7)	p	0.0259 (7)	p	0.0279(1)
b_F $(\times 10^2)$	1.027	q	-0.0025(2)	q	0.0017(2)	q	0.0013(6)
$c\ (\times 10^4)$	1.598						

[a] The fine structure parameters of the (v=0) $X\ ^2\Sigma^+$ state were held fixed to those of Ref. ….

Table 0.25 The determined Zeeman parameters for the $X\ ^2\Sigma^+$(v =0) and $A^2\Pi$ (v =0) states of MgH.

(v=0) $X\ ^2\Sigma^+$		(v=0) $A\ ^2\Pi$			
Parameter[a]	Value[b]	Parameter	Value[a]		
g_S	2.00227	g'_L	1.007(7)		
g_l	-0.0023	g_l	-0.18(6)		
		g'_l	-0.063(11)		
		g_S	2.002		
		Corr. Matrix[c]	1.00		
			-0.78	1.00	
			-0.33	-0.46	1.00

[a] The numbers in parentheses represent a 2σ error estimate. All values without error limits were held fixed.

[b] Taken from Ref. 19.

[c] Column labels given in order of the listed parameters.

6.3.2 Optical Stark spectroscopy of magnesium deuteride, MgD

The Stark effect in MgD is much larger than that of MgH because levels of opposite parity are closer together. The spectral features of the $A^2\Pi_r - X^2\Sigma^+$ (0, 0) band for MgD are nearly identical to the $A^2\Pi_r - X^2\Sigma^+$ (0, 0) band of MgH with difference with a shift of ~14 cm^{-1} on the transition positions caused by the isotopic effect between the H and D. Corresponding to the lines in the spectrum of MgH in Figure 6.7, the observed field-free spectrum in the region of the $Q_1(3/2)$(ν =19261.9366 cm^{-1}) and $^QR_{12}(1/2)$ (ν =19261.9572 cm^{-1}) lines of MgD is presented in Figure 6.11. Also presented is the sub-Doppler I_2 absorptions spectrum used for absolute wavelength calibration and the transmission of the stabilized etalon used for measurements of Stark induced shifts. In addition to ^{24}MgD, spectral features of the lesser abundant ^{25}MgD and ^{26}MgD, isotopologues are evident. The

complexity of the spectral features for the ^{25}MgD isotopologue is due to the unresolved ^{25}Mg(I=5/2) magnetic hyperfine splitting. The precisely measured transition wavenumbers of the low-rotational branch features of all twelve branches of the $A^2\Pi_r - X^2\Sigma^+$ (0,0) band of MgD are given in Table 6.8 along with the quantum number assignments and the difference between the observed and calculated wavenumbers.

For the Stark effect measurement, the spectra of the $R_1(1/2)$(v=19267.9157 cm^{-1}), $Q_1(1/2)$(v=19259.4133 cm^{-1}) and, $^{S}R_{21}(1/2)$ (v=19298.6093 cm^{-1}) branch features of ^{24}MgD were selected. Spectra for the $R_1(1/2)$ transition recorded in the presence of the of 3375 V/cm with both perpendicular and parallel polarizations are presented in Figure 6.12 along with the Stark tuning of the energy levels as a function of the applied electric field. The selection rules for the transitions in perpendicular polarization are $\Delta M_J = \pm 1$, whereas in parallel polarization are $\Delta M_J = 0$, respectively. A total of 48 shifts ranging from field strengths of 2250 to 10526 V/cm were accurately measured and are listed in Table 6.9 together with the quantum number assignments, and difference between the observed and calculated shifts.

A precise analysis of the Stark effect required the determination of the field-free energy levels of MgD, which is very similar to that of MgH. The optimized field-free parameters for the $A\ ^2\Pi$ (v=0) are given in Table 6.10 associated errors and correlation coefficients. The standard deviation of the fit was 0.0011 cm^{-1}, which is commensurate with the estimated measurement uncertainty of the transition wavenumbers. The determined values for $\left|\vec{\mu}_{el}\right|$ were 1.31±0.08 D and 2.567±0.010 D for the $X\ ^2\Sigma^+$ (v=0) and $A^2\Pi$ (v=0) states, respectively, with a standard deviation of 13 MHz.

Table 0.26 The observed and calculated transition wavenumber (cm^{-1}) for the $A\ ^2\Pi_r$-$X^2\Sigma^+$ (0, 0) band system of MgD.

Branch	J''	Observed	Obs.-calc.[a]	Branch	J''	Observed	Obs.-calc.
$^QP_{21}$	5/2	19280.5916	-0.0004	Q_1	1/2	19259.4133 (259.4111)	0.0011
	7/2	280.0879	0.0002		3/2	261.9366 (261.9357)	-0.0016
Q_2	3/2	280.6262 (280.6292)[b]	-0.0003		5/2	264.2849 (264.2789)	0.0001
	5/2	280.1369 (280.1294)	0.0009		7/2	266.5907 (266.5820)	0.0017
	9/2	281.3819 (280.3720)	0.0006		9/2	268.9653 (268.9583)	-0.0012
	11/2	282.9155	-0.0006	$^QR_{12}$	1/2	261.9572	-0.0017
$^SR_{21}$	1/2	298.6093	0.0013		3/2	264.3189	-0.0005
	3/2	310.0986	0.0011		5/2	266.6393	0.0020
$^RQ_{21}$	3/2	292.6010	-0.0005		7/2	269.0277	-0.0008
	5/2	298.0971	0.0006	R_1	1/2	267.9157 (267.9228)	-0.0016
	7/2	304.3668	-0.0014		3/2	276.2507 (276.2522)	-0.0016
	9/2	311.2991	0.0006		5/2	284.5418 (284.5440)	-0.0014
R_2	1/2	292.6221 (292.6109)	-0.0001		7/2	292.9023 (292.9499)	-0.0008
	3/2	298.1303 (298.0650)	-0.0007		9/2	301.4159 (301.4774)	0.0008
	5/2	304.4159 (304.4014)	-0.0006	$^PQ_{12}$	1/2	253.4096 (253.3985)	0.0007
	7/2	311.3612	0.0007		3/2	249.9364	0.0006
P_2	5/2	262.6396 (262.6517)	-0.0004		5/2	246.2918	0.0010
	7/2	256.1669 (256.1771)	0.0003		7/2	242.6136	0.0004
	9/2	250.4842	-0.0017	$^OP_{12}$	3/2	241.4293	-0.0014

		(250.4950)				(241.4302)	
	11/2	245.4853 (245.4887)	0.0007		5/2	231.9785 (231.9853)	0.0018
P_1	3/2	253.3886 (253.3985)	0.0004				
	5/2	249.9018 (249.9136)	0.0005				
	7/2	246.2438 (246.2606)	0.0013				
	9/2	242.5513 (242.6240)	0.0001				
	Std. Dev. = 0.0011 cm^{-1}						

a) Calculated using the optimized parameters given in Table 3.

b) The numbers in parentheses are the observed transition wavenumbers from Ref. 19.

Table 0.27 The observed and calculated Stark shifts of lines in $A\,^2\Pi_r$- $X^2\Sigma^+(0, 0)$ band system of MgD.

	Field			Obs	Dif
Branch	(V/cm)	$\|M_J'\|$	$\|M_J''\|$	(MHz)	(MHz)
$R_1(1/2)$	2250	1/2	1/2	-43	-4
∥	3375	1/2	1/2	-83	-1
	4499	1/2	1/2	-126	10
	4792	1/2	1/2	-137	14
	5096	1/2	1/2	-165	2
	5472	1/2	1/2	-190	-3
	5607	1/2	1/2	-210	-15
	6342	1/2	1/2	-237	-1
	7202	1/2	1/2	-285	0
	8114	1/2	1/2	-326	12
	8787	1/2	1/2	-382	-5
	9649	1/2	1/2	-423	4
	10526	1/2	1/2	-468	9
$R_1(1/2)$	2250	1/2	3/2	-325	-8
⊥		-1/2	1/2	-48	-9
	2812	1/2	3/2	-458	-11
		-1/2	1/2	-46	13
	3375	1/2	3/2	-606	-23
		-1/2	1/2	-88	-6
$Q_1(1/2)$	3375	1/2	1/2	1240	-3
∥					
$Q_1(1/2)$	281	-1/2	1/2	31	-2
⊥	450	-1/2	1/2	57	-12
	562	-1/2	1/2	100	-1
	1125	-1/2	1/2	295	-6
$^SR_{21}(1/2)$	1125	1/2	1/2	-263	-8
∥		1/2	1/2	313	-4
	2818	1/2	1/2	-687	-9
		1/2	1/2	760	16
	3375	1/2	1/2	-823	-4
		1/2	1/2	882	-6
	3375	1/2	1/2	-830	-11
		1/2	1/2	869	-19
$^SR_{21}(1/2)$	562	1/2	3/2	-395	1
⊥		-1/2	1/2	-119	-4
		-1/2	-1/2	164 [a]	-12
		1/2	3/2	441 [a]	-17

	1125	1/2	3/2	-848	-26
		-1/2	1/2	-278	-23
		-1/2	-1/2	295 [a]	-22
		1/2	3/2	858 [a]	-27
	2250	1/2	3/2	-1673	0
		-1/2	1/2	-554	-17
		-1/2	-1/2	564 [a]	-34
		1/2	3/2	1732 [a]	-7
	3375	1/2	3/2	-2530	-7
		-1/2	1/2	-843	-24
		-1/2	-1/2	888[a]	1
		1/2	3/2	2583[a]	-12

Standard deviation of fit = 13 MHz

[a] Field-induced transition.

Table 0.28 The determined field-free spectroscopic parameters for the $A\ ^2\Pi$ (v=0) state of MgD

Par.	Value	Correlation Coef.					
A	34.9902(9)	1.00					
B	3.18626(3)	-0.10	1.00				
γ	-0.0066(3)	0.71	0.07	1.00			
p	0.01425(2)	-0.01	0.08	0.09	1.00		
q	0.00067(5)	-0.10	-0.04	-0.06	0.10	1.00	
$T_0(A\ ^2\Pi)$	19270.5240(4)	0.43	-0.70	0.38	-0.00	-0.07	1.00
Std. dev= 0.0011							

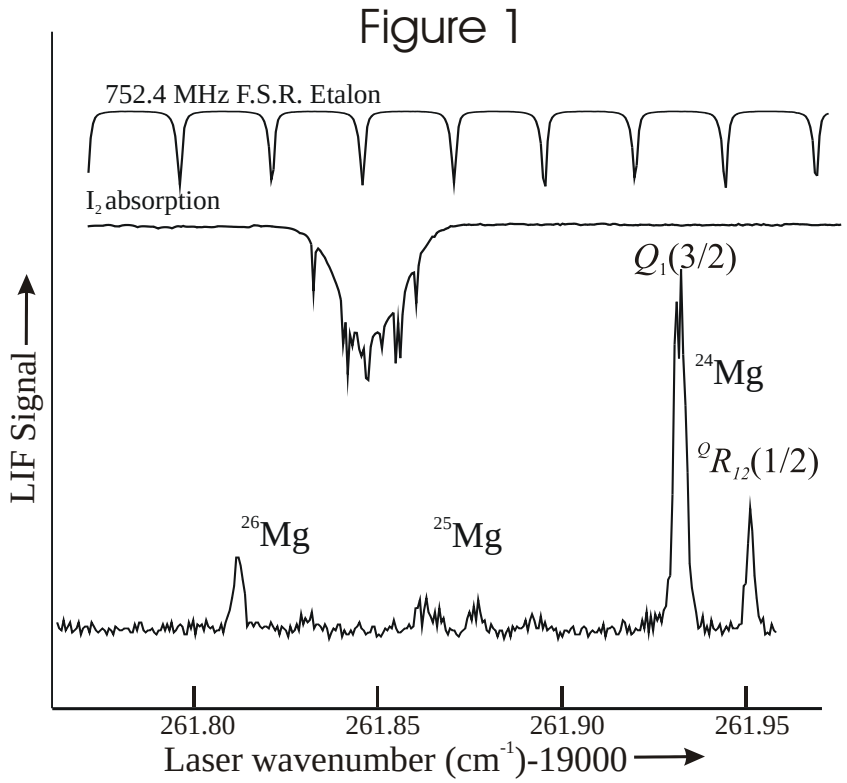

Figure 0.41 The observed $Q_1(3/2)$(ν =19261.9366 cm^{-1}) and $^{Q}R_{12}$ (1/2) (ν =19261.9572 cm^{-1}) field-free spectrum and the associated sub-Doppler I_2 spectrum (middle) and transmission of a stabilized confocal etalon. The $^{Q}R_{12}(J)$ satellite branch quickly becomes weak relative to the main $Q_1(J)$ branch.

Figure 2

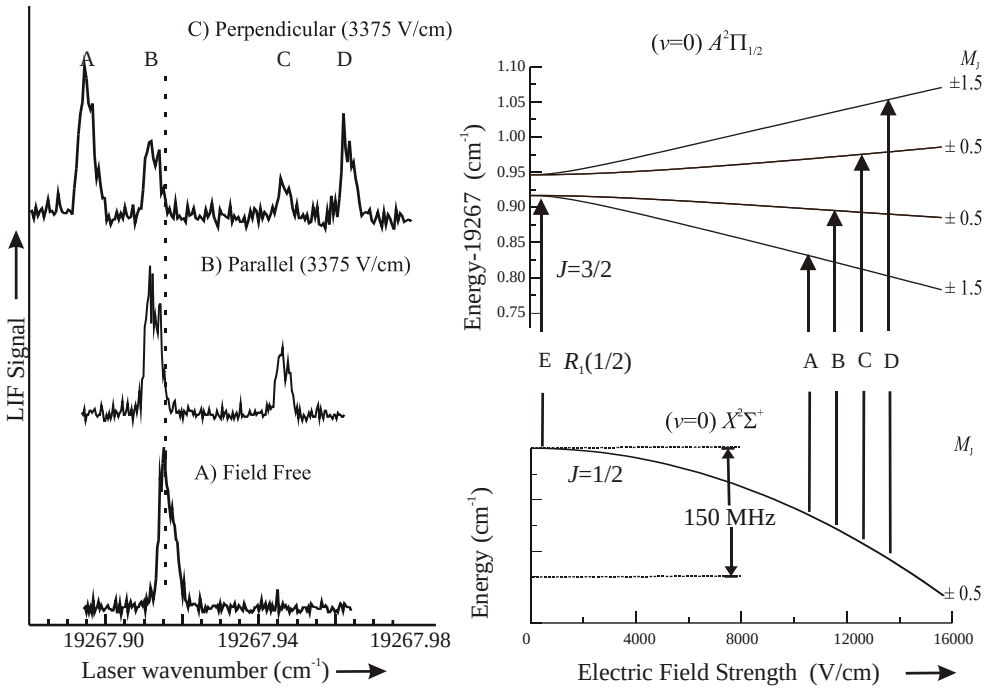

Figure 0.42 The $R_1(1/2)$ transition recorded field-free (lower), in the presence of the of 3375 V/cm with parallel (middle), and perpendicular (upper) polarization. The energy levels as a function of the applied electric field associated with the $R_1(1/2)$ transition are also given.

7. SUMMARY

The experimentally determined $\vec{\mu}_{el}$ values for AuF, AuCl, AuS, and AuO of this present study are listed Table 7.1 along with a comparison of the equilibrium bond lengths (r_0), reduced dipole moments ($\equiv \vec{\mu}_{el}/r_0$), ionization potential of ligands (I.P.), and electronegativity of ligands(E.N.). The v=0 equilibrium bond lengths, r_0, for AuF, AuCl and AuO were taken from previous studies of the pure rotational measurement [32, 36, 68, 100], whereas that of AuS was precisely determined by high-resolution study from our lab [73]. Instead of comparing the value of $\vec{\mu}_{el}$ between this group of gold-containing molecules, a comparison of $\vec{\mu}_{el}/r_0$ is more insightful because it emphasizes the change in electronic character. The electronegativity of the ligands is a good reference to represent the trend of $\vec{\mu}_{el}/r_0$, which in my cases is expected to be: AuS < AuO < AuCl < AuF. The observed ordering of $\vec{\mu}_{el}/r_0$ of the Au-containing molecules is approximately consistent with the ordering of ligand's electronegativity with the exception of the $\vec{\mu}_{el}/r_0$ of AuO being similar to that of AuCl. This ordering of $\vec{\mu}_{el}/r_0$ (i.e. AuS < AuO ≅ AuCl < AuF) can be further understood by looking at the nature of the orbitals.

The dominant configuration for the ground state of AuO and AuS predicated by high-level electronic structure calculations is [66, 69, 101]:

$$(1\sigma)^2(1\pi)^4(1\delta)^4(2\sigma)^2(2\pi)^3 \Rightarrow X^2\Pi_i, \tag{7.1}$$

whereas that of AuCl and AuF is very similar but with a fully occupied 2π orbital (i.e. $2\pi^4$ *vs*. $2\pi^3$), given as [39, 102]:

$$(1\sigma)^2(1\pi)^4(1\delta)^4(2\sigma)^2(2\pi)^4 \Rightarrow X^1\Sigma^+. \quad (7.2)$$

Table 0.29 Ground state $|\vec{\mu}_{el}|$ for AuX (X= Cl, F, O, and S)

	$\lvert\vec{\mu}_{el}\rvert$	r_0	$\lvert\vec{\mu}_{el}\rvert / r_0$	I.P.[g]	E.N.[h]
units	D	Å	D/ Å	eV	
AuCl	3.69[a]	2.1990[b]	1.68	12.97	3.16
AuF	4.32[c]	1.9184[d]	2.25	17.42	3.98
AuO	2.94[e]	1.8487[f]	1.59	13.61	3.44
AuS	2.22[e]	2.1556[e]	1.03	10.36	2.58

[a] Ref. [51]. [b] Ref. [100]. [c] Ref. [28]. [d] Ref. [32]. [e] Ref. [76]. [f] Ref. [103] [g] Ionization potential of ligand. [h] Electronegativity of ligand (in Pauling scale).

The M.O. correlation diagram of AuF, AuCl, AuS, and AuCl is illustrated in Figure 7.1. The orbital energies of the ligands are estimated as the ionization potential (as shown in Table 7.1) with the values of: S(3*p*) ~-10.36 eV, Cl(3*p*) ~-12.97 eV, O(2*p*) ~-13.61 eV, and F(2*p*) ~-17.42 eV. The orbital energies for Au(5*d*) and Au(6*s*) are approximately -19.7 eV and -9.1 eV. The similarity on the energies of the F(2*p*) orbital of Au(5*d*) causes the 2σ orbital of AuF to be essentially the F($2p_0$) orbital and the 2π orbital a strongly admitxture by: $\cong 0.8 * 5d_{\pm 1}(\mathrm{Au}) + 0.6 * 2p_{\pm 1}(\mathrm{F})$ [51]. In the case of AuS, AuO, and AuCl, the 1σ, 1π, and 1δ molecular orbitals are mostly derived from the Au 5*d* orbitals, with minor contributions (for 1σ and 1π) from S(3*p*), O(2*p*), and Cl(3*p*). The 2σ orbital is bonding of Au(6*s*) + ligand(p_0) polarized towards the ligand because the energy of the Au(6*s*)(~9.1 eV) is close to that of the S(3*p*) (~10.36 eV), Cl(3*p*)(~12.97 eV), and O(2*p*) (~13.61 eV) orbitals. The 2π orbital in these three molecules is essentially a non-bonding ligand-centered *p*-orbital. The ordering of $\vec{\mu}_{el} / r_0$ (i.e. AuS < AuO ≅ AuCl < AuF) coincides with

the energy ordering of the ligand 2p and 3p orbitals (i.e. S(3*p*) < Cl(3*p*) ≅ O(2*p*) < F(2*p*)) because of the change in polarization of the 2σ orbital.

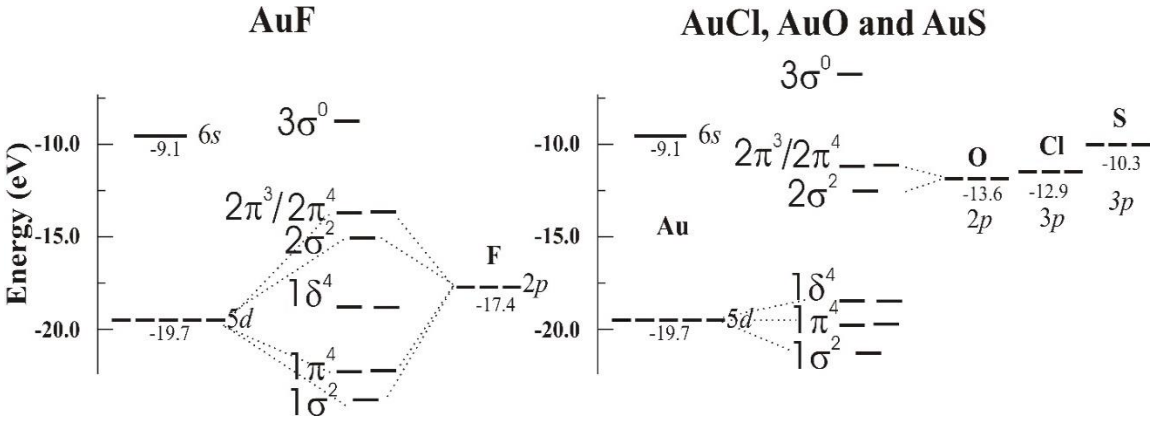

Figure 0.43 M.O. correlation diagram of Au-containing molecules.

In addition to understanding the trend in $\vec{\mu}_{el}/r_0$ for a series of Au-X molecules, it is also insightful to look at the trend when the metal is modified. The experimental determined dipole moment of PtF has been discussed in Chapter 6. Here the determined $\vec{\mu}_{el}$, r_0, and the ratio of $\vec{\mu}_{el}/r_0$ for the ground state of AuF, PtF, and IrF are compared in Table 7.2. The reduced dipole moment, $\vec{\mu}_{el}/r_0$, for the $X^2\Pi_{3/2}$ state of AuF (=2.25 D/Å) is significantly larger than that for the $X^2\Pi_{3/2}$ state of PtF (=1.83 D/Å), whereas that of PtF is larger than the $X^3\Phi_4$ state of IrF (=1.52 D/Å). The ordering of $\vec{\mu}_{el}$ (i.e. AuF > PtF > IrF) is strongly dependent upon the relative contribution of the $5d^n$ and $5d^{n-1}6s^1$ (n=7, 8 and 9 for Ir^+, Pt^+, and Au^+, respectively) configurations. The 6*s* orbital on the metal will ligand-field mixed with the $6p_0$ orbital resulting in the molecular orbital being polarized away from the electrophilic center of F^-. This back polarization reduces $\vec{\mu}_{el}$ value. Therefore, the

electronic states with a dominant $5d^n$ configurations will have a significantly larger $\vec{\mu}_{el}$ value than those with a dominant $5d^{n-1}6s^1$ configurations. As discussed above, the $X^2\Pi_{3/2}$ state of AuF has a pure $5d^{10}$ configuration with no contribution from the 6*s* of Au, whereas the $X^2\Pi_{3/2}$ state of PtF are equally contributed by the $5d^9$ configuration and $5d^86s^1$ configuration as revealed by the hyperfine analysis [77]. For the $X^3\Phi_4$ state of IrF, the analysis of magnetic hyperfine structure in previous study indicates that the $X^3\Phi_4$ state has an approximate 66% contribution from the $5d^76s^1$ configuration and a 33% contribution from the $5d^9$ configuration [104]. The ordering of the contribution from the $5d^{n-1}6s^1$ configurations (i.e. IrF > PtF > AuF) is consistent with the observation of $\vec{\mu}_{el} / r_0$.

Table 0.30 Determined results of $\vec{\mu}_{el}$, r_0, and the ratio of $\vec{\mu}_{el}/r_0$ for the ground state of AuF, PtF, and IrF.

	$\lvert\vec{\mu}_{el}\rvert$	r_0	$\lvert\vec{\mu}_{el}\rvert/r_0$
units	D	Å	D/ Å
AuF	4.32[a]	1.918	2.25
PtF	3.42[b]	1.868	1.83
IrF	2.82[c]	1.851	1.52

[a] Ref. [28]. [b] Ref. [77]. [c] Ref. [104].

REFERENCES

1. Wollaston, W.H., *A Method of Examining Refractive and Dispersive Powers, by Prismatic Reflection.* Phil. Trans. R. Soc. Lond., 1802. 92: p. 15.

2. Fraunhofer, J., *Bestimmung des Brechungs- und des Farben-Zerstreuungs - Vermögens verschiedener Glasarten, in Bezug auf die Vervollkommnung achromatischer Fernröhre.* Denkschriften der Königlichen Akademie der Wissenschaften zu München, 1814. 5: p. 33.

3. Brust, M., et al., *Synthesis of thiol-derivatized gold nanoparticles in a two-phase liquid-liquid system.* J. Chem. Soc., Chem. Commun., 1994(7): p. 801-2.

4. Schmidbaur, H., et al., *Understanding gold chemistry through relativity.* Chemical Physics, 2005. 311(1-2): p. 151-161.

5. Schmidbaur, H., *Gold Chemistry is Different.* Interdisciplinary Science Reviews, 1992. 17(3): p. 213-220.

6. Sommer, A., *Alloys of gold with alkali metals [2].* Nature, 1943. 152(3851): p. 215.

7. Pyykko, P., *Relativity, gold, closed-shell interactions, and CsAu·NH3.* Angew. Chem., Int. Ed., 2002. 41(19): p. 3573-3578.

8. Zintl, E., J. Goubeau, and W. Dullenkopf, *Metals and alloys. I. Salt-like compounds and intermetallic phases of sodium in liquid ammonia.* Z. physik. Chem., 1931. 154(Abt. A): p. 1-46.

9. Biltz, W., et al., *The valence and chemical compression in metals combined with gold.* Z. Anorg. Allg. Chem., 1938. 236: p. 12-23.

10. Heymann, E. and H.P. Weber, *The distribution equilibrium of sodium between molten sodium halides (NaBr, NaI) and a molten metal phase (Cd, Pb, Tl, Sn, Bi, Sb, Au).* Trans. Faraday Soc., 1938. 34: p. 1492-1501.

11. Eliav, Kaldor, and Ishikawa, *Open-shell relativistic coupled-cluster method with Dirac-Fock-Breit wave functions: Energies of the gold atom and its cation.* Phys Rev A, 1994. 49(3): p. 1724-1729.

12. Pyykko, P., *Theoretical chemistry of gold.* Angew Chem Int Ed Engl, 2004. 43(34): p. 4412-56.

13. Christensen, N.E. and B.O. Seraphin, *Relativistic Band Calculation and the Optical Properties of Gold.* Physical Review B, 1971. 4(10): p. 3321-3344.

14. Desclaux, J.P. and P. Pyykko, *Dirac-Fock one-center calculations. The molecules copper monohydride, silver hydride and gold monohydride including p-type symmetry functions.* Chem. Phys. Lett., 1976. 39(2): p. 300-3.

15. Pyykko, P. and J.P. Desclaux, *Relativity and the periodic system of elements.* Acc. Chem. Res., 1979. 12(8): p. 276-81.

16. Pyykko, P., *Relativistic effects in structural chemistry.* Chem. Rev., 1988. 88(3): p. 563-94.

17. Basch, H. and S. Topiol, *Relativistic effects in ab initio effective core potential studies of heavy metal compounds. Application to HgCl2, AuCl, and PtH.* The Journal of Chemical Physics, 1979. 71(2): p. 802-814.

18. Pyykkö, P., *Theoretical chemistry of gold. II.* Inorganica Chimica Acta, 2005. 358(14): p. 4113-4130.

19. Pyykko, P., *Theoretical chemistry of gold. III.* Chem Soc Rev, 2008. 37(9): p. 1967-97.

20. Brown, J.M. and A. Carrington, *Rotational Spectroscopy of Diatomic Molecules*. 2003, Cambridge: Cambridge University Press.

21. Frosch, R.A. and H.M. Foley, *Magnetic hyperfine structure in diatomic molecules.* Phys. Rev., 1952. 88: p. 1337-49.

22. Kristiansen, P. and L. Veseth, *Many-body calculations of hyperfine constants in diatomic molecules. I. The ground state of hydroxyl (16OH).* J. Chem. Phys., 1986. 84(5): p. 2711-19.

23. Wang, F. and T.C. Steimle, *Hyperfine interaction and Stark effect in the b 3Pi-X 1Sigma+(0,0) band of copper monofluoride, CuF.* J Chem Phys, 2010. 132(5): p. 054301.

24. Steimle, T.C., et al., *Molecular-beam optical Stark and Zeeman study of theA2Π--X2Σ+(0,0) band system of BaF.* Physical Review A, 2011. 84(1).

25. Zare, R.N., *Rotational Line Strengths: The O_2^+ $b^4\Sigma_g^-$ - $a^4\Pi_u$ Band System*. Molecular Spectroscopy: Modern Research, ed. K.N. Rao and C.W. Mathews. 1972, New York: Academic Press.

26. Kantrowitz, A. and J. Grey, *A High Intensity Source for the Molecular Beam. Part I. Theoretical.* Review of Scientific Instruments, 1951. 22(5): p. 328-332.

27. Scoles, G. and F. Torello, *Supersonic molecular beams production and temperature distribution in free expanding jets.* Meccanica, 1968. 3(1): p. 20-27.

28. Steimle, T.C., et al., *Molecular-beam optical stark and zeeman study of the $[17.8]0^+$-$X^1\Sigma^+$(0,0) band system of AuF*. J Phys Chem A, 2013. 117(46): p. 11737-44.

29. Saenger, K.L. and C.P. Sun, *Yellow emission bands produced during gold etching inO2-CF4rf glow-discharge plasmas: Evidence for gas-phase AuF.* Physical Review A, 1992. 46(1): p. 670-673.

30. Ferguson, W.F.C., *The Spectrum of Gold Chloride.* Physical Review, 1928. 31(6): p. 969-972.

31. Andreev, S. and J.J. BelBruno, *Detection of AuF by emission spectroscopy in a hollow cathode discharge.* Chem. Phys. Lett., 2000. 329(5,6): p. 490-494.

32. Okabayashi, T., et al., *Millimeter- and submillimeter-wave spectroscopy of AuF in the ground X1Σ+ state.* Chem. Phys. Lett., 2002. 366(3,4): p. 406-411.

33. Knurr, B.J., E.K. Butler, and T.D. Varberg, *Electronic Spectrum of AuF: Hyperfine Structure of the [17.7]1 State.* J. Phys. Chem. A, 2009. 113(47): p. 13428-13435.

34. Butler, E.K., et al., *Excited Electronic States of AuF.* J. Phys. Chem. A, 2010. 114(14): p. 4831-4834.

35. O'Brien, Elliott, and Dulick, *Fourier Transform Emission Spectroscopy of the Visible Transitions of AuCl.* J Mol Spectrosc, 1999. 194(1): p. 124-127.

36. Okabayashi, T., et al., *Millimeter- and submillimeter-wave spectra of AuCl and AuBr in the X1Σ+ electronic ground states.* J. Mol. Spectrosc., 2003. 220(2): p. 155-161.

37. Schwerdtfeger, P., et al., *Relativistic effects in gold chemistry. I. Diatomic gold compounds.* The Journal of Chemical Physics, 1989. 91(3): p. 1762-1774.

38. Iliaš, M., P. Furdík, and M. Urban, *Comparative Study of Electron Correlation and Relativistic Effects in CuF, AgF, and AuF.* The Journal of Physical Chemistry A, 1998. 102(27): p. 5263-5268.

39. Guichemerre, M., G. Chambaud, and H. Stoll, *Electronic structure and spectroscopy of monohalides of metals of group I-B.* Chem. Phys., 2002. 280(1-2): p. 71-102.

40. Goll, E., et al., *Improved dipole moments by combining short-range gradient-corrected density-functional theory with long-range wave-function methods.* Physical Review A, 2007. 76(3).

41. Holka, F., et al., *The (hyper)polarizabilities of AuXeF and XeAuF.* Chemical Physics Letters, 2009. 472(4-6): p. 185-189.

42. Schwerdtfeger, P., et al., *Breakdown of the pseudopotential approximation for magnetizabilities and electric multipole moments: test calculations for Au, AuF, and Sn(n) cluster (n </= 20).* J Chem Phys, 2011. 134(20): p. 204102.

43. Hill, J.G. and K.A. Peterson, *Explicitly Correlated Coupled Cluster Calculations for Molecules Containing Group 11 (Cu, Ag, Au) and 12 (Zn, Cd, Hg) Elements:*

Optimized Complementary Auxiliary Basis Sets for Valence and Core-Valence Basis Sets. J. Chem. Theory Comput., 2012. 8(2): p. 518-526.

44. Suzumura, T., T. Nakajima, and K. Hirao, *Ground-state properties of MH, MCl, and M2 (M = Cu, Ag, and Au) calculated by a scalar relativistic density functional theory.* Int. J. Quantum Chem., 1999. 75(4/5): p. 757-766.

45. Brown, J.R., et al., *Experimental and theoretical studies of diatomic gold halides.* J. Am. Soc. Mass Spectrom., 2002. 13(5): p. 485-492.

46. Figgen, D., et al., *Energy-consistent pseudopotentials for group 11 and 12 atoms: adjustment to multi-configuration Dirac–Hartree–Fock data.* Chemical Physics, 2005. 311(1-2): p. 227-244.

47. Pantazis, D.A., et al., *All-Electron Scalar Relativistic Basis Sets for Third-Row Transition Metal Atoms.* J. Chem. Theory Comput., 2008. 4(6): p. 908-919.

48. Rabilloud, F., *Structure and stability of coinage metal fluoride and chloride clusters (MnFn and MnCln, M = Cu, Ag, or Au; n = 1-6).* J. Comput. Chem., 2012. 33(26): p. 2083-2091.

49. Yoshizawa, T. and S. Sakaki, *NMR shielding constants of CuX, AgX, and AuX (X = F, Cl, Br, and I) investigated by density functional theory based on the Douglas-Kroll-Hess hamiltonian.* J. Comput. Chem., 2013. 34(12): p. 1013-1023.

50. Figgen, D., et al., *Energy-consistent pseudopotentials for group 11 and 12 atoms: adjustment to multi-configuration Dirac-Hartree-Fock data.* Chem. Phys., 2005. 311(1-2): p. 227-244.

51. Zhang, R., et al., *The permanent electric dipole moment of gold chloride, AuCl.* Molecular Physics, 2015. 113(15-16): p. 2073-2080.

52. Laerdahl, J.K., T. Saue, and K. Faegri, Jr., *Direct relativistic MP2. Properties of ground state CuF, AgF, and AuF.* Theor. Chem. Acc., 1997. 97(1-4): p. 177-184.

53. Xiang, L., et al., *Gate-controlled conductance switching in DNA.* Nat Commun, 2017. 8: p. 14471.

54. Li, Y., et al., *Thermoelectric effect and its dependence on molecular length and sequence in single DNA molecules.* Nat Commun, 2016. 7: p. 11294.

55. Huang, C., et al., *Break junction under electrochemical gating: testbed for single-molecule electronics.* Chem Soc Rev, 2015. 44(4): p. 889-901.

56. Elbing, M., et al., *A single-molecule diode.* Proc Natl Acad Sci U S A, 2005. 102(25): p. 8815-20.

57. Vericat, C., et al., *Self-assembled monolayers of thiols and dithiols on gold: new challenges for a well-known system.* Chem Soc Rev, 2010. 39(5): p. 1805-34.

58. Pensa, E., et al., *The Chemistry of the Sulfur-Gold Interface: In Search of a Unified Model.* Acc. Chem. Res., 2012. 45(8): p. 1183-1192.

59. Azcárate, J.C., et al., *Understanding the Surface Chemistry of Thiolate-Protected Metallic Nanoparticles.* The Journal of Physical Chemistry Letters, 2013. 4(18): p. 3127-3138.

60. Love, J.C., et al., *Self-Assembled Monolayers of Thiolates on Metals as a Form of Nanotechnology.* Chem. Rev. (Washington, DC, U. S.), 2005. 105(4): p. 1103-1169.

61. Ulman, A., *Formation and Structure of Self-Assembled Monolayers.* Chem. Rev. (Washington, D. C.), 1996. 96(4): p. 1533-1554.

62. Zielasek, V., et al., *Gold catalysts: nanoporous gold foams.* Angew Chem Int Ed Engl, 2006. 45(48): p. 8241-4.

63. Baker, T.A., X. Liu, and C.M. Friend, *The mystery of gold's chemical activity: local bonding, morphology and reactivity of atomic oxygen.* Phys Chem Chem Phys, 2011. 13(1): p. 34-46.

64. Biener, J., et al., *Nanoporous Gold: Understanding the Origin of the Reactivity of a 21st Century Catalyst Made by Pre-Columbian Technology.* ACS Catalysis, 2015. 5(11): p. 6263-6270.

65. Ichino, T., et al., *Photoelectron Spectroscopy of AuO^- and AuS^-*. J. Phys. Chem. A, 2004. 108(51): p. 11307-11313.

66. Zhai, H.-J., et al., *Probing the Electronic Structure and Chemical Bonding of Gold Oxides and Sulfides in AuOn- and AuSn- (n = 1, 2).* J. Am. Chem. Soc., 2008. 130(28): p. 9156-9167.

67. Liu, H.T., et al., *Vibrational State-Selective Resonant Two-Photon Photoelectron Spectroscopy of AuS(-) via a Spin-Forbidden Excited State.* J Phys Chem Lett, 2015. 6(4): p. 637-42.

68. Okabayashi, T., et al., *Pure rotational spectrum of gold monoxide (AuO) in the X2Π3/2 state.* Chemical Physics Letters, 2005. 403(1-3): p. 223-227.

69. O'Brien, L.C., A.E. Oberlink, and B.O. Roos, *The Electronic Spectrum of AuO: A Combined Theoretical and Experimental Study.* J. Phys. Chem. A, 2006. 110(43): p. 11954-11957.

70. O'Brien, L.C., S.C. Hardimon, and J.J. O'Brien, *Spectroscopy of AuO: Identification of the [10.7] Π3/2 to X2Π3/2 Transition.* J. Phys. Chem. A, 2004. 108(51): p. 11302-11306.

71. Shaji, S., et al., *Intracavity laser absorption spectroscopy of AuO: Identification of the b4Π3/2–X2Π3/2 transition.* Journal of Molecular Spectroscopy, 2007. 243(1): p. 37-42.

72. O'Brien, L.C., et al., *Intracavity laser absorption spectroscopy of AuO: Identification of the B 2Σ−–X 2Π3/2 transition.* Journal of Molecular Spectroscopy, 2008. 252(2): p. 136-142.

73. Kokkin, D.L., et al., *Au-S Bonding Revealed from the Characterization of Diatomic Gold Sulfide, AuS.* J Phys Chem A, 2015. 119(48): p. 11659-67.

74. Schwerdtfeger, P., et al., *Relativistic effects in gold chemistry. I. Diatomic gold compounds.* J. Chem. Phys., 1989. 91(3): p. 1762-74.

75. Kraka, E., M. Filatov, and D. Cremer, *Comparison of gold bonding with mercury bonding.* Croat. Chem. Acta, 2009. 82(1): p. 233-243.

76. Zhang, R., et al., *The electric dipole moments in the ground states of gold oxide, AuO, and gold sulfide, AuS.* J Chem Phys, 2017. 146(6): p. 064307.

77. Qin, C., et al., *The permanent electric dipole moment and hyperfine interactions in platinum monofluoride, PtF.* J Chem Phys, 2012. 137(5): p. 054309.

78. Qin, C., et al., *The pure rotational spectrum of platinum monocarbide, PtC.* Chemical Physics Letters, 2012. 535: p. 40-43.

79. Steimle, T.C., R. Zhang, and H. Wang, *The electric dipole moment of magnesium deuteride, MgD.* J Chem Phys, 2014. 140(22): p. 224308.

80. Zhang, R. and T.C. Steimle, *Optical Zeeman Spectroscopy of the (0, 0) $a^2\Pi$-$X^2\Sigma^+$ Band System of Magnesium Hydride.* The Astrophysical Journal, 2014. 781(1): p. 51.

81. Karpov, A., et al., *Covalently Bonded 1 ∞[Pt]- Chains in BaPt: Extension of the Zintl-Klemm Concept to Anionic Transition Metals?* J. Am. Chem. Soc., 2004. 126(43): p. 14123-14128.

82. Pavlenko, Y.V., et al., *The electronic bands of CrD, CrH, MgD and MgH: application to the 'deuterium test'.* Monthly Notices of the Royal Astronomical Society, 2008. 386(3): p. 1338-1346.

83. Tennyson, J. and S.N. Yurchenko, *ExoMol: molecular line lists for exoplanet and other atmospheres.* Monthly Notices of the Royal Astronomical Society, 2012. 425(1): p. 21-33.

84. Shayesteh, A. and P.F. Bernath, *Rotational analysis and deperturbation of the A2Pi --> X2Sigma+ and B'2Sigma+ --> X2Sigma+ emission spectra of MgH.* J Chem Phys, 2011. 135(9): p. 094308.

85. Berdyugina, S.V. and S.K. Solanki, *The molecular Zeeman effect and diagnostics of solar and stellar magnetic fields.* Astronomy and Astrophysics, 2002. 385(2): p. 701-715.

86. Berdyugina, S.V., S.K. Solanki, and C. Frutiger, *The molecular Zeeman effect and diagnostics of solar and stellar magnetic fields.* Astronomy and Astrophysics, 2003. 412(2): p. 513-527.

87. Berdyugina, S.V., et al., *The molecular Zeeman effect and*

diagnostics of solar and stellar magnetic fields. Astronomy & Astrophysics, 2005. 444(3): p. 947-960.

88. Bethlem, H.L., et al., *Alternating gradient focusing and deceleration of polar molecules.* J. Phys. B: At., Mol. Opt. Phys., 2006. 39(16): p. R263-R291.

89. Hogan, S.D., M. Motsch, and F. Merkt, *Deceleration of supersonic beams using inhomogeneous electric and magnetic fields.* Phys. Chem. Chem. Phys., 2011. 13(42): p. 18705-18723.

90. van de Meerakker, S.Y.T., et al., *Manipulation and Control of Molecular Beams.* Chem. Rev. (Washington, DC, U. S.), 2012. 112(9): p. 4828-4878.

91. Steimle, T.C., K.Y. Jung, and B.Z. Li, *The permanent electric dipole moment of PtO, PtS, PtN, and PtC.* J. Chem. Phys., 1995. 103(5): p. 1767-72.

92. Steimle, T.C., K.Y. Jung, and B.Z. Li, *A supersonic molecular beam spectroscopic study of platinum monocarbide, PtC.* The Journal of Chemical Physics, 1995. 102(15): p. 5937-5941.

93. Beaton, S.A. and T.C. Steimle, *Laser-induced fluorescence and Optical/Stark spectroscopy of PtC.* The Journal of Chemical Physics, 1999. 111(24): p. 10876-10882.

94. Womack, K., et al., *High resolution electronic spectroscopy of the A2Σ- - X2Π1/2 transition of PtN.* J. Chem. Phys., 2014. 141(8): p. 084304/1-084304/8.

95. Childs, W.J., *Overview of laser-radiofrequency double-resonance studies of atomic, molecular, and ionic beams.* Phys. Rep., 1992. 211(3): p. 113-65.

96. Scurlock, C.T., D.A. Fletcher, and T.C. Steimle, *Hyperfine structure in the (0,0,0) ~X2Σ+ state of calcium monohydroxide observed by pump/probe microwave-optical double resonance.* J. Mol. Spectrosc., 1993. 159(2): p. 350-6.

97. Appelblad, O., C. Nilsson, and R. Scullman, *Vibrational and rotational analysis of some band systems of the molecule platinum carbide.* Phys. Scr., 1973. 7(1-2): p. 65-71.

98. Okabayashi, T., et al., *Microwave spectroscopy of platinum monofluoride and platinum monochloride in the X 2Π3/2 states.* J. Chem. Phys., 2012. 136(17): p. 174311/1-174311/9.

99. Zink, L.R., et al., *Laboratory measurements for the astrophysical identification of magnesium hydride (MgH).* Astrophys. J., 1990. 359(2, Pt. 2): p. L65-L66.

100. Evans, C.J. and M.C. Gerry, *The Pure Rotational Spectra of AuCl and AuBr*. J Mol Spectrosc, 2000. 203(1): p. 105-117.

101. Liang, Y.-n. and F. Wang, *Theoretical studies on low-lying states of AuX (X = O, S).* Wuli Huaxue Xuebao, 2014. 30(8): p. 1447-1455.

102. Magnko, L., et al., *A comparison of metallophilic attraction in (X-M-PH3)2 (M = Cu, Ag, Au; X = H, Cl).* Phys. Chem. Chem. Phys., 2002. 4(6): p. 1006-1013.

103. Okabayashi, T., et al., *Pure rotational spectrum of gold monoxide (AuO) in the X2Π3/2 state.* Chem. Phys. Lett., 2005. 403(1-3): p. 223-227.

104. Zhuang, X., T.C. Steimle, and C. Linton, *The electric dipole moment of iridium monofluoride, IrF*. J. Chem. Phys., 2010. 133(16): p. 164310/1-164310/6.

APPENDIX A

MATRIX ELEMENTS OF THE HAMILTONIANS EVALUATED IN A CASE (a_β) BASIS SET FOR DIATOMIC MOLECULES WITH ONE NUCLEAR SPIN

(J.M.Brown, I. Kopp, C. Malmberg and B. Rydh, Physica Scripta 17, 55(1978).)

(1) Matrix elements for spin-orbit interaction, $\hat{H}_{so}$:

$\left\langle \eta\Lambda S\Sigma J\Omega IF \left| \hat{H}_{so} \right| \eta\Lambda S\Sigma J\Omega IF \right\rangle = A\Lambda\Sigma$.

(2) Matrix elements for spin-spin interaction, $\hat{H}_{ss}$:

$\left\langle \eta\Lambda S\Sigma J\Omega IF \left| \hat{H}_{ss} \right| \eta\Lambda S\Sigma J\Omega IF \right\rangle = \frac{2}{3}\lambda[3\Sigma^2 - S(S+1)]$.

(3) Matrix elements for spin-rotation interaction, $\hat{H}_{sr}$:

$\left\langle \eta\Lambda S\Sigma' J\Omega' IF \left| \hat{H}_{sr} \right| \eta\Lambda S\Sigma J\Omega IF \right\rangle$

$= \gamma \left\{ \delta_{\Sigma'\Sigma}\delta_{\Omega'\Omega} \times [\Sigma^2 - S(S+1)] + \sum_{q=\pm 1} (-1)^{phase1} \times threeJ1 \times par1 \right\}, with$

$phase1 = J - \Omega' + S - \Sigma';$

$threeJ1 = \begin{pmatrix} J & 1 & J \\ -\Omega' & q & \Omega \end{pmatrix} \begin{pmatrix} S & 1 & S \\ -\Sigma' & q & \Sigma \end{pmatrix};$

$par1 = \sqrt{J(J+1)(2J+1)S(S+1)(2S+1)}.$

(4) Matrix elements for the rotation, $\hat{H}_{rot}$:

$\left\langle \eta\Lambda S\Sigma' J\Omega' IF \left| \hat{H}_{rot} \right| \eta\Lambda S\Sigma J\Omega IF \right\rangle$

$= B \left\{ \delta_{\Sigma'\Sigma}\delta_{\Omega'\Omega} \times par1 - 2\sum_{q=\pm 1} (-1)^{phase1} \times threeJ1 \times par2 \right\}, with$

$par1 = J(J+1) - \Omega^2 + S(S+1) - \Sigma^2 + \left\langle L_x^2 + L_y^2 \right\rangle;$

$phase1 = J - \Omega' + S - \Sigma';$

$threeJ1 = \begin{pmatrix} J & 1 & J \\ -\Omega' & q & \Omega \end{pmatrix} \begin{pmatrix} S & 1 & S \\ -\Sigma' & q & \Sigma \end{pmatrix};$

$par2 = \sqrt{J(J+1)(2J+1)S(S+1)(2S+1)}.$

(5) Matrix elements for the centrifugal distortion, $\hat{H}_{CD}$:

$$\langle \eta \Lambda S \Sigma' J \Omega' IF | \hat{H}_{cd} | \eta \Lambda S \Sigma J \Omega IF \rangle$$

$$= -D \left\{ \delta_{\Sigma'\Sigma} \delta_{\Omega'\Omega} \times term1 - 2 \sum_{q=\pm 1} (-1)^{phase1} \times threeJ2 \times par3 \times par4 \right\}, with$$

$$term1 = par1 + 4 \sum_{q=\pm 1} \sum_{\Omega''} threeJ1 \times par2$$

$$par1 = [J(J+1) - \Omega^2 + S(S+1) - \Sigma^2]^2;$$

$$threeJ1 = \begin{pmatrix} J & 1 & J \\ -\Omega & q & \Omega'' \end{pmatrix}^2 \begin{pmatrix} S & 1 & S \\ -\Sigma & q & \Sigma'' \end{pmatrix}^2;$$

$$par2 = J(J+1)(2J+1)S(S+1)(2S+1);$$

$$phase1 = J - \Omega' + S - \Sigma';$$

$$threeJ2 = \begin{pmatrix} J & 1 & J \\ -\Omega' & q & \Omega \end{pmatrix} \begin{pmatrix} S & 1 & S \\ -\Sigma' & q & \Sigma \end{pmatrix};$$

$$par3 = \sqrt{J(J+1)(2J+1)S(S+1)(2S+1)};$$

$$par4 = 2J(J+1) - (\Omega')^2 - \Omega^2 + 2S(S+1) - (\Sigma')^2 - \Sigma^2.$$

(6) Matrix elements for the Λ-doubling, $\hat{H}_{LD}$:

$$\langle \eta \Lambda' S \Sigma' J \Omega' IF | \hat{H}_{LD} | \eta \Lambda S \Sigma J \Omega IF \rangle$$

$$= \sum_{q=\pm 1} \delta_{\Lambda', \Lambda \mp 2} \{ \delta_{\Omega'\Omega} (o + p + q) \times term1 + (p + 2q) \times term2 + \delta_{\Sigma'\Sigma} q \times term3 \}, with$$

$$term1 = \sum_{\Sigma''} (-1)^{phase1} \times threeJ1 \times par1;$$

$$term2 = (-1)^{phase2} \times threeJ2 \times par2;$$

$$term3 = \sum_{\Omega''} (-1)^{phase3} \times threeJ3 \times par3;$$

$$phase1 = (S - \Sigma') + (S - \Sigma'')$$

$$threeJ1 = \begin{pmatrix} S & 1 & S \\ -\Sigma' & q & \Sigma'' \end{pmatrix} \begin{pmatrix} S & 1 & S \\ -\Sigma'' & q & \Sigma \end{pmatrix};$$

$$par1 = S(S+1)(2S+1);$$

$$phase2 = (J - \Omega') + (S - \Sigma');$$

$$threeJ2 = \begin{pmatrix} J & 1 & J \\ -\Omega' & -q & \Omega \end{pmatrix} \begin{pmatrix} S & 1 & S \\ -\Sigma' & q & \Sigma \end{pmatrix};$$

$$par2 = \sqrt{J(J+1)(2J+1)S(S+1)(2S+1)};$$

$$phase3 = (J - \Omega') + (J - \Omega'');$$

$$threeJ3 = \begin{pmatrix} J & 1 & J \\ -\Omega' & -q & \Omega'' \end{pmatrix} \begin{pmatrix} J & 1 & J \\ -\Omega'' & -q & \Omega \end{pmatrix};$$

$$par3 = J(J+1)(2J+1).$$

(7) Matrix elements for the magnetic hyperfine interaction, $\hat{H}_{mhyf}$:

$$\langle \eta\Lambda' S\Sigma' J'\Omega' IF | \hat{H}_{hfs} | \eta\Lambda S\Sigma J\Omega IF \rangle$$

$$= \delta_{\Lambda'\Lambda} \left\{ term1 \times \sum_q (-1)^{J'-\Omega'} \times threeJ1 \times [a \times term2 + b_F \times term3 + c \times term4] \right\} - d \times term5, with$$

$$term1 = (-1)^{J+I+F} \times par1 \times \begin{Bmatrix} F & J & I \\ 1 & I & J' \end{Bmatrix};$$

$$term2 = \Lambda \delta_{\Sigma'\Sigma} \delta_{\Omega'\Omega};$$

$$term3 = (-1)^{S-\Sigma'} \times \begin{pmatrix} S & 1 & S \\ -\Sigma' & q & \Sigma \end{pmatrix} \sqrt{S(S+1)(2S+1)};$$

$$term4 = \frac{\sqrt{30}}{3} (-1)^{q+(S-\Sigma')} \begin{pmatrix} S & 1 & S \\ -\Sigma' & q & \Sigma'' \end{pmatrix} \begin{pmatrix} 1 & 2 & 1 \\ -q & 0 & q \end{pmatrix} \sqrt{S(S+1)(2S+1)};$$

$$term5 = \sum_{q=\pm 1} \delta_{\Lambda',\Lambda\mp 2} (-1)^{phase1} \times par1 \times \begin{Bmatrix} F & J & I \\ 1 & I & J' \end{Bmatrix} \begin{pmatrix} S & 1 & S \\ -\Sigma' & q & \Sigma \end{pmatrix} \times threeJ1 \times \sqrt{S(S+1)(2S+1)};$$

$$phase1 = (J + I + F) + (J' - \Omega') + (q + S - \Sigma');$$

$$par1 = \sqrt{I(I+1)(2I+1)(2J'+1)(2J+1)}.$$

$$threeJ1 = \begin{pmatrix} J' & 1 & J \\ -\Omega' & -q & \Omega \end{pmatrix};$$

(8) Matrix elements for the electric quadrupole interaction, $\hat{H}_Q$:

$$\langle \eta\Lambda' S\Sigma J'\Omega' IF | \hat{H}_Q | \eta\Lambda S\Sigma J\Omega IF \rangle$$

$$= \frac{1}{2} \times term1 \times (eQq_0 \times term2 - eQq_2 \times term3), with$$

$$term1 = (-1)^{J+I+F} \begin{pmatrix} I & 2 & I \\ -I & 0 & I \end{pmatrix}^{-1} \begin{Bmatrix} F & J & I \\ 2 & I & J' \end{Bmatrix} \sqrt{(2J'+1)(2J+1)};$$

$$term2 = \frac{1}{2} \delta_{\Lambda'\Lambda} \delta_{\Omega'\Omega} (-1)^{J'-\Omega} \begin{pmatrix} J' & 2 & J \\ -\Omega & 0 & \Omega \end{pmatrix};$$

$$term3 = \sum_{q=\pm 2} \frac{1}{2\sqrt{6}} \delta_{\Lambda',\Lambda\mp 2} (-1)^{J'-\Omega'} \begin{pmatrix} J' & 2 & J \\ -\Omega' & -q & \Omega \end{pmatrix}.$$

(9) Matrix elements for the electric dipole operator, $\hat{\mu}$:

$$\langle \eta\Lambda' S'\Sigma' J'\Omega' IF' M_F' | T_p^1(\hat{\mu}) | \eta\Lambda S\Sigma J\Omega IF M_F \rangle$$

$$= (-1)^{F'-M_F'} \begin{pmatrix} F' & 1 & F \\ -M_F' & p & M_F \end{pmatrix} \times \delta_{\Sigma'\Sigma} (-1)^{J'+I+F+1} \sqrt{(2F'+1)(2F+1)} \times term$$

$$term = \begin{Bmatrix} I & J' & F' \\ 1 & F & J \end{Bmatrix} \sum_q (-1)^{J'-\Omega'} \sqrt{(2J'+1)(2J+1)} \begin{pmatrix} J' & 1 & J \\ -\Omega & q & \Omega \end{pmatrix} \langle \eta\Lambda' | T_q^1(\mu) | \eta\Lambda \rangle$$

APPENDIX B

SUPPLMENTAL MATERIAL FOR SPECTROSCOPIC STUDY OF PtF

(Chapter 6.2.3)

Description:

Table S1: The observed and calculated transition wavenumbers (cm^{-1}) for the [11.9] $\Omega=3/2 - X^2\Pi_{3/2}$ (0, 0) and (1, 0) bands system of ^{194}PtF.

Table S2: The observed and calculated transition wavenumbers (cm^{-1}) for the [11.9] $\Omega=3/2 - X^2\Pi_{3/2}$ (0, 0) and (1, 0) bands system of ^{196}PtF.

Table S3: The observed and calculated transition wavenumbers (cm^{-1}) for the [11.9] $\Omega=3/2 - X^2\Pi_{3/2}$ (0, 0) band system of ^{198}PtF.

Table S4: The observed and calculated transition wavenumbers (cm^{-1}) for the [11.9] $\Omega=3/2 - X^2\Pi_{3/2}$ (0, 0) and (1, 0) bands system of ^{195}PtF.

Table S1 The observed and calculated transition wavenumbers (cm^{-1}) for the [11.9] Ω=3/2 – $X^2\Pi_{3/2}$ (0, 0) and (1, 0) bands system of ^{194}PtF. Single prime denotes upper levels and double prime denotes lower levels.

Branch	F′	F″	Observed	Calculated	Obs.-Calc.
(0,0)					
P(5.5)	4	5	11932.6619	11932.6613	0.0006
	5	5	11932.6591	11932.6593	-0.0002
	5	6	11932.6562	11932.6565	-0.0003
P(4.5)	3	4	11933.3909	11933.3894	0.0015
	4	4	11933.3881	11933.3869	0.0012
	4	5	11933.3848	11933.3835	0.0013
P(3.5)	2	3	11934.0805	11934.0795	0.0010
	3	3	11934.0771	11934.0762	0.0009
	3	4	11934.0727	11934.0719	0.0008
P(2.5)	1	2	11934.7329	11934.7324	0.0005
	2	2	11934.7274	11934.7272	0.0002
	2	2	11934.7220	11934.7214	0.0006
Q(4.5)	4	4	11935.7117	11935.7111	0.0006
	5	4	11935.7094	11935.7091	0.0003
	4	5	11935.7085	11935.7077	0.0008
	5	5	11935.7061	11935.7057	0.0004
Q(3.5)	3	3	11935.8848	11935.8850	-0.0002
	4	3	11935.8821	11935.8825	-0.0004
	3	4	11935.8808	11935.8808	0.0000
	4	4	11935.8778	11935.8783	-0.0005
Q(2.5)	2	2	11936.0210	11936.0211	-0.0001
	3	2	11936.0174	11936.0178	-0.0004
	2	3	11936.0155	11936.0154	0.0001
	3	3	11936.0118	11936.0120	-0.0002
Q(1.5)	1	1	11936.1206	11936.1208	-0.0002
	2	1	11936.1148	11936.1156	-0.0008
	1	2	11936.1120	11936.1119	0.0001
	2	2	11936.1063	11936.1066	-0.0003
R(1.5)	2	1	11937.4086	11937.4096	-0.0010
	2	2	11937.4001	11937.4006	-0.0005
	3	2	11937.3964	11937.3973	-0.0009
R(2.5)	3	2	11937.8257	11937.8266	-0.0009
	3	3	11937.8202	11937.8209	-0.0007
	4	3	11937.8175	11937.8184	-0.0009
R(3.5)	4	3	11938.2059	11938.2067	-0.0008
	4	4	11938.2019	11938.2025	-0.0006
	5	4	11938.1997	11938.2005	-0.0008
(1,0)					
P(4.5)	3	4	12489.7040	12489.7025	0.0015

	4	4	12489.7015	12489.7002	0.0013
	4	5	12489.6983	12489.6968	0.0015
P(3.5)	2	3	12490.4032	12490.4015	0.0017
	3	3	12490.3990	12490.3984	0.0006
	3	4	12490.3950	12490.3941	0.0009
P(2.5)	1	2	12491.0610	12491.0606	0.0004
	2	2	12491.0558	12491.0558	0.0000
	2	3	12491.0503	12491.0501	0.0002
Q(2.5)	2	2	12492.3429	12492.3431	-0.0002
	3	2	12492.3396	12492.3400	-0.0004
	2	3	12492.3374	12492.3373	0.0001
	3	3	12492.3341	12492.3342	-0.0001
Q(1.5)	1	1	12492.4486	12492.4490	-0.0004
	2	1	12492.4434	12492.4442	-0.0008
	1	2	12492.4400	12492.4401	-0.0001
	2	2	12492.4349	12492.4353	-0.0004
R(1.5)	2	1	12493.7305	12493.7315	-0.0010
	2	2	12493.7219	12493.7226	-0.0007
	3	2	12493.7186	12493.7195	-0.0009
R(2.5)	3	2	12494.1388	12494.1397	-0.0009
	4	3	12494.1309	12494.1316	-0.0007
R(3.5)	4	3	12494.5077	12494.5083	-0.0006
	5	4	12494.5013	12494.5022	-0.0009

Standard Deviation=0.00074cm^{-1} (22MHz) .

Table S2 The observed and calculated transition wavenumbers (cm^{-1}) for the [11.9] Ω=3/2 – $X^2\Pi_{3/2}$ (0, 0) and (1, 0) bands system of ^{196}PtF. Single prime denotes upper levels and double prime denotes lower levels.

Branch	F′	F″	Observed	Calculated	Obs.-Calc.
(0,0)					
P(5.5)	4	5	11932.6882	11932.6876	0.0006
	5	5	11932.6863	11932.6856	0.0007
	5	6	11932.6834	11932.6828	0.0006
P(4.5)	3	4	11933.4168	11933.4149	0.0019
	4	4	11933.4137	11933.4125	0.0012
	4	5	11933.4106	11933.4091	0.0015
P(3.5)	2	3	11934.1054	11934.1043	0.0011
	3	3	11934.1017	11934.1011	0.0006
	3	4	11934.0976	11934.0968	0.0008
P(2.5)	1	2	11934.7573	11934.7564	0.0009
	2	2	11934.7516	11934.7514	0.0002
	2	2	11934.7461	11934.7457	0.0004
Q(4.5)	4	4	11935.7349	11935.7346	0.0003
	5	4	11935.7330	11935.7327	0.0003

	4	5	11935.7314	11935.7312	0.0002
	5	5	11935.7296	11935.7293	0.0003
Q(3.5)	3	3	11935.9077	11935.9082	-0.0005
	4	3	11935.9052	11935.9058	-0.0006
	3	4	11935.9036	11935.9040	-0.0004
	4	4	11935.9009	11935.9016	-0.0007
Q(2.5)	2	2	11936.0443	11936.0441	0.0002
	3	2	11936.0408	11936.0409	-0.0001
	2	3	11936.0385	11936.0384	0.0001
	3	3	11936.0350	11936.0352	-0.0002
Q(1.5)	1	1	11936.1429	11936.1436	-0.0007
	2	1	11936.1377	11936.1386	-0.0009
	1	2	11936.1342	11936.1347	-0.0005
	2	2	11936.1288	11936.1297	-0.0009
R(1.5)	2	1	11937.4311	11937.4313	-0.0002
	2	2	11937.4223	11937.4224	-0.0001
	3	2	11937.4188	11937.4192	-0.0004
R(2.5)	3	2	11937.8474	11937.8481	-0.0007
	3	3	11937.8417	11937.8424	-0.0007
	4	3	11937.8393	11937.8400	-0.0007
R(3.5)	4	3	11938.2267	11938.2279	-0.0012
	4	4	11938.2228	11938.2237	-0.0009
	5	4	11938.2203	11938.2218	-0.0015
(1,0)					
P(4.5)	3	4	12489.9370	12489.9380	-0.0010
	4	5	12489.9312	12489.9322	-0.0010
P(3.5)	2	3	12490.6347	12490.6353	-0.0006
	3	3	12490.6313	12490.6319	-0.0006
	3	4	12490.6270	12490.6277	-0.0007
P(2.5)	1	2	12491.2929	12491.2930	-0.0001
	2	2	12491.2876	12491.2878	-0.0002
	2	3	12491.2823	12491.2821	0.0005
Q(3.5)	3	3	12492.4312	12492.4314	-0.0002
	4	4	12492.4240	12492.4246	-0.0006
Q(2.5)	2	2	12492.5751	12492.5751	0.0000
	3	2	12492.5723	12492.5717	0.0006
	2	3	12492.5692	12492.5694	-0.0002
	3	3	12492.5661	12492.5660	0.0001
Q(1.5)	1	1	12492.6802	12492.6802	0.0000
	2	1	12492.6748	12492.6750	-0.0002
	1	2	12492.6714	12492.6713	0.0001
	2	2	12492.6663	12492.6661	0.0002
R(1.5)	2	1	12493.9623	12493.9623	0.0000
	2	2	12493.9542	12493.9534	0.0008
	3	2	12493.9509	12493.9500	0.0009

R(2.5)	3	2	12494.3718	12494.3712	0.0006
	3	3	12494.3661	12494.3655	0.0006
	4	3	12494.3636	12494.3630	0.0006
R(3.5)	4	3	12494.7412	12494.7410	0.0002
	5	4	12494.7351	12494.7348	0.0003

Standard Deviation=0.00074cm^{-1} (22MHz) .

Table S3 The observed and calculated transition wavenumbers (cm^{-1}) for the [11.9] Ω=3/2 – $X^2\Pi_{3/2}$ (0, 0) band system of ^{198}PtF. Single prime denotes upper levels and double prime denotes lower levels.

Branch	F′	F″	Observed	Calculated	Obs.-Calc.
(0,0)					
P(4.5)	3	4	11933.4441	11933.4421	0.0020
	4	5	11933.4381	11933.4361	0.0020
P(3.5)	2	3	11934.1324	11934.1312	0.0012
	3	4	11934.1247	11934.1234	0.0013
P(2.5)	1	2	11934.7838	11934.7830	0.0008
	2	2	11934.7783	11934.7775	0.0008
	2	3	11934.7725	11934.7718	0.0007
Q(2.5)	2	2	11936.0691	11936.0693	-0.0002
	3	3	11936.0600	11936.0600	0.0000
Q(1.5)	1	1	11936.1695	11936.1690	0.0005
	2	1	11936.1616	11936.1635	-0.0019
	1	2	11936.1589	11936.1601	-0.0012
	2	2	11936.1536	11936.1546	-0.0010
R(1.5)	2	1	11937.4539	11937.4552	-0.0013
	2	2	11937.4455	11937.4463	-0.0008
	3	2	11937.4424	11937.4428	-0.0004
R(2.5)	3	2	11937.8710	11937.8713	-0.0003
	4	3	11937.8629	11937.8630	-0.0001
R(3.5)	4	3	11938.2497	11938.2506	-0.0009
	5	4	11938.2432	11938.2443	-0.0011

Standard Deviation=0.000108cm^{-1} (32MHz) .

Table S4 The observed and calculated transition wavenumbers (cm^{-1}) for the [11.9] Ω=3/2 – $X^2\Pi_{3/2}$ (0, 0) and (1, 0) bands system of ^{195}PtF. Here F_1 refers to the ^{195}Pt hyperfine levels. Single prime denotes upper levels and double prime denotes lower levels.

Branch	F_1'	F'	F_1''	F''	Observed	Calculated	Obs.–Calc.
(0,0)							

P(5.5)	5	4.5	6	5.5	11932.6806	11932.6784	0.0022
	5	5.5	6	6.5	11932.6764	11932.6738	0.0026
	4	3.5	5	4.5	11932.6694	11932.6672	0.0022
	4	4.5	5	5.5	11932.6639	11932.6625	0.0014
P(4.5)	4	3.5	5	4.5	11933.4091	11933.4074	0.0017
	4	4.5	4	4.5	11933.4067	11933.4050	0.0017
	4	4.5	5	5.5	11933.4033	11933.4017	0.0016
	3	2.5	4	3.5	11933.3943	11933.3929	0.0014
	3	3.5	4	4.5	11933.3885	11933.3872	0.0013
P(3.5)	3	2.5	3	2.5	11934.1092	11934.1081	0.0004
	3	3.5	3	3.5	11934.1017	11934.1009	0.0008
	3	2.5	4	3.5	11934.0999	11934.0990	0.0009
	3	3.5	4	4.5	11934.0924	11934.0918	0.0006
	2	1.5	3	2.5	11934.0806	11934.0788	0.0018
	2	2.5	3	2.5	11934.0769	11934.0755	0.0014
	2	2.5	3	3.5	11934.0728	11934.0715	0.0006
P(2.5)	2	1.5	2	1.5	11934.7679	11934.7675	0.0004
	2	2.5	2	2.5	11934.7573	11934.7573	0.0000
	2	1.5	3	2.5	11934.7553	11934.7550	0.0003
	2	2.5	3	2.5	11934.7503	11934.7502	0.0001
	2	2.5	3	3.5	11934.7451	11934.7449	0.0002
	1	0.5	2	1.5	11934.7220	11934.7210	0.0010
	1	1.5	2	1.5	11934.7171	11934.7162	0.0009
	1	1.5	2	2.5	11934.7118	11934.7108	0.0010
Q(4.5)	5	5.5	5	4.5	11935.7277	11935.7284	-0.0007
	5	4.5	5	4.5	11935.7270	11935.7263	0.0006
	5	5.5	5	5.5	11935.7218	11935.7212	0.0006
	4	3.5	4	3.5	11935.7166	11935.7163	0.0007
	4	4.5	4	4.5	11935.7117	11935.7111	0.0006
Q(3.5)	4	3.5	3	2.5	11935.9099	11937.9101	-0.0002
	4	4.5	3	3.5	11935.9036	11937.9037	-0.0001
	4	3.5	4	3.5	11935.9010	11935.9010	0.0000
	4	3.5	4	4.5	11935.8969	11935.8970	-0.0001
	4	4.5	4	4.5	11935.8944	11935.8946	-0.0002
	3	2.5	3	2.5	11935.8881	11935.8885	-0.0004
	3	3.5	3	3.5	11935.8819	11935.8820	-0.0001
Q(2.5)	3	2.5	2	1.5	11936.0510	11936.0509	0.0001
	3	3.5	2	2.5	11936.0423	11936.0423	0.0000
	3	3.5	3	3.5	11936.0387	11936.0384	0.0003
	3	2.5	3	3.5	11936.0348	11936.0352	-0.0004
	3	3.5	3	2.5	11936.0332	11936.0331	0.0001
	3	2.5	3	2.5	11936.0299	11936.0299	0.0000
	2	1.5	2	1.5	11936.0213	11936.0215	-0.0002
	2	2.5	2	1.5	11936.0177	11936.0162	-0.0005
	2	1.5	2	2.5	11936.0159	11936.0162	-0.0003

	2	2.5	2	2.5	11936.0124	11936.0129	-0.0005
Q(1.5)	2	1.5	1	0.5	11936.1588	11936.1600	-0.0012
	2	2.5	1	1.5	11936.1481	11936.1474	0.0007
	2	1.5	2	1.5	11936.1393	11936.1401	-0.0008
	2	2.5	2	1.5	11936.1344	11936.1353	-0.0009
	2	1.5	2	2.5	11936.1315	11936.1323	-0.0008
	2	2.5	2	2.5	11936.1265	11936.1275	-0.0010
	1	0.5	1	0.5	11936.1136	11936.1136	0.0000
	1	1.5	1	0.5	11936.1086	11936.1087	-0.0001
	1	0.5	1	1.5	11936.1060	11936.1058	0.0002
	1	1.5	1	1.5	11936.1005	11936.1010	-0.0005
	1	0.5	2	1.5	11936.0942	11936.0936	0.0006
R(1.5)	3	2.5	2	2.5	11937.4147	11937.4157	-0.0010
	2	1.5	1	0.5	11937.4135	11937.4141	-0.0006
	3	3.5	2	2.5	11937.4120	11937.4125	-0.0005
	2	1.5	1	1.5	11937.4056	11937.4063	-0.0007
	2	2.5	1	1.5	11937.4021	11937.4030	-0.0009
	2	1.5	2	1.5	11937.3934	11937.3941	-0.0007
	2	2.5	1	1.5	11937.3900	11937.3908	-0.0008
	2	2.5	2	2.5	11937.3823	11937.3831	-0.0008
R(2.5)	4	3.5	3	2.5	11937.8400	11937.8404	-0.0004
	4	3.5	3	3.5	11937.8344	11937.8351	-0.0007
	4	3.5	3	3.5	11937.8321	11937.8327	-0.0006
	3	2.5	2	1.5	11937.8304	11937.8312	-0.0008
	3	2.5	2	2.5	11937.8249	11937.8259	-0.0010
	3	2.5	2	2.5	11937.8223	11937.8234	-0.0011
	3	2.5	3	2.5	11937.8182	11937.8188	-0.0006
	3	3.5	3	3.5	11937.8152	11937.8163	-0.0011
	3	3.5	3	3.5	11937.8103	11937.8110	-0.0007
R(3.5)	5	4.5	3	3.5	11938.2242	11938.2251	-0.0009
	5	4.5	4	3.5	11938.2195	11938.2200	-0.0005
	5	4.5	4	4.5	11938.2154	11938.2160	-0.0006
	5	5.5	4	4.5	11938.2132	11938.2141	-0.0009
	4	3.5	3	2.5	11938.2106	11938.2119	-0.0013
	4	3.5	3	3.5	11938.2078	11938.2079	-0.0001
	4	4.5	3	3.5	11938.2043	11938.2059	-0.0016
	4	3.5	4	3.5	11938.2018	11938.2028	-0.0010
	4	4.5	4	3.5	11938.1995	11938.2008	-0.0013
	4	4.5	4	4.5	11938.1953	11938.1968	-0.0015
(1,0)							
P(3.5)	3	2.5	3	2.5	12490.5338	12490.5336	0.0002
	3	3.5	3	3.5	12490.5269	12490.5266	0.0003
	3	2.5	4	3.5	12490.5251	12490.5245	0.0006
	3	3.5	4	3.5	12490.5219	12490.5215	0.0004
	3	3.5	4	4.5	12490.5180	12490.5175	0.0005

	2	1.5	3	2.5	12490.5051	12490.5043	0.0008
	2	2.5	3	2.5	12490.5017	12490.5013	0.0004
	2	2.5	3	3.5	12490.4980	12490.4972	0.0008
	2	2.5	4	3.5	12490.4929	12490.4921	0.0008
P(2.5)	2	1.5	2	1.5	12491.1977	12491.1986	-0.0009
	2	2.5	2	2.5	12491.1879	12491.1888	-0.0009
	2	1.5	3	2.5	12491.1861	12491.1862	-0.0001
	2	2.5	3	2.5	12491.1813	12491.1817	-0.0004
	2	2.5	3	3.5	12491.1758	12491.1764	-0.0006
	1	0.5	2	1.5	12491.1523	12491.1523	0.0000
	1	1.5	2	1.5	12491.1478	12491.1478	0.0000
	1	1.5	2	2.5	12491.1425	12491.1425	0.0000
	1	1.5	3	2.5	12491.1355	12491.1354	0.0001
Q(2.5)	3	2.5	2	1.5	12492.4757	12492.4763	-0.0006
	3	3.5	2	2.5	12492.4681	12492.4680	0.0001
	3	2.5	3	2.5	12492.4645	12492.4639	0.0006
	3	3.5	3	2.5	12492.4614	12492.4609	0.0005
	3	2.5	3	3.5	12492.4593	12492.4586	0.0007
	3	3.5	3	3.5	12492.4560	12492.4556	0.0004
	2	1.5	2	1.5	12492.4772	12492.4470	0.0002
	2	2.5	2	1.5	12492.4436	12492.4440	-0.0004
	2	1.5	2	2.5	12492.4421	12492.4417	0.0004
	2	2.5	2	2.5	12492.4388	12492.4386	0.0002
	2	1.5	3	2.5	12492.4348	12492.4346	0.0002
	2	2.5	3	2.5	12492.4313	12492.4315	-0.0002
	2	2.5	3	3.5	12492.4267	12492.4262	0.0005
Q(1.5)	2	1.5	1	0.5	12492.5917	12492.5912	0.0005
	2	2.5	1	1.5	12492.5791	12492.5789	0.0002
	2	1.5	2	1.5	12492.5698	12492.5712	-0.0014
	2	2.5	2	1.5	12492.5661	12492.5668	-0.0007
	2	1.5	2	2.5	12492.5631	12492.5635	-0.0004
	2	2.5	2	2.5	12492.5596	12492.5590	0.0006
	1	0.5	1	0.5	12492.5452	12492.5449	0.0003
	1	1.5	1	0.5	12492.5402	12492.5404	-0.0002
	1	0.5	1	1.5	12492.5371	12492.5371	0.0000
	1	1.5	1	1.5	12492.5323	12492.5326	-0.0003
	1	1.5	2	1.5	12492.5207	12492.5204	0.0003
	1	1.5	2	2.5	12492.5132	12492.5127	0.0005
R(1.5)	3	2.5	2	1.5	12493.8493	12493.8489	0.0004
	3	2.5	2	2.5	12493.8419	12493.8412	0.0007
	3	3.5	2	2.5	12493.8384	12493.8396	-0.0012
	2	1.5	1	0.5	12493.8384	12493.8382	0.0002
	2	1.5	1	1.5	12493.8320	12493.8318	0.0002
	2	2.5	1	1.5	12493.8279	12493.8288	-0.0009
	2	1.5	2	1.5	12493.8196	12493.8196	0.0000

	2	2.5	2	1.5	12493.8161	12493.8166	-0.0005
	2	2.5	2	2.5	12493.8082	12493.8088	-0.0006
R(2.5)	4	3.5	3	2.5	12494.2580	12494.2578	0.0002
	4	3.5	3	3.5	12494.2529	12494.2525	0.0004
	4	4.5	3	3.5	12494.2504	12494.2503	0.0001
	3	2.5	2	1.5	12494.2479	12494.2486	-0.0007
	3	2.5	2	2.5	12494.2428	12494.2410	-0.0005
	3	3.5	2	2.5	12494.2403	12494.2410	-0.0007
	3	2.5	3	2.5	12494.2360	12494.2362	-0.0002
	3	3.5	3	2.5	12494.2335	12494.2339	-0.0004
	3	3.5	3	3.5	12494.2280	12494.2286	-0.0006

Standard Deviation=0.00079cm^{-1} (24MHz) .